

2018-01-01

Geometry, Timing, And Kinematics Of Neogene Extensional And Transtensional Structures Of Southern Death Valley: Implications For Regional Reconstructions And A Corrective Method For Rigid Body Rotations

Zachariah Fleming

University of Texas at El Paso, zachariah.fleming@protonmail.com

Follow this and additional works at: https://digitalcommons.utep.edu/open_etd



Part of the [Geology Commons](#), and the [Remote Sensing Commons](#)

Recommended Citation

Fleming, Zachariah, "Geometry, Timing, And Kinematics Of Neogene Extensional And Transtensional Structures Of Southern Death Valley: Implications For Regional Reconstructions And A Corrective Method For Rigid Body Rotations" (2018). *Open Access Theses & Dissertations*. 3.

https://digitalcommons.utep.edu/open_etd/3

This is brought to you for free and open access by DigitalCommons@UTEP. It has been accepted for inclusion in Open Access Theses & Dissertations by an authorized administrator of DigitalCommons@UTEP. For more information, please contact lweber@utep.edu.

GEOMETRY, TIMING, AND KINEMATICS OF NEOGENE EXTENSIONAL
AND TRANSTENSIONAL STRUCTURES OF SOUTHERN DEATH VALLEY:
IMPLICATIONS FOR REGIONAL RECONSTRUCTIONS AND
A CORRECTIVE METHOD FOR
RIGID BODY ROTATIONS

ZACHARIAH DOUGLAS FLEMING

Doctoral Program in Geological Sciences

APPROVED:

Terry Pavlis, Ph.D., Chair

Jose Hurtado, Ph.D.

Marianne Karplus, Ph.D.

Jason Ricketts, Ph. D.

Oscar Dena, Ph. D.

Benjamin C. Flores, Ph.D.
Interim Dean of the Graduate School

Copyright ©

by

Zachariah Douglas Fleming

2018

Dedication

This manuscript is dedicated to Jane. None of this would have been possible without you. Also, my parents for inspiring me and supporting me throughout the years.

GEOMETRY, TIMING, AND KINEMATICS OF NEOGENE EXTENSIONAL
AND TRANSTENSIONAL STRUCTURES OF SOUTHERN DEATH VALLEY:
IMPLICATIONS FOR REGIONAL RECONSTRUCTIONS AND A
CORRECTIVE METHOD FOR RIGID BODY ROTATIONS

by

ZACHARIAH DOUGLAS FLEMING

DISSERTATION

Presented to the Faculty of the Graduate School of
The University of Texas at El Paso
in Partial Fulfillment
of the Requirements
for the Degree of

DOCTOR OF PHILOSOPHY

Department of Geological Sciences
THE UNIVERSITY OF TEXAS AT EL PASO

December 2018

Acknowledgements

I would like to acknowledge my advisor, Dr. Terry Pavlis, for his guidance throughout this work and for introducing me to wonderful geology of Death Valley. Also, the rest of my committee and the UTEP Geology Department for all the support and feedback during my study. Field work would not have been possible without the help of Jim Rutkofske.

Support for the research was provided by NSF EAR-1250388, NSF Project DUE 1323419, and a 2017 GSA Student Grant.

Table of Contents

Acknowledgements.....	v
Table of Contents.....	vi
List of Tables	ix
List of Figures.....	x
List of Plate.....	xii
Chapter 1: An Orientation Based Correction Method for SfM-MVS Point Clouds—Implications for Field Geology	1
1.1 Abstract.....	1
1.2 Introduction.....	3
1.2.1 Basics of Structure from Motion and Multi-View Stereo Photogrammetry.....	6
1.2.2 Study Area	8
1.3 Methodology.....	9
1.3.1 Field Methods and Image Acquisition.....	9
1.3.2 Data Processing and Interpretation	11
1.4 Results.....	12
1.4.1 Comparison of Models from Different Cameras	12
1.4.2 Comparison of Orientation Data from Point Cloud Measurements to Field Measurements	13
1.4.3 Correstion of Point Cloud Measurements Using Known Field Controls	15
1.5 Discussion.....	18
1.5.1 Model to Model Discrepancies	18
1.5.2 Use of Field Data to Orient Point Cloud Models	19
1.5.3 Pitfalls of Point Cloud Multi-Point Analysis for Geology	21
1.6 Conclusions.....	22
Supplementary Models	36
Data Supplement 1.1	37
Data Supplement 1.2.....	42
References.....	45
Chapter 2: Geology and Structure of Ibex Hills and Saratoga Hills, CA	48
2.1 Abstract.....	48

2.2	Introduction.....	49
2.3	Tectonic Setting.....	51
2.4	Methodology.....	54
2.4.1	Geologic Mapping	54
2.4.2	Cross-Section Construction	56
2.4.3	Kinematic Analysis.....	57
2.5	Results and Observations.....	58
2.5.1	Map Units: Stratigraphy of the Mapped Area	58
2.5.2	Geologic Mapping	64
2.5.3	Fault Geometry in the Ibex Hills	66
2.5.4	Folding in the Ibex Hills	71
2.5.5	Kinematic Analysis.....	72
2.5.6	Fault Reconstruction	74
2.5.7	Fold Analysis	76
2.6	Discussion.....	77
2.6.1	Structural Evolution of the Ibex Hills and Saratoga Hills	77
2.6.2	Implications for Extensional Models of the Region	79
2.6.3	Genesis of Curved Fault Surfaces in the Ibex Hills.....	81
2.6.4	Correlations within the Ibex Pass Basin	83
2.7	Conclusions.....	83
	References.....	105
Chapter 3: Regional Correlations of the Ibex Hills in the Southern Death Valley Region, CA ..		112
3.1	Abstract.....	112
3.2	Introduction.....	113
3.3	Previous Work	115
3.3.1	Rolling-Hinge Model.....	115
3.3.2	Discrete Fault Model	117
3.4	Geologic Setting	118
3.4.1	Sheephead Fault.....	118
3.4.2	Grand View Fault	119
3.4.2	Ibex Pass	120
3.5	Methodology.....	122
3.5.1	Creation of 3D Geologic Model	122
3.5.2	Determining Piercing Lines for Reconstruction	123

3.5.3 Other Considerations	124
3.6 Results.....	125
3.6.1 Northwest Directed Extension.....	125
3.6.2 Offset Along the Sheephead Fault and/or Grand View Fault.....	127
3.6.3 Southwest Directed Extension.....	128
3.7 Discussion.....	129
3.8 Conclusions.....	132
References.....	148
Vita.....	154

List of Tables

Table 1.1: Comparison of Model and Field Orientations	34
Table 1.2: Comparison of Nikon and Sony Derived Data	35
Table 2.1: Stretch and Heave of Section Traces	103

List of Figures

Figure 1.1: Location Map of Study Area	24
Figure 1.2: Field Photograph of the Modeled Outcrop.....	25
Figure 1.3: Field Phtograph of a Fold within the Outcrop	26
Figure 1.4: Screenshots of the Dense Point Cloud	27
Figure 1.5: Point Cloud Showing Scalar Distances of the Two Datasets.....	28
Figure 1.6: Comparison of Model and Field Surfaces.....	29
Figure 1.7: Precision Experiments.....	30
Figure 1.8: Rotation Axes for Study Area Outcrop Model	31
Figure 1.9: Rotations Axes for Unreferenced Examples	32
Figure 1.10: Stereonet of Corrected Model Planes.....	33
Figure 2.1: Location Map of Study Area with Major Fault Zones	85
Figure 2.2: Simplified Stratigraphy of Southern Death Valley	86
Figure 2.3: Stratigraphy of southern Ibex Hills Compare to Ibex Pass	87
Figure 2.4: Geologic Map of the Northern Half of the Study Area-Select Faults Highlighted.....	88
Figure 2.5: Geometry of Bedding-Fault Intersections	89
Figure 2.6: Stereonet of Low Angle Normal Faults	90
Figure 2.7: Cross-Sections of the Study Area	91
Figure 2.8: Stereonet and Rose Diagram of High and Moderate Angle Normal Faults.....	92
Figure 2.9: Geologic Map of the Southern Half of the Study Area-Select Faults Highlighted.....	93
Figure 2.10: Field Photograph of Folded Noonday Formation	94
Figure 2.11: Field Photograph of a Fold Showing Cleavage Bedding Geometry	95
Figure 2.12: Odd-Axis Method of the EBF and the Low-Angle Normal Faults	96
Figure 2.13: Cross-Section D-D' Showing Both Current and Restored Geometry.....	97

Figure 2.14: Cross-Section B-B' Showing Current Geometry and Steps of Restoration.....	98
Figure 2.15: Cross-Section A-A' Showing Current Geometry and Steps of Restoration	99
Figure 2.16: Stereonets of Fold Axes and Foliation-Bedding Intersections in the Noonday Outcrop	100
Figure 2.17: Stereonet of Poles to Foliation.	101
Figure 2.18: 3D Structural Model of Noonday Outcrop.....	102
Figure 3.1: Location Map of the Study Area with Major Fault Zone.....	134
Figure 3.2: Comparison of Newly Mapped Granite Megabreccia to Previous Work	135
Figure 3.3: Comparison of Rolling-Hinge and Discrete Fault Models	136
Figure 3.4: Comparison of Ibex Pass Stratigraphy to Southern Ibex Hills.	137
Figure 3.5: Geologic Maps Showing the Igneous Deposits of Ibex Pass and the Northern Ibex Hills	138
Figure 3.6: 3D Structural Model of the Ibex Hills After High-Angle Fault Restoration	139
Figure 3.7: Screenshot of Plane Creation from Cross-Sections in Move Software.....	140
Figure 3.8: 3D Stuctural Models of the Ibex Hills Showing Progressive Restoration	141
Figure 3.9: Comparison of Noonday Basal Unconformity in the Northern Ibex Hills and the Southern Nopah Range	142
Figure 3.10: Map of Potential Restoration Paths for the Ibex Hills	143
Figure 3.11: Map of Hypothesized Displacement of Intrusive of the Northern Ibex Hills	144
Figure 3.12: 3D Model Showing Restored Faults Relationship with the Saddle Peak Hills.....	145
Figure 3.13: Map Showing Distance Between the Ibex Hills and the Nopah Range After Strike-Slip Restoration.....	146
Figure 3.14: Map Showing Estimate of Sheephead Fault Slip when Assuming Regional Rotation.....	147

List of Plates

Plate 1: Geologic Map of the Study Area	104
---	-----

An Orientation Based Correction Method for SfM-MVS Point Clouds— Implications for Field Geology

1.1 ABSTRACT

Advancements in computing capabilities over the last decade have allowed for the routine creation of Structure from Motion-Multiview Stereo (SfM-MVS) terrain models that can serve as base for high resolution geologic mapping. Outcrops models developed from these systems are high-resolution, photo-realistic 3D base providing unprecedented capability for geometric analysis. Yet, before this technology becomes a mainstay of field geology, the potential errors associated with it must be well understood. Here, we compare orientation measurements from multi-point analyses on the SfM-MVS point clouds to those taken in the field with the objective of resolving the geometry of complex folds within the outcrop. We also analyzed two point clouds of the same exposure created from different ground-based cameras to compare the ranges of error. We found that the point clouds produced from ground-based photos exhibited significant rigid-body rotation relative to the real world despite well distributed ground control, yet the models maintained a realistic scale and internal geometry. To correct the error the model values were rotated and the discrepancy reassessed. The two point clouds produced similar results, however, the Sony compact-digital-camera-based point cloud ultimately corresponded more closely to field values. We suggest that the primary cause of the error in the point clouds was GPS-based and was enhanced by the lack of significant topographic relief in our camera positions, allowing rigid-body rotations along the axis of the photographic array. This outcome suggests that care must be taken when GPS errors are a significant fraction of the outcrop size and relatively 2D outcrops imaged by a relatively 1D image array are subject to rotation errors that are difficult to remove without high-resolution ground control. Short of using a UAV and/or RTK-GPS we show how this can be resolved simply by collecting several known orientations in the field, which can then be used to orient the model

more accurately, akin to ground control points. This addition is a key step if this method is to be used for more thorough analysis and is a general method that could be used to orient virtual outcrops with no geographic reference.

Note: The contents of this chapter were published in the Journal of Structural Geology, vol. 113 with my advisor, Dr. Terry Pavlis as a co-author. As per UTEPs dissertation requirements I am providing this note as assurance that I did, in fact, contribute majorly to this work and subsequent publication with Dr. Terry Pavlis providing guidance and input when needed.

1.2 INTRODUCTION

Advancements in technology over the past decade have changed the way geoscientists both acquire and display their data, leading to a revolution in the performance of field mapping (Pavlis et al., 2015; Cawood et al., 2017; Pavlis and Mason, 2017). Digital-mapping techniques leverage the modern dissemination of imagery and digital elevation data, and they provide a medium for large-scale geologic features to be interpreted. More importantly, recent developments in photogrammetry allow high-resolution photo-realistic terrain models to be easily constructed, producing unprecedented visualizations of Earth's surface. However, for these models to benefit the scientific community it must be assured that they are oriented and are consistent with the sites they represent.

The advent of virtual outcrop modeling creates opportunities in which field time can be decreased because a portion of the analysis of geologic features can be completed “in-house” through three-dimensional image analysis (e.g. Schober and Exner, 2011; Bistacchi et al., 2015). The use of virtual outcrop models is therefore an important change to the field geology paradigm of single field-site analysis (Pavlis and Mason, 2017). Initially, the creators of virtual outcrops took advantage of terrestrial and airborne LiDAR and draped imagery over the LiDAR point clouds to create a colorized and topographically realistic model of the region of interest (e.g. Bonnaffe et al., 2007). The digital elevation model (DEM) produced from LiDAR provides high resolution data unique to the study area. However, a major disadvantage of LiDAR is cost, for both terrestrial and airborne systems, and mobility, in the case of terrestrial LiDAR systems (Tavani et al., 2016). These limitations become an issue when one considers that mobility and cost management are key requirements for field studies, especially in the case of academics.

More recently, Structure from Motion (SfM)-Multi-View Stereo (MVS) photogrammetric workflows have arisen as an alternative to LiDAR (e.g. White et al., 2008; Bistacchi et al., 2015; Tavani et al., 2016). The algorithms behind SfM photogrammetry have been circulating in the literature for several decades (e.g. Longuet-Higgins, 1981) and have evolved through that time to be a fully automated process which can produce accurate three-dimensional surfaces with minimal user input (Brown and Lowe, 2005; Snavely et al., 2008). With modern computing power SfM algorithms for very small models (5-20 photographs) can be run on a smartphone and larger models (100's to 1000's of photographs) can be done with consumer-grade laptop and desktop computers. The result of the SfM algorithms is a sparse point cloud with known camera and key point positions (Westoby et al., 2012). To create a dense 3D point cloud, perhaps two orders of magnitude denser than the sparse cloud, the results of the SfM algorithms must be fed into a MVS package, which then utilizes the known camera positions to create points from the overlapping photographs (Westoby et al., 2012). Terrain models created from SfM-MVS photogrammetry are comparable to those generated by terrestrial LiDAR systems (e.g. Carrivick et al., 2016), with routine resolution to centimeter scales using a conventional digital camera and photogrammetry software (e.g. Agisoft Photoscan).

One of the primary advantages of virtual outcrop models is the ability to rotate the viewpoint to any orientation without the time restrictions of field work. This flexibility allows the investigator to select structurally useful perspectives for analysis, such as inspection down the axis of folds, orthogonal viewing of faults truncating beds, etc. This ability combats a common issue in field geology which is the error associated with viewing structural geometries (e.g. interlimb angle, fault-bedding intersections, etc.) from oblique angles (Baltsavias, 1999). Minimizing this issue is crucial when one is attempting to characterize structures and put them into context within a regional geologic history. This issue is compounded in more structurally complex areas where information cannot be extrapolated from routinely collected data. For example, in the cases of non-cylindrical or refolded fold axes where the orientation of the fold axis may change significantly within the space of the section. Solving this issue using traditional field methods requires a high density of orientation data to be collected to accurately characterize the changes in the structural geometry. However, this solution quickly becomes intractable within regions containing significant topographic relief that make achieving total data coverage virtually impossible. In these areas investigators are limited to data that can be collected on foot leading to an incomplete data set.

The creation of virtual outcrop models via SfM-MVS techniques significantly diminishes these issues by allowing for 360° rotation and the measurement of geologically relevant surfaces directly from the model (Brush, 2015; Tavani et al., 2016). While countless applications for three-dimensional modeling and virtual outcrops exist in geology, the utility to field structural geology is the subject of this paper. Specifically, we analyzed an outcrop that exhibits complex, refolded disharmonic folds to compare the orientations measured from our virtual outcrop model to those taken in the field.

The data and results presented here are intended to highlight some potential pitfalls in a workflow combining SfM-MVS photogrammetry with traditional field geology. Ideally a geologist carrying only a camera and GPS unit would be able to come across an outcrop that they would like to model and quickly acquire data to generate a model of the outcrop for later analysis. The availability of this workflow should both speed up fieldwork and aid problem solving in structurally complex areas and access-challenged outcrops, saving valuable field time. The ability to create an ad hoc virtual outcrop while in the field is necessary for SfM-MVS photogrammetry to be legitimately integrated into a field geology workflow. Nonetheless, we show here that the imprecision of small handheld GPS units impacts model accuracy when outcrop models are below the scale of $\sim 100\text{m}$. More importantly, we illustrate a technique where field orientation measurements can be used to remove rigid body rotations that result from GPS imprecision. Consequently, we demonstrate SfM-MVS photogrammetry is a powerful tool in resolving complex structural problems, especially at the outcrop scale, provided the inaccuracies can be addressed.

1.2.1 Basics of Structure from Motion and Multi-View Stereo Photogrammetry

The details of the algorithms used by photogrammetry software (e.g. Agisoft Photoscan) is not the focus of this paper. However, it is important to have some background on the techniques to provide context for the study at hand.

Photogrammetry is a remote sensing technique that utilizes at least two images of a scene to derive the 3-dimensional location of features within the scene from known values of camera position, focal length, and orientation (Tavani et al., 2014). However, in cases where the camera position and geometry is not necessarily known it is still possible to derive 3-dimensional view of a scene using SfM techniques (Snavely et al., 2008; Westoby et al., 2012; Tavani et al., 2014; Bistacchi et al., 2015; Tavani et al., 2016). Most importantly, SfM requires a sequence of overlapping photographs which are taken from various points of view so that features may be mapped and correlated across the overlapping scenes in a 3-dimensional sense (Westoby et al., 2012). Initially, camera positions are very approximately estimated as differently oriented photographs are mapped and correlated along common feature sets and the internal geometry of the camera is assumed to be constant throughout the process (Westoby et al., 2012; Tavani et al., 2014). The initial camera positions are then refined iteratively as more and more solutions become available (i.e. as more photographs are integrated and features are matched), also generating the initial sparse point cloud (e.g. Snavely et al., 2008). As opposed to traditional photogrammetry the reference system of the resulting SfM 3-dimensional model is a relative one, an ‘image-space’ (Westoby et al., 2012). This relative reference system is a result of the SfM algorithms not requiring any reference information.

The results of the SfM algorithms are the intrinsic camera geometries and a sparse point cloud which can be used as inputs for MVS algorithms (Furukawa and Ponce, 2009; Furukawa et al., 2010; Westoby et al., 2012; Furukawa and Hernandez, 2015). The camera positions and the sparse point cloud are then used as references for the MVS algorithm to build on by using the points to find photographs with overlapping scenes and reconstructing their depth piece by piece (Furukawa et al., 2010).

To obtain a georeferenced SfM model, the user has two options: (1) to provide camera positions; (2) use ground control points (GCPs). GCPs are artificial targets or natural objects within the scene with a known position that can then be identified and used to orient the final model. Depending on the software used for the SfM photogrammetry process (e.g. Agisoft Photoscan, VisualSfM, etc.), the option for applying reference information is available once the photographs are imported into the software. If the camera being used has an internal GPS unit, that information is generally stored within the metadata of the photographs. Agisoft Photoscan Professional can automatically pull that information and import it into the program alongside the photographs. If the user chooses to place GCP's throughout the outcrop, either in addition to the camera positions or as the primary georeferencing technique, Agisoft Photoscan Professional has the functionality to input these values in a fraction of the scenes and then automatically match the GCP's in overlapping scenes. The user then imports the xyz coordinates of the GCP's to reference the model.

1.2.2 Study Area

Our case study is located within the northern Ibex Hills in eastern California. The Ibex Hills are within the Death Valley extensional terrain at the southern flank of the Black Mountains (Figure 1.1). During the Neogene, the Death Valley region was greatly extended between the middle Miocene to present (e.g., Holm and Wernicke, 1990; Bidgoli et al., 2015). Neogene extension was superimposed on Mesozoic contractional structures and created the folds discussed herein (e.g. Wernicke et al., 1988; Pavlis et al., 2014).

The study area is an outcrop of interbedded shale and carbonate in the upper part of the Neoproterozoic Radcliff member of the Noonday Formation. The outcrop is approximately 60 meters in length and 10 meters in height, exposed in an east-west channel in the northern Ibex Hills (Figure 1.2). The face of the outcrop is relatively steep and near vertical in places. The steepness of the outcrop face makes it difficult to conduct traditional orientation measurements, so it is a good candidate for testing the potential of SfM photogrammetry.

The folds exhibited within the outcrop range from open to sub-isoclinal with the tighter folds typically within the interbedded shales. Changes in fold axis orientation are apparent across the outcrop varying from steeply plunging to the northeast to more gently plunging to the southeast, and curvature of hinge lines is locally apparent at outcrop scale. A prominent fanning spaced cleavage is present throughout the area (Figure 1.3). Small scale, steeply dipping faults, ranging from ~1-3 meters of apparent offset, are abundant in the outcrop and locally obscure the bedding traces.

1.3 METHODOLOGY

1.3.1 Field Methods and Image Acquisition

Images were acquired with both a Sony DSC-HX9V model camera with an internal GPS device as well as a Nikon D5300 DSLR camera. The Nikon D5300 DSLR camera was equipped with a Nikon fixed focal-length 35 mm lens, which is approximately equivalent to a 52 mm focal-length lens on a 35 mm film camera. This setup is the preferred lens system for photogrammetry work using Agisoft Photoscan software (<http://www.agisoft.com/>). The f-stop of the Nikon D5300 was set at 11 and the exposure time was set to 1/400 seconds. The Sony DSC-HX9V camera contains a zoom lens, but the camera was kept at its minimum zoom setting of 4.38 mm, to provide a fixed focal length for the SfM methods. The f-stop value for the Sony DSC-HX9V was 3.3 and the exposure time was 1/200 seconds. Both cameras were equipped with automatic whiteness balancing.

To best model an outcrop with SfM-MVS photogrammetry, an array of photographs taken at different angles must be acquired (Westoby et al., 2012). Thus, photographs with each camera were taken around the outcrop to ensure as much coverage as possible and to provide the best resolution of the 3-dimensional features of the outcrops (e.g. overhangs, gullies, etc.) (Figures 1.1, 1.2 & 1.3). In models developed solely from ground-based photographs this process commonly is handicapped by inability to obtain images with variations in z (elevation) due to subdued terrain. In our case, this problem was acute with images acquired across a broad horizontal range (~50m) but a narrow vertical range (~3m). In total, 7 different camera stations were occupied to produce the model with ~50 images/station using the Nikon D5300 DSLR and <10 images/station with the Sony DSC-HX9V model camera (Figure 1.1). This large difference in the number of images/station is simply due to differences in

lens focal length with the relatively wide-angle Sony as compared to the Nikon. To best minimize the variance between the photographs taken with each camera, the images were taken sequentially with both cameras at each station. The result was 481 images from the Sony DSC-HX9V and 792 photographs from the Nikon D5300. Ultimately, only 298 and 340 images were used for the Nikon and Sony point clouds, respectively. This reduction in the number of images was primarily an attempt to streamline the workflow, especially in the case of the Nikon photographs that had many redundant images. In addition, some of the original photographs were taken of a portion of the outcrop that was simply not necessary to model for the geologic problem at hand. The photographs were taken in the afternoon so that the sunlight was above the ridge of the canyon containing the outcrop to minimize shadows. To ensure that the photographs were taken in a similar light, all images were acquired within ~2hr, which is critical for the feature matching algorithms.

Initially, two methodologies were utilized to provide georeference constraints for the final model. The first method was to use the internal GPS locations provided in the Sony DSC-HX9V. This method produces as many xyz values for each station as photographs taken. Positions recorded by the Sony DSC-HX9V varied over a range of 3-4 m, due to well-known errors in Wide Area Augmentation System (WAAS) corrected GPS positions (Kaplan and Hegarty, 2005; Zaidman, 2008). In the study area, multi-path is a potential issue because the outcrop is located within an east-west oriented channel wash (Figure 1.1), which is a prime location for signal reflections resulting in multi-path readings (Kaplan and Hegarty, 2005). If multiple photographs were taken from the same station it is undesirable, and unmanageable, to have different xyz positions for each image. To minimize these problems, we waited approximately one to two minutes at each station to ensure the GPS had sufficient time to obtain a position lock. Since the photographs from both cameras were taken at the same locations the GPS positions acquired from the Sony DSC-HX9V internal GPS were used to georeference the photographs taken with the Nikon D5300 DSLR camera when the images were analyzed.

In addition to this georeferencing method, ground control points (GCPs) were also used. We used white paper plates as target GCP's and located them with a handheld, WAAS enabled GPS. In total four GCP's were placed along the face of the outcrop (Figure 1.1). The potential issues of this method

involve the same GPS error issues as camera position such as multi-path and shadowing (Kaplan and Hegarty, 2005).

While in the field, orientations were also taken using a traditional Brunton compass and these were later used to compare to the orientations obtained from the measurements using the model. Field measurements focused on five folds that were expected to be easily resolved in the model. One of these folds also exhibited a curved fold axis at outcrop scale and was therefore analyzed as two separate sections, upper and lower, of the same fold. In addition, foliation-bedding intersections were collected so that the genesis of the foliations could be correlated to fold generation. These field orientation data were important in recognizing georeferencing errors in the models and provided a serendipitous opportunity to correct the data via rigid body rotations.

1.3.2 Data Processing and Interpretation

After returning from the field, the photographs were transferred to a Dell desktop computer with 12 Intel Xeon E5-2603 CPUs and 64 gigabytes of RAM. This relatively powerful desktop computer allowed for the data to be processed in a matter of days rather than weeks with a 2 to 4 processor machine. The processing workflow is described in Data Supplement 1 of the Supplemental Materials.

After generation of a dense point cloud (Figure 1.4), the model was exported to Maptek I-Site Studio for interpretation. I-Site Studio enables both the visualization of the 3-dimensional point clouds and the ability to draw line work, project surfaces, and take measurements of surfaces (i.e. strike and dip) directly on the point cloud model. I-Site Studio contains a routine for direct measurement of planar orientations of objects using three or more points on the model. This method was used to measure orientations both in inaccessible areas and at sites where field measurements were made on the real-world outcrop. The orientation data were then exported as a text file and imported into, and analyzed within, Stereonet 9.5 (www.geo.cornell.edu/geology/faculty/RWA/programs/stereonet). Stereonet was used to visually and quantitatively compare the orientations obtained via Maptek I-Site Studio to field data (Table 1.1). This method revealed that differences existed between model orientation and real-world orientations that were an artifact of some combination of model generation, measurement error in

the field, and our GCP method. Recognition of this error led us to develop a method for correction, using orientation data from the outcrop (see below).

The two point clouds generated from the different cameras were compared using the software CloudCompare (<http://cloudcompare.org/>) (Supplementary Model 1 and 2 in Supplemental Materials). In this program, the two point clouds were uploaded and the tool “Cloud/Cloud Distances” was used. The result of this process was a scalar distance point cloud in which each point has a distance value associated with it, which is determined from the nearest neighbors of the two original point clouds (Figure 1.5).

1.4 RESULTS

1.4.1 Comparison of Models from Different Cameras

We made two versions of this outcrop model using different cameras to evaluate how camera type and lens configuration might influence the model. Our initial prediction was that the principal distinction would be resolution, with the longer lens and higher resolution of the Nikon camera yielding a higher resolution model. To minimize other effects, we used essentially the same processing workflow for both cameras (Data Supplement 1 in Supplemental Materials) that included equivalent optimization of camera calibrations and the same ground control points. The result of this experiment was surprising in that models from the two different cameras show spatial deviations from each other (Figures 1.5). In fact, the two models were not parallel in general and in order to compare the point cloud surfaces, they were registered together using the GCPs in CloudCompare. After this registration spatial differences still existed between the point clouds (Figure 1.5).

This spatial difference was expressed through a visualization of the scalar nearest-neighbor distance between the point clouds. This analysis showed that the two raw point clouds are close in 3-dimensional space with ~90% of the distances falling below 1.5 meters. The largest differences, those greater than 2 meters, primarily come at the far edges of the point clouds where the point clouds are sparser and the different models do not resolve the same features (e.g. bushes in some photographs and not others). Thus, large errors would be expected using this nearest neighbor analysis. To eliminate this

edge effect, we filtered the data in CloudCompare to a maximum distance value of 3.0 meters based on the shape of the histogram (Figure 1.5).

After applying this filter, ~80% of the distance values are less than or equal to 1 meter (Figure 1.5). These distance values are surprising given that both models used virtually the same processing and ground control. Particularly significant is an apparent systematic error across the exposure shown by a patch of the model, blue in Figure 1.5, where the error is virtually zero with error increasing outward from this patch.

To further evaluate this discrepancy, we queried the scale of known objects that are in both models, namely the plates used as GCPs. The plates used in this project had a diameter of 9 inches or ~0.23 meters. Measurements were taken from both point clouds, 6 in total, yielding an average diameter value of 0.229 meters for a range of 0.22-0.24 meters. The evidence for accurate sizes of the plates suggests the models derived from both cameras provided scales accurate to those of the real world. Thus, this spatial error between the models does not appear to be a scale discrepancy between them but is more likely related to errors in surface rendering in the point cloud, for example the smoothing of surfaces (Figure 1.6).

1.4.2 Comparison of Orientation Data from Point Cloud Measurements to Field Measurements

After aligning the two camera models, we conducted an experiment to compare measurements made in the field with a conventional Brunton compass to remotely sensed orientation measurements made on each point cloud. To evaluate the variations, we compared the orientations of point cloud surfaces which corresponded to those collected in the field. This procedure was done using the multi-point orientation-analysis functions in CloudCompare, allowing the user to select any number of points and then fits a plane to all selected points using a least squares analysis. The orientation of this plane is then reported to the user in the form of strike and dip. At each surface of interest, 25-50 measurements were taken, depending on the size of the area, and the average value for each set was used for the rest of the analysis of this paper (Figure 1.7). The average measurements are provided in Table 1.1. A serendipitous result of this experiment was a discovery that consistent mismatches existed between

orientations measured in the two methods, implying that although the model was spatially accurate, it was rotated relative to geographic coordinates.

Table 1.1 summarizes the data comparisons between model and field measurements for the Nikon and Sony derived models. It is not clear from visual inspection if these distinctions are due to poor representations of the model surface resulting in variable measurements and/or error due to spatial orientation problems of the models. Thus, we further evaluated the data with a precision experiment from each studied area in each point cloud model (Figure 1.7). For all but two of surfaces the poles to the planes resulted in 95% confidence intervals of less than 3° (Figure 1.7 and Table 1.1). In the cases with higher confidence intervals, one had an alpha 95% of 4° while the other had an alpha 95 of 6.6° (Figure 1.7 and Table 1.1). The cases which show high-precision results suggest the point clouds are well behaved as a smooth measurement surface. The error is most likely related to model orientation or internal geometry error and likely has little to do with user measurement error of the point cloud. On the other hand, those cases that exhibited greater variation are more likely influenced by issues of an inconsistent measurement surface leading to a higher likelihood of user error. We therefore use the 95% confidence intervals as a preliminary estimate of error associated with the model measurements as they represent the likely variation one might obtain when measuring the point clouds.

Initially, we concentrated on twelve surfaces for this analysis, because these surfaces were easily accessible for field measurements and we presumed they would be well rendered in the model. Once the point clouds were created, however, five of these surfaces were not well rendered in the point cloud and were therefore not used for field comparison. Our analysis showed that the interior angle differences between field measured planes and the planes measured on the Nikon point cloud range from a minimum value of 21.1° to a maximum value of 57.8° (Table 1.1). The Sony derived point cloud also deviated from the field bedding data with differences ranging from 5.6° to 23.4° (Table 1.1). The five surfaces which we excluded were derived from poorly rendered regions of the models (e.g. Figure 1.6) thereby producing erroneous results. This issue has been previously acknowledged by Brush (2015) and Cawood et al. (2017) in their comparison of photogrammetric models to LiDAR models.

The majority the Nikon point-cloud orientation values were significantly different than the field measurements with all values differing by more than 20°. Table 1.2 shows the differences between field and the Nikon point-cloud measurements separated into strike and dip. These differences represent the degree of z-axis rotation of the model values relative to the field measurements and for the Nikon point cloud they range from 8-177°. Table 1.2 also shows the differences between the field and the Sony-derived point-cloud measurements separated into strike and dip. Contrary to the Nikon point cloud the majority of the values for the Sony point-cloud strike measurements relatively close to the corresponding field values with a range of 2.6-24° (Table 1.2).

In both cases, the differences in strike and dip are not consistent with both higher and lower dip angles and variably rotated strikes seen in the model data (Table 1.2). The variable orientation of point cloud data compared to field data suggests a more cryptic error than a simply vertical or horizontal axis rotation.

1.4.3 Correction of Point Cloud Measurements Using Known Field Controls

Based on the accurate scale of the models, it was most likely that the error could be solved by a rigid-body rotation of the model orientation values to the field values. To correct for this rotation, we used a relatively straightforward script in MatLab (Data Supplement 2 in Supplemental Materials). This method was based upon the hypothesis that if we can align two non-parallel planes of the model then the rotation associated with that correction should correct the model as a whole. In this method, we begin by converting the trend and plunge of the poles to the planes to their cartesian components in the right-handed coordinate system north, east, and down (NED). Then these orientations are arbitrarily paired with another model plane alongside their corresponding field-based planes. The plane pairs need not be geologically related because any non-parallel pair of planes would accomplish the same result. In our case we correct for three pairs of planes where each have two model orientations and a corresponding field orientation.

The initial step is to choose one of the model planes, referred to here as plane \mathbf{M}_1 , and rotate it to parallelism with the corresponding field measurement, plane \mathbf{F}_1 . The rotation angle and the rotation axis, \mathbf{R}_A , is defined by the cross product:

$$\mathbf{R}_A = \mathbf{M}_A \times \mathbf{F}_A \quad (1)$$

Where \mathbf{M}_A is a unit vector along the pole to the \mathbf{M}_1 and \mathbf{F}_A is a unit vector parallel to the pole to \mathbf{F}_1 , and the magnitude of \mathbf{R}_A is the Sine of the rotation angle needed to rotate \mathbf{M}_A to \mathbf{F}_A . The second plane of the pair, referred to as \mathbf{M}_2 with pole \mathbf{M}_B and its corresponding field values \mathbf{F}_2 and \mathbf{F}_B , is then rotated through the angle $\sin^{-1}(\mathbf{R}_A)$ about the axis defined by (1).

At this stage, \mathbf{M}_A and \mathbf{F}_A are coincident, but \mathbf{M}_B and \mathbf{F}_B will, in general, remain as two distinct features. A second rotation is then performed about an axis parallel to \mathbf{F}_A . To determine the magnitude of the rotation which would best align \mathbf{M}_B to \mathbf{F}_B , the MatLab script rotates about \mathbf{F}_A in 1° increments for 360° . The interior angle difference between plane \mathbf{M}_B and \mathbf{F}_B is then recorded at each step in an array, and the array is then searched for the minimum value, \mathbf{r}_{\min} , whose index represents the rotation that restores \mathbf{M}_B to alignment with \mathbf{F}_B . The Cartesian components of \mathbf{F}_A and \mathbf{r}_{\min} are then used for the second axis-angle rotation value (Eq. 2). The individual rotation matrices are then found for each of the rotations \mathbf{R}_{M_A} and \mathbf{R}_{M_B} , and multiplied to give a total rotation matrix, $\mathbf{R}_{\text{TOTAL}}$ (Eq. 3).

$$\mathbf{R}_B = (\mathbf{F}_A(1); \mathbf{F}_A(2); \mathbf{F}_A(3); \mathbf{r}_{\min}) \quad (2)$$

$$\mathbf{R}_{\text{TOTAL}} = [\mathbf{R}_{M_B}] \cdot [\mathbf{R}_{M_A}] \quad (3)$$

One key issue with this workflow is that in general the interior angle of \mathbf{M}_1 and \mathbf{M}_2 is not equal to that of \mathbf{F}_1 and \mathbf{F}_2 due to measurement error in all four orientations from imprecision in both model estimates and field measurement. In such cases, the rotation about \mathbf{R}_B will not bring \mathbf{M}_B parallel with \mathbf{F}_B . To minimize the error from this likely situation, we simply repeated the process using $\mathbf{M}_B \times \mathbf{F}_B$ for the first rotation and then following the above procedure. This process gives a second total rotation axis for the planes that is then averaged to give a mean rotation axis which gives equal weight to the pairing of

$\mathbf{M_A}$ to $\mathbf{F_A}$ and $\mathbf{M_B}$ to $\mathbf{F_B}$ (Figure 1.8 & 1.9). This complete process can then be repeated for each pair of model planes and their associated field planes, and the resultant sets of rotation axes can be used to get a best fit rotation axis using Fisher statistics (Figure 1.8 & 1.9). For rotation magnitude we used a simple average rotation from the family of rotation magnitudes.

A special case that must be considered in this workflow is one where some, or all, of the measured planes are overturned relative to the real world. In this situation, care must be taken with sign conventions where an upper hemisphere pole in the model is compared to the lower hemisphere pole of the field value. If the lower hemisphere model pole is used, the angle between it and the field pole is either too small or too large, and while it would result in one correctly oriented plane it would not work for the model at large.

To test the above methodology, we conducted a simple control experiment where we rotated a group of six arbitrary planes, as three plane pairs, about a known rotation axis with a trend and plunge of 265/50. Using the original planes as our “field” data and the rotated planes as our “model” data, we ran the values through our MatLab script. The results showed rotation axes varying less than a degree, with the small variance presumably the result of rounding error of the program, thus supporting our method, with a calculated mean trend and plunge value of 264.9/50.2 with an alpha 95 of 0.4° (Figure 1.8c).

Based on the success of this control experiment (Figure 1.8c), we applied the method using orientation data from three folds in the Ibex Hills outcrop for both the Sony and Nikon derived point clouds. Figure 8 show the six rotation axes, three fold pairs and one for each limb used as the first rotation (i.e. for calculating $\mathbf{R_A}$), for the test case and the Sony (Figure 1.8b) and Nikon (Figure 1.8a) based models. In comparison to the test case, the rotation axes have significantly more spread for these real-world data (Figure 1.8a & b). The origin of the scatter is undoubtedly the result of measurement errors within the data set, both in the field and model data, and potentially some amount of internal model error (see below). Nonetheless, because of this scatter, we conducted further tests to evaluate the

method. In these examples (Figure 1.9), we used completely non-oriented point clouds generated from Photoscan with no georeferencing information. In three cases, the calculated rotation axes form tight clusters with minimal angular dispersion, indicating the method is especially effective for such well rendered outcrops. However, in one example, a high amount of dispersion occurs among the calculated rotation axes (Figure 1.9). Inspection of that model revealed that the field measurement included sites that were difficult to measure accurately on the model due to the size of the site on the point cloud. Fortunately, this problem was easily recognized from the data itself, without visualizing the model, because the data show unrealistic geometries such as large variations in the angles between model and field planes. As a result, for this case (Figure 1.9d), the model cannot be easily aligned and probably would require revisiting the site to obtain better measurements to properly align the model.

Figure 1.10 shows a stereogram of the final rotated planes for the Sony and Nikon point clouds alongside the field orientations. Table 1.1 contains the remaining error of the Ibex Hills models relative to the field. Ultimately error that remained in both cases was minimized to mean errors of 7.5° and 10.4° for Sony and Nikon point clouds, respectively (Table 1.1). The errors for the Sony-derived point-cloud model ranged from 2.3° to 21.8° . The Nikon-based point cloud had errors ranging from 5.8° to 14.4° with all but one falling below 10° (Table 1.1). Considering all model orientations after correction, $\sim 84\%$ fell below 10° of error (Table 1.1).

1.5 DISCUSSION

1.5.1 Model to Model Discrepancies

One of the objectives of this study was to assess how models generated with a compact digital camera compared to models generated with a DSLR camera (Table 1.1 & 1.2). While the Sony compact digital camera was a camera with less resolution, it produced similar results to field data and ultimately less mean error than the Nikon point cloud even after correction. This outcome is an encouraging result

when considering the goal of producing valid 3D mapping and interpretation from less expensive equipment. However, it is also important to note that the Sony digital-camera-derived point-cloud did contain holes that were not seen in the Nikon DSLR-derived point-cloud (Figure 1.6b). Although it could likely be minimized with careful photography, both models were created with photographs from the same vantage point. Therefore, these holes may be a product of less resolution in the Sony photographs and ultimately fewer available tie-points for the SfM-MVS software to work with.

1.5.2 Use of Field Data to Orient Point Cloud Models

Although SfM/MVS models are visually striking, our experience in this study suggests care must be taken in using them for direct measurements. The most dramatic issue that arose in this study is the rotational error recognized in the model when we compared orientations from remotely sensed measurements on the point cloud vs direct field measurements. This result was initially surprising, yet in retrospect should not have been given our georeferencing method that used a standard differential GPS for georeferencing models (e.g. Bemis et al., 2014). Specifically, typical WAAS corrected differential GPS has errors of 2-3m horizontal and 4-9m vertical (Zaidman, 2008). This potential error seems trivial in normal field mapping, which is generally done at scales where this horizontal error is only a few pixels on base imagery. When errors of this magnitude are applied to reference an outcrop model that is <100m across, however, the error is a significant fraction of the model dimensions. We suggest here that this imprecision was the underlying source of the misalignment of our models that we recognized by a mismatch in orientation data collected in the field vs. the model. That is, imprecise GPS positions for cameras and markers, particularly vertical errors, led to a model that was scaled correctly, but rotated relative to geographic coordinates. This problem could be avoided by using a high precision GPS, but few geologists carry, or want to carry, these instruments routinely because of size and cost.

Fortunately, a simple solution exists for this problem with our rotation method. We suggest this method is a general method that solves a practical field problem as geologists move to collecting more and more 3D data in the field. For example, it is now straightforward to image a small outcrop to make a 3D model using SfM-MVS software, but orienting the model in real space might require a high precision GPS instrument and the added data processing burden of using high resolution ground control would likely discourage most geologists from making use of the method. Our method solves that problem. With this method, we can save large amounts of valuable field time by simply taking images for model development, then using one or more of these photos, annotate the photo with field measurements. The data could then be processed, potentially even in the field, without georeference, then reoriented using our method. We envision field scenarios in areas of poor outcrop where this method could revolutionize the field workflow by allowing high-resolution 3D modeling of key outcrops, that themselves become part of a larger field database.

Although our method provides a simple way to properly orient an unreferenced model, it is not without its own limitations. In our case study, this technique oriented the model to minimize errors between field and model measurement, yet some error remained (Table 1.1). Some of this error may simply be a routine measurement error in the field data, however, additional sources of error are likely internal to the models, which can be subtle (e.g. Fig. 1.6). Fortunately, these methods can allow for very fast measurements, far faster than field techniques, and thus, some errors could be evaluated with classic precision experiments (e.g. Fig. 1.7). Nonetheless, a cautionary note: high precision measurement is not necessarily accurate in a scenario like that shown in Figure 6. What the precision experiments do provide, however, is a degree of confidence that the measurements taken from the model are not overly erratic and are a good representation of the orientations in that area of the model. In addition, in both cases of the Ibex Hills outcrop (Figure 1.8b & c) a scatter in the rotation axes for plane pairs which be essentially parallel, if all measurements were perfect (i.e. Figure 1.8c). The discrepancy between rotation

axes determined using the rotations in a different order is likely a simple consequence of measurement error distributed among the four measurements for each plane pair. The origin of the scatter among the total rotation axes, however, is less obvious. We suggest that future studies should examine this problem more fully.

In lieu of quantifying all measurement error, we suggest that when rotating the model planes, one uses the surfaces best displayed in the point cloud and in the field, therefore likely producing the least measurement error. This suggestion is supported by results from the examples of Figure 1.9. These data were taken from point clouds with more prominent three-dimensional relief across the model relative to those taken from the Ibex Hills outcrop. The larger areas of three-dimensional relief make for surfaces that can not only be more easily measured, but also any point cloud aberrations would make up less of the measured points, thus yielding a more accurate multi-point analysis. Therefore, when applying this method, users should look for surfaces with obvious planar geometry and at a scale large enough to accurately analyze on the model. Additionally, a range of orientations should be sought to insure clear resolution of rotation axes (e.g. two nearly coplanar surfaces with a minor error would clearly produce a poor result relative to two orthogonal surfaces and may produce unreliable rotation axes).

Note that this method requires some careful consideration of the geometry that is best for the model correction, not necessarily for resolution of a conventional geologic problem. For example, in the Ibex Hills outcrop, we used layering for planar references because we were measuring these surfaces anyway for our structural analysis. In retrospect, however, after developing this method, other procedures would be superior. One simple approach is to find conspicuous planar surfaces with different orientations such as bedding planes and joint sets, clearly mark the reference surfaces in the field prior to taking images, measure the surfaces and record the data on annotated photographs, then take the photographs for model development. The importance of using clearly identifiable planar features is highlighted by the poorly corrected example in Figure 1.9d. A significant amount of measurement error

in the field, upon the model surface, or error inherent in a poorly constructed model can produce such poor results and is something users should be aware of when using this method.

1.5.3 Pitfalls of Point Cloud Multi-Point Analysis for Geology

Although the multipoint analysis methods for measuring orientations on a referenced point cloud can be a powerful technique for rapid collection of orientation data, we recognized some significant pitfalls in this study and related studies (e.g. Brush 2015). A key issue is that in some scenarios, the 3D model can generate an unrealistic rendering of surfaces in the point clouds (Figure 1.6), even when the model appears photorealistic. This effect generally arises from a lack of camera angles around the area being modeled that is sufficient to resolve subtleties in the 3D geometry, leading to either holes in the point clouds (Figure 1.6b) or insufficient data for depth calculation (Figure 1.6a). If the problem is holes in the model, it is easily recognized, but when the model is artificially smoothed, erroneous measurements are possible. This effect can occur on many scales, depending on the model, and is also highly dependent on rock type. For example, a rock that produces large, ledgy outcrops exposing bedding surfaces would allow routine measurements by these methods, but a sugary marble that weathered to rounded slopes would be a case where this method would be very difficult. In these subtler cases of smoothing in the model, one might test them by finding two quality surfaces and correct those using the presented method. If there are large differences remaining with the other surfaces, they may be invalid, either due to poor measurement or model smoothing etc.

The lack of camera angles is even more pronounced in studies such as ours where we were limited to ground-based observations. For example, in localities where the height of the outcrop is significantly greater than the elevation range that photographs can be taken from, viewpoints will be strongly limited. Note that this problem is not unique to SfM-MVS models in that terrestrial LiDAR often suffers the same issue. This can be solved most readily by using unmanned aerial vehicles (UAV) or aerial photography, however, that level of equipment negates the “bare-bones” approach to creation of geologic outcrop models for the purposes of ad hoc creation while in the field. Nonetheless, as UAV’s become more common and potentially easy to use, this approach should be more carefully analyzed for field workflows.

1.6 CONCLUSIONS

The potential benefits of SfM-MVS photogrammetry are clear and based on previous studies it can produce comparable results to LiDAR given the right parameters (Glendell et al., 2017). However, its application to traditional field work is not yet seamless and our results highlight potential issues in that workflow. Significant errors in our model were brought about by the lack of vertical relief in our camera positions and GPS error. Both of which could not be corrected for in this case without the addition of more technology (e.g. UAVs, RTK GPS systems) (Cawood et al., 2017). We show, however, that a simple method can easily orient a model that is misoriented, provided the error is a simple rigid-body rotation, which from our experience is the case in SfM-MVS models that are properly acquired. Specifically, acquiring a few planes of known orientation can be compared to measurements on that model, and a simple iterative script in MatLab can produce a mean rotation axis for the entire outcrop (Figure 1.8 & 1.9). Performing this correction allows for geologically relevant observations to be made within a reasonable degree of accuracy and can save valuable field time.

Our studies underscore the role of GPS error in georeferencing SfM-MVS models and indicate that size of the outcrop is important in the role of this error. Specifically, our studied outcrop had little vertical relief (<5 m) and the GPS error is a significant fraction of the outcrop size (~ 100 m long) which led to rotation of the model relative to geographic coordinates, particularly due to error in the z direction. For larger scale cases, >100 m, this would likely be less of an issue.

Ultimately, the method we propose in this paper will assist in a more seamless transition of 3D visualization into field geology and structural geology. As this technology continues to become more routine the ability for accurate georeferencing should not remain a hinderance to the process. The simple acquisition of orientations alongside GCPs, or even in lieu of them, allows for the collection of accurate geologic information, assuming a well-formed model is created. This effectively removes the users reliance on error prone GPS, specifically hand-held units, for the creation of such models which can then be used for reliable geologic interpretation out of the field.

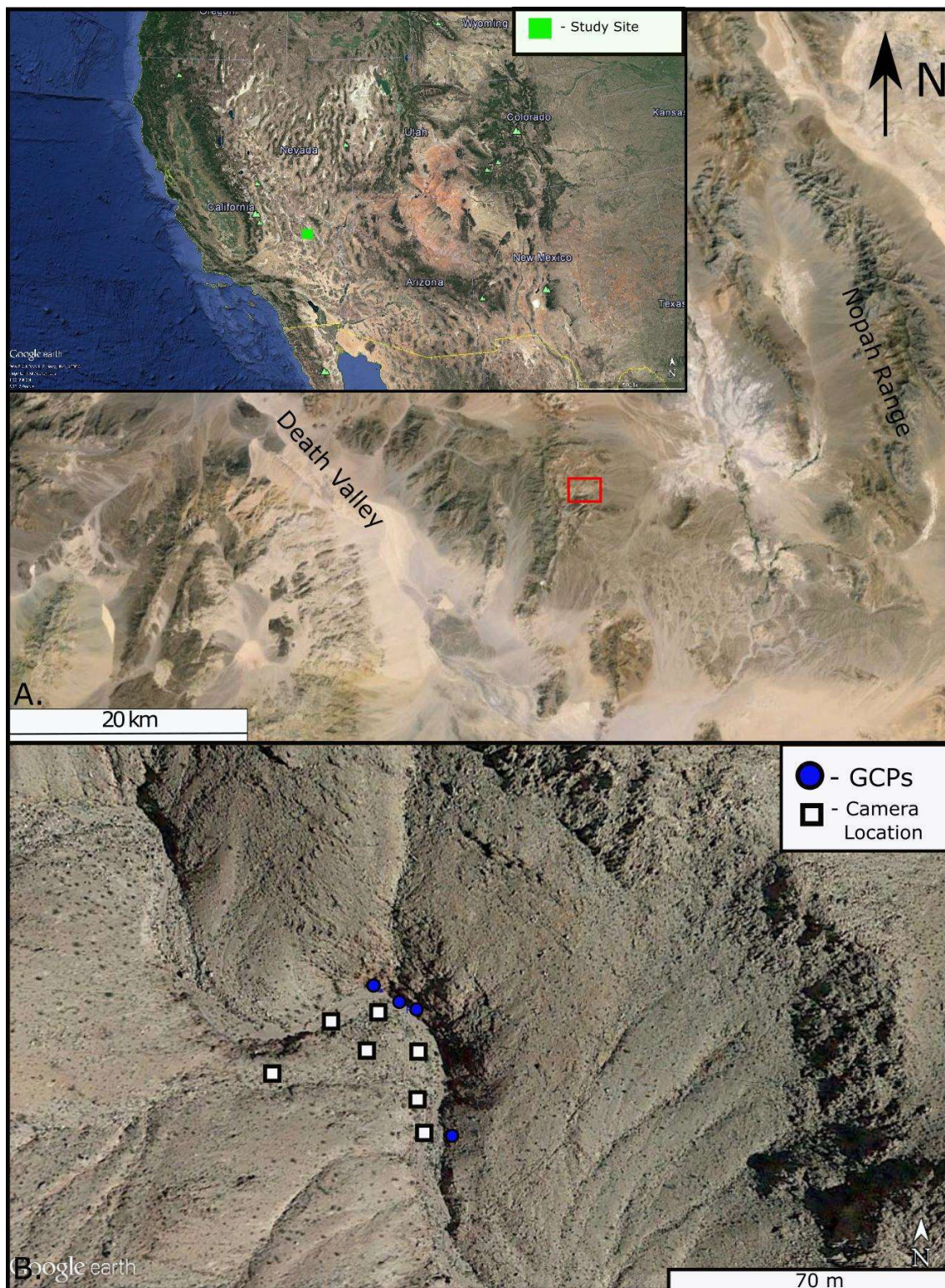


Figure 1.1. A. Regional location map of the study location with regional structures drawn approximately. B. Closer view of the study area within the Ibex Hills with the camera positions and GCPs displayed.

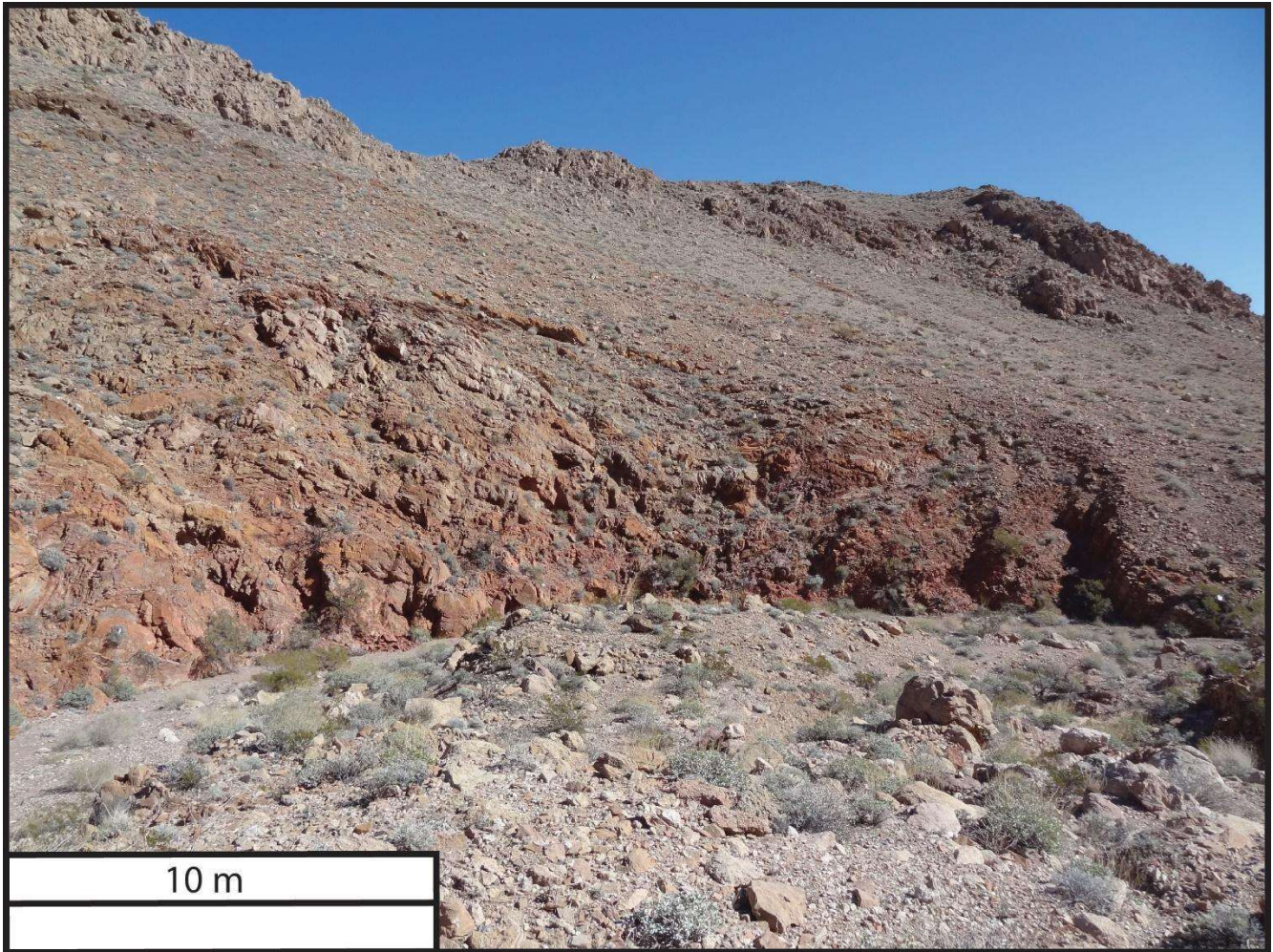


Figure 1.2. Field photograph of the outcrop modeled in this study, looking northeast.

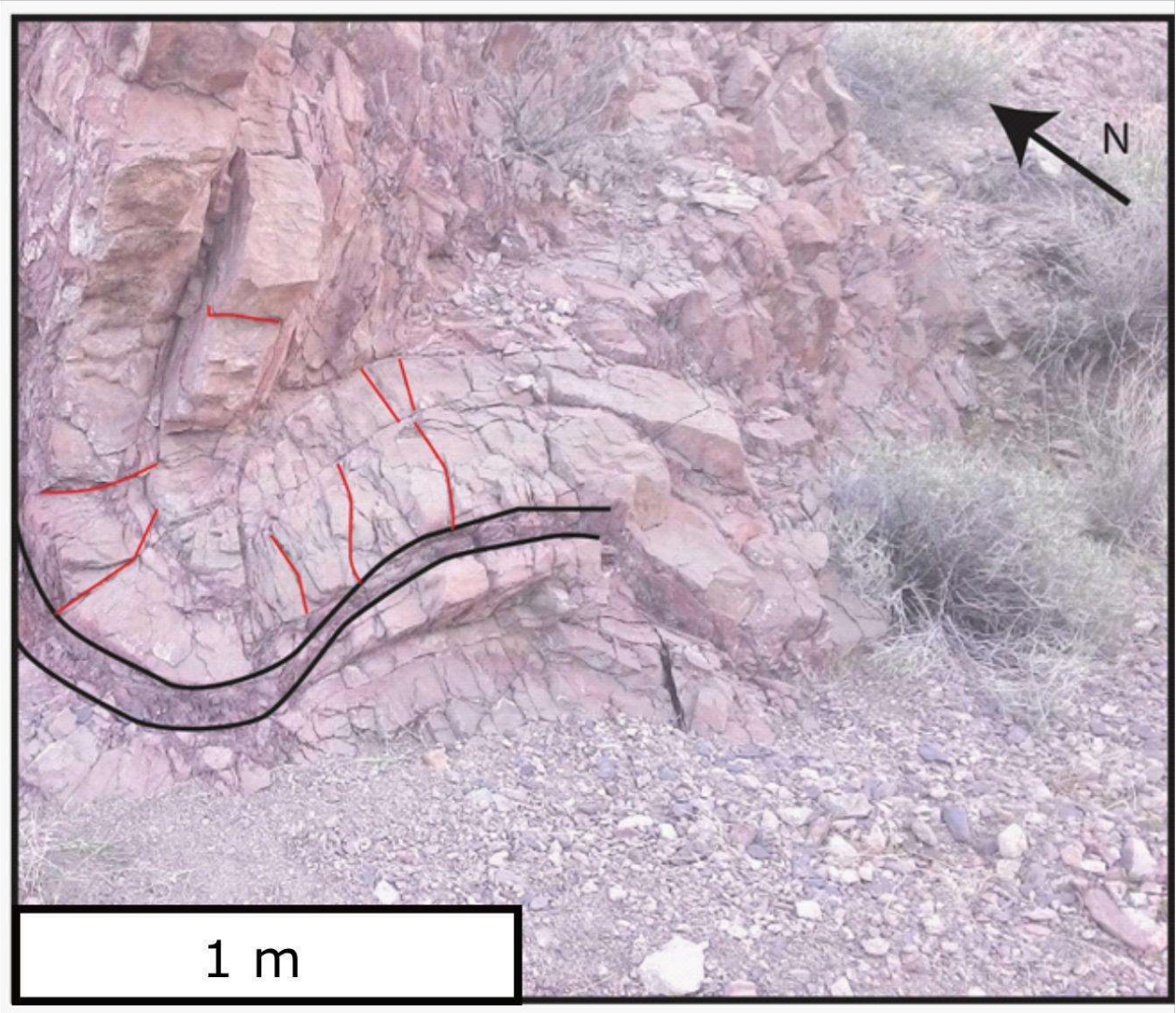


Figure 1.3. Field photograph of one of the folds within the modeled outcrop. Red lines indicate traces of the spaced cleavage in the outcrop and black lines are approximate bedding

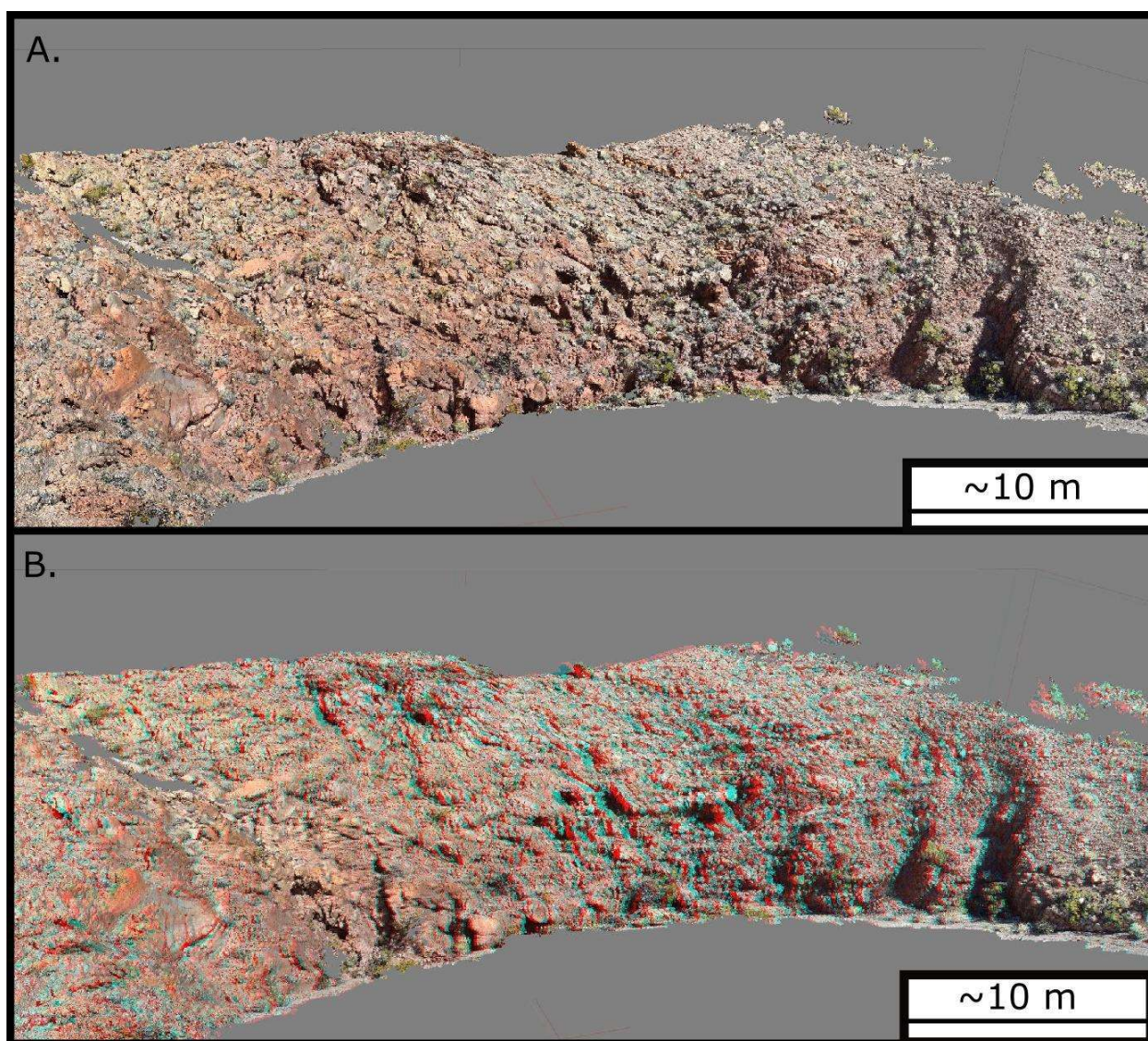


Figure 1.4. A. Screenshot showing an oblique view of the dense point cloud created in *Agisoft Photoscan*. This example is the point cloud derived from the Nikon camera. B. The same view of the point cloud but in stereo-view for use with cyan-magenta glasses.

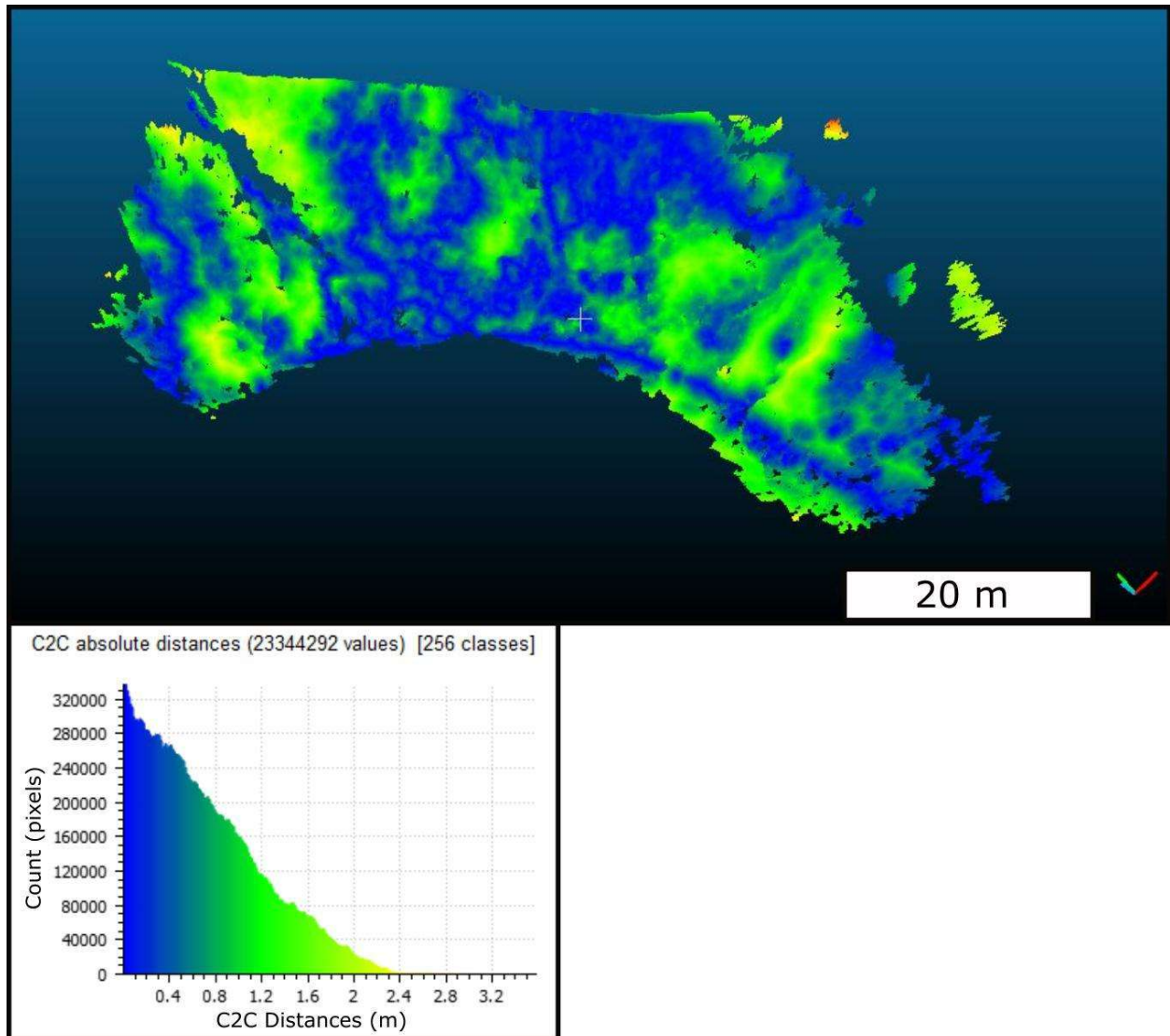


Figure 1.5. The scalar distance point cloud created in *CloudCompare* after the erroneous values near the edges of the model were filtered. At the bottom of the figure is the histogram for the point cloud which clearly shows the highest values are a small population of the overall point cloud.

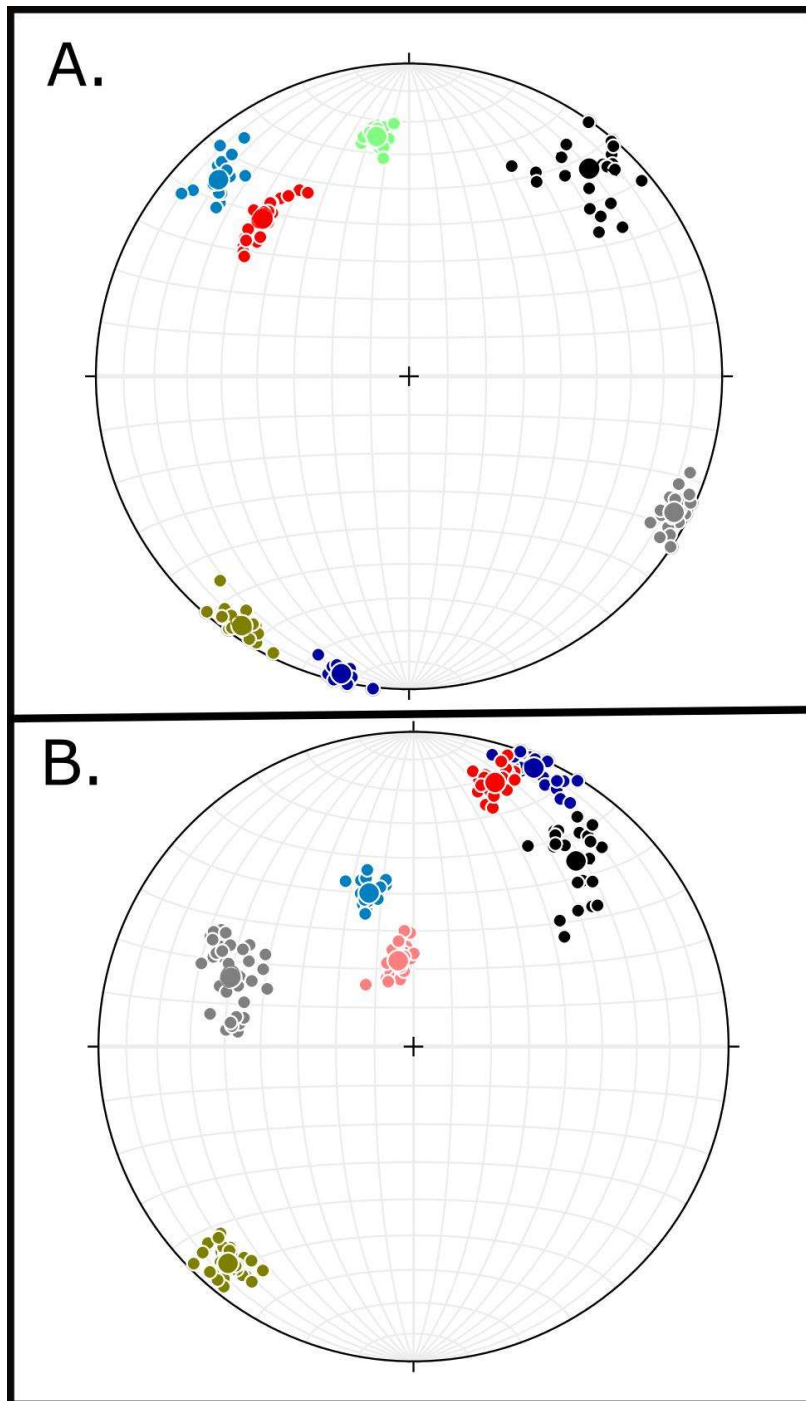


Figure 1.7. A. Precision experiments of the six surfaces used for the Ibex Hills model registration, from the Nikon model. B. Precision experiments of the six surfaces used for the Ibex Hills model registration, from the Sony model. In both cases the colors represent measurements taken from the same surface. The large circle is the mean vector of the subset.

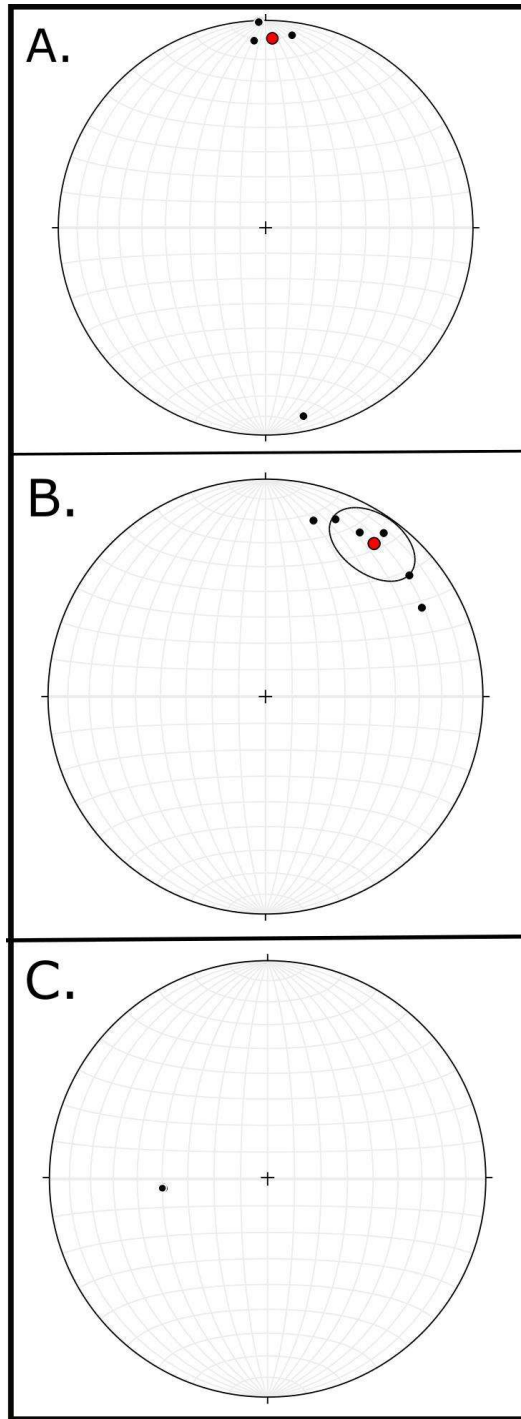


Figure 1.8. A. Rotation axes for the correction of the Nikon based point cloud. Red line indicates the mean rotation axis. B. Rotation axes for the correction of the Sony based point cloud. Red line indicates the mean rotation axis. C. Rotation axes for the test case discussed in the text.

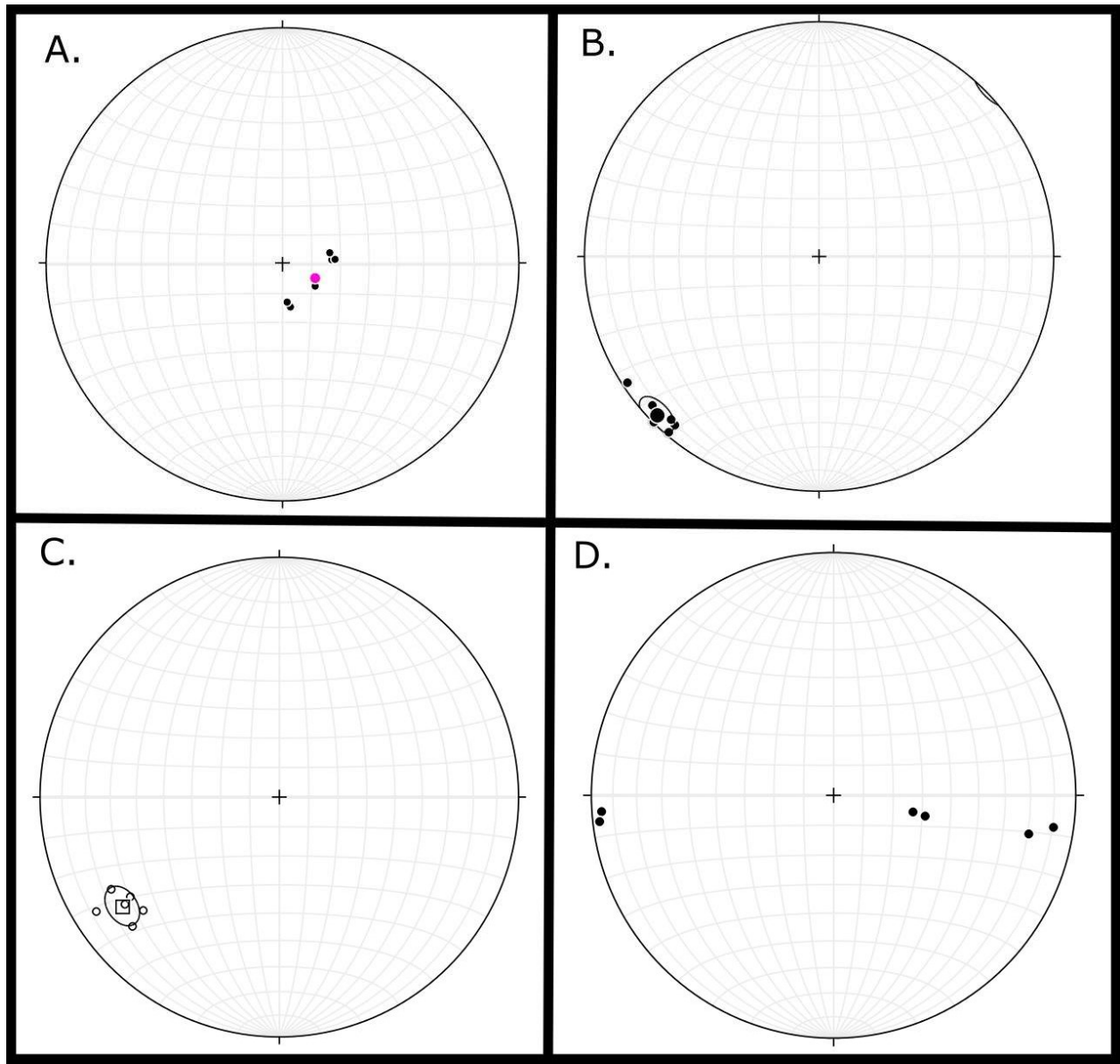


Figure 1.9. Rotations found for unreferenced point clouds to test our methodology. Note the strong grouping in examples A-C. However, D shows the effect of internal model errors of geometry, surface smoothing, or some combination.

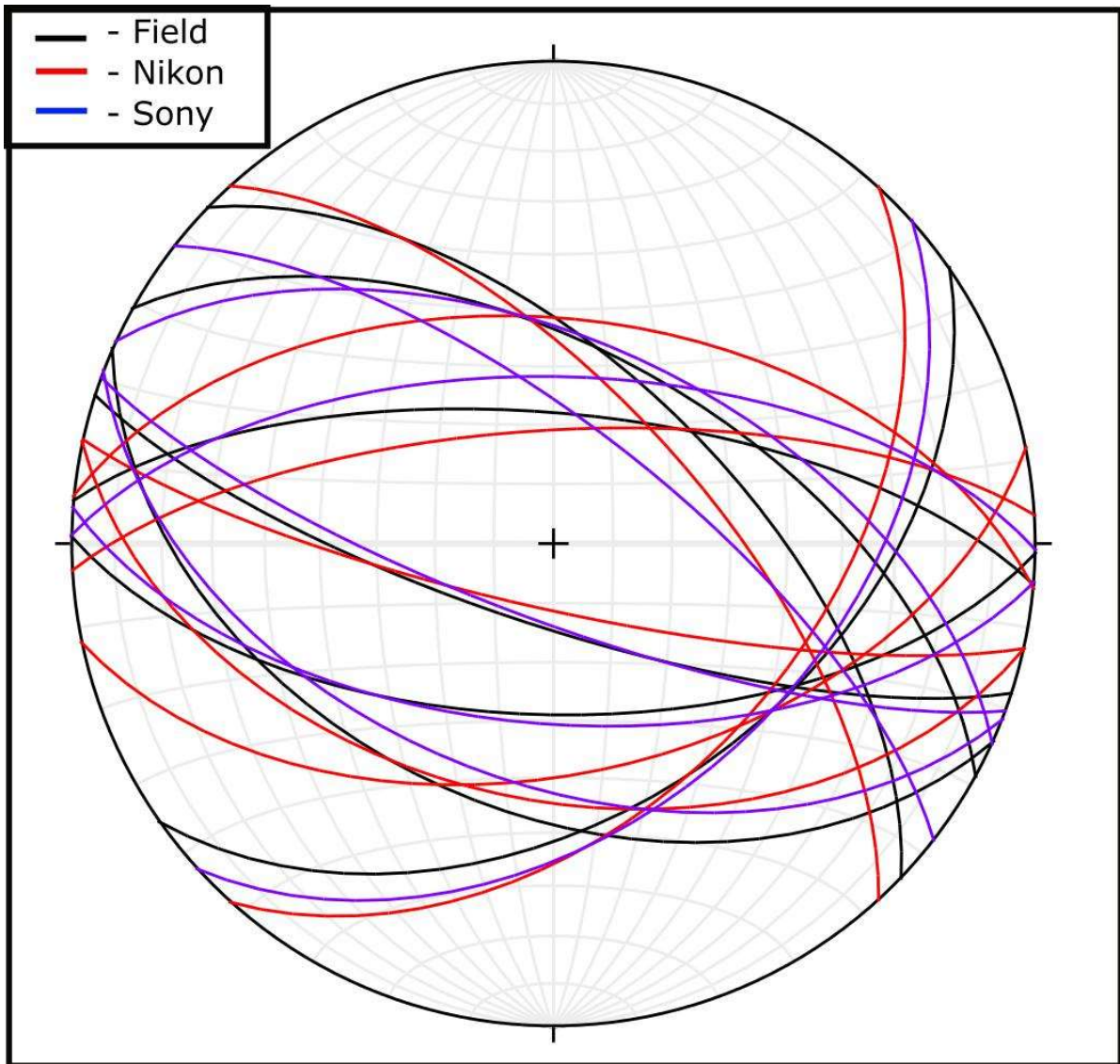


Figure 1.10. Stereonet containing both the Sony and Nikon measurements after correction alongside the corresponding field data.

Table 1.1. Table of the measured values from the Nikon and Sony point clouds along with the corresponding a95 values. The differences shown are the angular differences between the field values before and after correction.

Model Source	Strike/Dip	a95	Difference Before Rotation	Difference After Rotation	Mean Error Before Rotation	Mean Error After Rotation
Nikon	131/85.3	1.5	34.8	5.8	39.48 +-2.5	10.47 +-2.5
Nikon	207.1/83.8	6.6	57.8	8.5		
Nikon	283/86.5	1.9	20.1	8.5		
Nikon	45.9/76.6	1.1	44.5	14.4		
Nikon	82/66.4	2.4	26.4	6.2		
Nikon	45.8/58.2	1.3	53.3	8.1		
Sony	294/72	4	21.8	21.8	16.25 +-2.1	7.58 +- 2.1
Sony	51/20.7	2.5	23.4	5.1		
Sony	258.1/76.8	1.4	18.3	7.3		
Sony	103.4/76.8	1.6	19.5	3.4		
Sony	110.6/71	1.4	5.6	2.3		
Sony	126.1/46.5	1.2	8.9	5.6		

Table 1.2. Comparison of the Sony and Nikon point cloud values with those of the field in the isolated terms of strike and dip.

Data Source	Strike	Dip	Strike Difference	Dip Difference
Field	314	60	177	25.3
Nikon	131	85.3		
Field	55	44	152.1	39.8
Nikon	207.1	83.8		
Field	299	57	4.8	27.7
Nikon	303.8	84.7		
Field	275	68	8	18.5
Nikon	283	86.5		
Field	91	61	45.1	15.6
Nikon	45.9	76.6		
Field	108	76	26	9.6
Nikon	82	66.4		
Field	114	44	68.2	14.2
Nikon	45.8	58.2		
	Strike	Dip		
Field	314	60	20	12
Sony	294	72		
Field	55	44	4	23.3
Sony	51	20.7		
Field	299	57	24	6.4
Sony	275	63.4		
Field	275	68	16.9	8.8
Sony	258.1	76.8		
Field	91	61	12.4	15.8
Sony	103.4	76.8		
Field	108	76	2.6	5
Sony	110.6	71		
Field	114	44	12.1	2.5
Sony	126.1	46.5		

Supplementary Model 1. Contact author for original model using Nikon DSLR photographs.

Supplementary Model 2. Contact author for original model using Sony photographs.

Data Supplement 1: Photoscan processing

The initial step in Agisoft Photoscan Professional is to import the photographs into the program. In the case of the photographs taken with the Sony DSC-HX9V the xyz positions recorded by the cameras GPS are automatically imported alongside the photographs. However, as was previously mentioned the xyz positions provided by the internal GPS of the Sony DSC-HX9V change through time due to error of the GPS system. To correct for this an average of the position values for each camera station was used for the final model creation. To do this the camera positions along with their associated image file names were exported as a .csv text file and opened in Microsoft Excel. Using the information recorded in the field (i.e. the corresponding image files and station numbers), the images from the same camera stations were identified and their xyz information was analyzed. If the values were consistent with only a minor amount of error, then an average of the values was taken and replaced the original xyz values for each of the images at that station. However, if there was an anomalously high and/or low value(s) within the images of the station then an average including these values would likely skew the data. In all cases of this study the anomalous values were associated with the first one to three photographs taken.

Therefore, the anomalous values were inferred to have been associated with photographs taken before the internal GPS could relocate its position after movement. To ensure that the most accurate xyz values were obtained for georeferencing the model these outliers were not used to calculate the average positions of the stations. Once the average positions of the stations had been calculated these were then imported into Agisoft Photoscan Professional to be used as the true camera positions. These same xyz values were also used for the Nikon D5300 DSLR camera.

Following the addition of the camera positions the next step was to align the photographs. This step and the following actions up to exporting the final photogrammetric model are very straight forward in Agisoft Photoscan Professional and are all under the “Workflow” drop down menu on the main toolbar of the program. After selecting the “Align Photographs” command a dialog box opens which includes

options for “Accuracy” and “Pair Preselection”. Accuracy will determine how well the program determines camera positions and in the results shown herein all the models were created with choosing the high accuracy option in this dialog box. The term “Pair Preselection” refers to a process of the program which first aligns groups of photographs determined to have overlapping features before they undergo high accuracy alignment, therefore making the process more efficient (Agisoft Photoscan Professional Manual v 1.3). There are three options in the “Pair Preselection” menu which consists of “None”, “Generic”, and “Ground Control”. Choosing the option of “None” predictably omits the process of “Pair Preselection”. The choice of “Generic” initiates a process during which the program aligns subsets of photographs on a low accuracy setting and if photographs are determined to be overlapping they are then preferentially aligned on the higher accuracy setting for final alignment. The “Ground Control” option uses GCPs to find overlapping photographs and preferentially align them in the same way as the “Generic” option (Agisoft Photoscan Professional Manual v 1.3). In both cases, the Sony DSC-HX9V and Nikon D5300 photographs, the “Generic” setting was used.

The results of the “Align Photographs” function are the camera positions and associated photographs as well as a sparse point cloud. From this process, the program creates “tie points” between the images which are essentially corresponding features between photographs containing all or part of the same scene (Agisoft Photoscan Manual v 1.3). To limit potential erroneous tie points, and therefore limit error within the final point cloud, the 10% of tie points with the highest calculated error by the program were eliminated via the “Gradual Selection” function. Once these erroneous tie points were removed from the sparse point cloud the “Optimize Cameras” function was used which reworks the camera positions based on new information, in this case the removal of tie points. Once the camera positions were optimized the GCP’s were incorporated into the imported photographs. To do this the plates used as GCP’s in the field were identified in image scenes and labeled (e.g. Plate A) in Agisoft Photoscan Professional. As this is done for each GCP the image recognition capabilities of Agisoft Photoscan

Professional attempts to find the same GCPs in all the photographs which contain them. That is to say, that once the user inputs, for example, “GCP-A” as a paper plate labeled with an ‘A’ the program automatically looks for the same paper plate marked with the letter ‘A’ in each photograph and if it identifies it then the GCP marker is placed within that photograph as well. However, this process is not perfect and the program makes mistakes in recognizing the GCPs, either failing to identify them or placing them in an incorrect location. Due to this potential error, it was necessary to analyze each photograph once all the GCPs were initially identified and to insert or remove incorrect GCPs where necessary. Once the GCPs were accurately placed within the photographs the xyz positions of the plates were imported into Agisoft Photoscan Professional as a text file. With the positions of GCPs now available to the program the “Optimize Cameras” function was then used again to re-orient the cameras and model based on the input of the ground control. It is important to note that only 6 of the 8 GCPs were used in the Nikon D5300 based model simply because Agisoft Photoscan had difficulty finding two of the GCPs within the photographs and it was assumed that 6 would be sufficient for the size of our outcrop. The 2 GCPs were, however, both near the northwest edge of the model leaving that area with less spatial reference.

At this stage, the orientations of the camera positions and the geometry of the sparse point cloud can be assessed and any problems with alignment were addressed at this point. Issues with photograph alignment commonly express themselves by unrealistic camera positions which may even be underground if they were transferred to the real world or simply do not correlate with where the user took the photographs. To address these issues, we found the most effective method was to select the unaligned photographs and adjacent aligned photographs and re-align them as a subset of the rest of the photographs. Agisoft Photoscan Professional allows this to be done without re-aligning the rest of the photographs and commonly this simple method of aligning the photographs again fixes the issue. If re-aligning the problem photographs did not work, the next method we utilized was to divide the

photographs into multiple “chunks”, to use the terminology of Agisoft, which are processed as individual models and can later be merged to create the final outcrop point cloud. This method was used for the photographs taken with the Sony DSC-HX9V and was successful in creating a complete photogrammetric model. Despite the effectiveness of the aforementioned methods there were still unaligned photographs present in both sets of photographs and these were simply omitted from the rest of the process and in the final model construction. This decision, while not optimal, was made because an accurate and complete model was still able to be obtained without the problematic photographs. Following the alignment, the next step was the creation of the dense point cloud (Figure 7). The dialog box opened by selecting the “Build Dense Cloud” menu option presents choices of quality ranging from low to highest. The models presented here were created using the “high quality” setting which we found to produce results comparable to the setting of “highest quality” while saving significant processing time. The final point cloud created from the Sony DSC-HX9V consists of 32,041,353 points and the point cloud created from the Nikon D5300 consists of 69,080,011 points. The point clouds produced within Agisoft Photoscan Professional were then exported as text files to be imported into the software used for our more detailed structural analysis of the outcrop, Maptek I-Site Studio.

Data supplement 2: MatLab Script

```
%MatLab script used to solve for best fit rotation axes of plane pairs

%F1-F7 are the NED components of the field plane values
F1 = [ -0.36;-0.623;0.695];
F2 = [0.686;-0.109;0.719];
F4 = [-0.924; -0.081; 0.375];
F5 = [0.874; 0.015; 0.485];
F6 = [0.923; 0.3; 0.242];
F7 = [0.639; 0.271; 0.719];
%N1-N7 are the NED components of the model values
N1 = [-0.503; -0.422; 0.755];
N2 = [0.67; -0.505; 0.545];
N4 = [-0.777; 0; 0.629];
N5 = [0.962; -0.084; 0.259];
N6 = [0.979; 0.19; 0.07];
N7 = [ 0.845; 0.226; 0.485];
%d is used as the count through 360 degrees of rotation later in the code
d = 360;
%the angle vectors are used to store the minimum distance between the
%second model plane and field plane when rotated about the pole to the
%first. The index of these vectors gives the associated rotation amount.
angle = zeros(d,1);
angle2 = zeros(d,1);
angle3 = zeros(d,1);
%NR1, NR4, and NR6 are the initial rotation vectors (Ra in the text) for
%the first model and field values in each set of rotations
NR1 = vrrotvec(N1,F1);
NR4 = vrrotvec(N4,F4);
NR6 = vrrotvec(N6,F6);

%the for loop runs for 360 iterations
for a = 1:d;
    %NR2 test is the pole to the plane of the first field plane of the pair
    %the fourth vector value changes with each iteration by one degree
    NR2test = [F1(1);F1(2);F1(3);degtorad(a)];
    %test1mat is the rotation matrix associated with Ra and is multiplied
    %into N2 so that it is now in its first rotation orientation.
    test1mat = vrrotvec2mat(NR1);
    N2rot = test1mat*N2;
    %the matrix of the pole to the first plane is then created, which
    %changes each iteration, and used to rotate the second plane again
    test2mat = vrrotvec2mat(NR2test);
    N2rot2 = test2mat*N2rot;
    %the angular distance is then calculated in the axis-angle
    %representation and stored in the angle vector.
    diffvec = vrrotvec(N2rot2, F2);
    angle(a) = diffvec(4);
end
%the minimum angular distance and its index is then found for the second
%plane
[M,I] = min(angle);
%the index is the degree of rotation which is then used in the axis-angle
%representation of the best fit second rotation
NR2real = [F1(1);F1(2);F1(3);degtorad(I)];
```

```

%the above process is simply repeated for the NR5 and NR6 plane pair
for b = 1:d;
    NR5test = [F4(1);F4(2);F4(3);degtorad(b)];
    test4mat = vrrotvec2mat(NR4);
    N5rot = test4mat*N5;
    test5mat = vrrotvec2mat(NR5test);
    N5rot5 = test5mat*N5rot;
    diffvec2 = vrrotvec(N5rot5, F5);
    angle2(b) = diffvec2(4);
end

[X,Y] = min(angle2);

NR5real = [F4(1);F4(2);F4(3);degtorad(Y)];

%The above process is again repeated for the NR6 and NR7 plane pair.
for c = 1:d;
    NR7test = [F6(1);F6(2);F6(3);degtorad(c)];
    test6mat = vrrotvec2mat(NR6);
    N7rot = test6mat*N7;
    test7mat = vrrotvec2mat(NR7test);
    N7rot2 = test7mat*N7rot;
    diffvec3 = vrrotvec(N7rot2, F7);
    angle3(c) = diffvec3(4);
end

[A, B] = min(angle3);
NR7real = [F6(1); F6(2); F6(3); degtorad(B)];

%at this point there are six axis-angle rotations which are essentially two
%step processes of one single rotation. These are converted to matrices to
%be multiplied thereby giving one rotation for each of the three pairs
mat1 = vrrotvec2mat(NR1);
mat2 = vrrotvec2mat(NR2real);
mat3 = vrrotvec2mat(NR4);
mat4 = vrrotvec2mat(NR5real);
mat5 = vrrotvec2mat(NR6);
mat6 = vrrotvec2mat(NR7real);

%Multiplication of the two rotation matrices yields one singular rotation
RotMat1 = mat2*mat1;
RotMat2 = mat4*mat3;
RotMat3 = mat6*mat5;
%the axis-angle representation is then derived from the matrices to be
%converted to trend and plunge
VecRot1 = vrrotmat2vec(RotMat1);
VecRot2 = vrrotmat2vec(RotMat2);
VecRot3 = vrrotmat2vec(RotMat3);
%the degree of rotation is stored separatley for ease of access when
%recording data
deg1 = radtodeg(VecRot1(4));
deg2 = radtodeg(VecRot2(4));
deg3 = radtodeg(VecRot3(4));

%this same process is then repeated only using the second plane (e.g. F2,

```

%F5 etc) as the first plane to be rotated in the pair. This can be accomplished simply by swapping values at the top of the first code, which is essentially what was done below, however, the addition of "alt" was added to the end of each variable to avoid overwriting variables.

```
F2alt = [ -0.36;-0.623;0.695];
F1alt = [0.686;-0.109;0.719];
F5alt = [-0.924; -0.081; 0.375];
F4alt = [0.874; 0.015; 0.485];
F7alt = [0.923; 0.3; 0.242];
F6alt = [0.639; 0.271; 0.719];

N2alt = [-0.503; -0.422; 0.755];
N1alt = [0.67; -0.505; 0.545];
N5alt = [-0.777; 0; 0.629];
N4alt = [0.962; -0.084; 0.259];
N7alt = [0.979; 0.19; 0.07];
N6alt = [ 0.845; 0.226; 0.485];

d = 360;

anglealt = zeros(d,1);
angle2alt = zeros(d,1);
angle3 = zeros(d,1);

NR1alt = vrrotvec(N1alt,F1alt);
NR4alt = vrrotvec(N4alt,F4alt);
NR6alt = vrrotvec(N6alt,F6alt);

for a = 1:d;
    NR2testalt = [F1alt(1);F1alt(2);F1alt(3);degtorad(a)];
    test1maltalt = vrrotvec2mat(NR1alt);
    N2rotalt = test1maltalt*N2alt;
    test2maltalt = vrrotvec2mat(NR2testalt);
    N2rot2alt = test2maltalt*N2rotalt;
    diffvecalt = vrrotvec(N2rot2alt, F2alt);
    anglealt(a) = diffvecalt(4);
end

[M,I] = min(anglealt);

NR2realalt = [F1alt(1);F1alt(2);F1alt(3);degtorad(I)];

for b = 1:d;
    NR5testalt = [F4alt(1);F4alt(2);F4alt(3);degtorad(b)];
    test4maltalt = vrrotvec2mat(NR4alt);
    N5rotalt = test4maltalt*N5alt;
    test5maltalt = vrrotvec2mat(NR5testalt);
    N5rot5alt = test5maltalt*N5rotalt;
    diffvec2alt = vrrotvec(N5rot5alt, F5alt);
    angle2alt(b) = diffvec2alt(4);
end

[X,Y] = min(angle2alt);
```

```

NR5realalt = [F4alt(1);F4alt(2);F4alt(3);degtorad(Y)];

for c = 1:d;
    NR7testalt = [F6alt(1);F6alt(2);F6alt(3);degtorad(c)];
    test6maltalt = vrrotvec2mat(NR6alt);
    N7rotalt = test6maltalt*N7alt;
    test7maltalt = vrrotvec2mat(NR7testalt);
    N7rot2alt = test7maltalt*N7rotalt;
    diffvec3alt = vrrotvec(N7rot2alt, F7alt);
    angle3alt(c) = diffvec3alt(4);
end

[A, B] = min(angle3alt);
NR7realalt = [F6alt(1); F6alt(2); F6alt(3); degtorad(B)];

mat1alt = vrrotvec2mat(NR1alt);
mat2alt = vrrotvec2mat(NR2realalt);
mat3alt = vrrotvec2mat(NR4alt);
mat4alt = vrrotvec2mat(NR5realalt);
mat5alt = vrrotvec2mat(NR6alt);
mat6alt = vrrotvec2mat(NR7realalt);

RotMat1alt = mat2alt*mat1alt;
RotMat2alt = mat4alt*mat3alt;
RotMat3alt = mat6alt*mat5alt;

VecRot1alt = vrrotmat2vec(RotMat1alt);
VecRot2alt = vrrotmat2vec(RotMat2alt);
VecRot3alt = vrrotmat2vec(RotMat3alt);

deg1alt = radtodeg(VecRot1alt(4));
deg2alt = radtodeg(VecRot2alt(4));
deg3alt = radtodeg(VecRot3alt(4));

```

References

- Baltsavias, E.P., 1999, A comparison between photogrammetry and laser scanning: *ISPRS Journal of Photogrammetry and Remote Sensing*, v. 54, p. 83–94, doi: 10.1016/S0924-2716(99)00014-3.
- Bemis, S.P., Mickelthwaite, S., Turner, D., James, M.R., Akciz, S., Thiele, S.T., and Bangash, H.A., 2014, Ground-based and UAV-Based photogrammetry: A multi-scale, high-resolution mapping tool for structural geology and paleoseismology: *Journal of Structural Geology*, v. 69, Part A, p. 163–178, doi: 10.1016/j.jsg.2014.10.007.
- Bidgoli, T.S., Amir, E., Walker, J.D., Stockli, D.F., Andrew, J.E., and Caskey, S.J., 2015, Low-temperature thermochronology of the Black and Panamint mountains, Death Valley, California: Implications for geodynamic controls on Cenozoic intraplate strain: *Lithosphere*, p. L406.1, doi: 10.1130/L406.1.
- Bistacchi, A., Balsamo, F., Storti, F., Mozafari, M., Swennen, R., Solum, J., Tueckmantel, C., and Taberner, C., 2015, Photogrammetric digital outcrop reconstruction, visualization with textured surfaces, and three-dimensional structural analysis and modeling: Innovative methodologies applied to fault-related dolomitization (Vajont Limestone, Southern Alps, Italy): *Geosphere*, v. 11, p. 2031–2048, doi: 10.1130/GES01005.1.
- Bonnaffe, F., Jennette, D., and Andrews, J., 2007, A method for acquiring and processing ground-based lidar data in difficult-to-access outcrops for use in three-dimensional, virtual-reality models: *Geosphere*, v. 3, p. 501–510, doi: 10.1130/GES00104.1.
- Brown, M., and Lowe, D.G., 2005, Unsupervised 3D object recognition and reconstruction in unordered datasets, *in* Fifth International Conference on 3-D Digital Imaging and Modeling (3DIM'05), p. 56–63, doi: 10.1109/3DIM.2005.81.
- Brush, J.A., 2015, Evaluating methods of field-based 3D visualization and their application to mapping metamorphic terranes: An example from the Panamint Mountains, California: ETD Collection for University of Texas, El Paso, p. 1–141.
- Carrivick, J.L., Smith, M.W., and Quincey, D.J., 2016, *Structure from Motion in the Geosciences*: John Wiley & Sons, 211 p.
- Cawood, A.J., Bond, C.E., Howell, J.A., Butler, R.W.H., and Totake, Y., 2017, LiDAR, UAV or compass-clinometer? Accuracy, coverage and the effects on structural models: *Journal of Structural Geology*, v. 98, p. 67–82, doi: 10.1016/j.jsg.2017.04.004.
- Furukawa, Y., Curless, B., Seitz, S.M., and Szeliski, R., 2010, Towards Internet-scale multi-view stereo, *in* 2010 IEEE Computer Society Conference on Computer Vision and Pattern Recognition, p. 1434–1441, doi: 10.1109/CVPR.2010.5539802.
- Furukawa, Y., and Hernandez, C., 2015, *Multi-View Stereo: A Tutorial*: Place of publication not identified, Now Publishers Inc, 166 p.

- Furukawa, Y., and Ponce, J., 2009, Accurate Camera Calibration from Multi-View Stereo and Bundle Adjustment: *International Journal of Computer Vision*, v. 84, p. 257–268, doi: 10.1007/s11263-009-0232-2.
- Glendell, M., McShane, G., Farrow, L., James, M.R., Quinton, J., Anderson, K., Evans, M., Benaud, P., Rawlins, B., Morgan, D., Jones, L., Kirkham, M., DeBell, L., Quine, T.A., et al., 2017, Testing the utility of structure-from-motion photogrammetry reconstructions using small unmanned aerial vehicles and ground photography to estimate the extent of upland soil erosion: *Earth Surface Processes and Landforms*, p. n/a-n/a, doi: 10.1002/esp.4142.
- Harris, C., and Stephens, M., 1988, A combined corner and edge detector, *in* *In Proc. of Fourth Alvey Vision Conference*, p. 147–151.
- Holm, D.K., and Wernicke, B., 1990, Black Mountains crustal section, Death Valley extended terrain, California: *Geology*, v. 18, p. 520–523, doi: 10.1130/0091-7613(1990)018<0520:BMCSDV>2.3.CO;2.
- Kaplan, E., and Hegarty, C., 2005, *Understanding GPS: Principles and Applications*: Artech House, 718 p.
- Longuet-Higgins, H.C., 1981, A computer algorithm for reconstructing a scene from two projections: *Nature*, v. 293, p. 133–135, doi: 10.1038/293133a0.
- Norton, I., 2011, Two-stage formation of Death Valley: *Geosphere*, v. 7, p. 171–182, doi: 10.1130/GES00588.1.
- Pavlis, T.L., Brush, J., Cobb, J., and Anonymous, 2015, Paper mapping is dead and flat map geologic analysis has one foot in the grave; the new revolution in three dimensional structural analysis using inexpensive terrain models and visualization software: *Abstracts with Programs - Geological Society of America*, v. 47, p. 407.
- Pavlis, T., and Mason, K., 2017, The New World of 3D Geologic Mapping: *GSA Today*, v. 27, p. 4–10, doi: 10.1130/GSATG313A.1.
- Pavlis, T.L., Rutkofske, J., Guerrero, F., and Serpa, L.F., 2014, Structural overprinting of Mesozoic thrust systems in eastern California and its importance to reconstruction of Neogene extension in the southern Basin and Range: *Geosphere*, v. 10, p. 732–756, doi: 10.1130/GES00993.1.
- Schober, A., and Exner, U., 2011, 3D structural modelling of an outcrop-scale fold train using photogrammetry and GPS mapping: *Austrian Journal of Earth Sciences = Mitteilungen der Oesterreichischen Geologischen Gesellschaft*, v. 104, p. 73–79.
- Serpa, L., and Pavlis, T.L., 1996, Three-dimensional model of the late Cenozoic history of the Death Valley region, southeastern California: *Tectonics*, v. 15, p. 1113–1128, doi: 10.1029/96TC01633.
- Snavely, N., Seitz, S.M., and Szeliski, R., 2008, Modeling the World from Internet Photo Collections: *International Journal of Computer Vision*, v. 80, p. 189–210, doi: 10.1007/s11263-007-0107-3.

- Tavani, S., Corradetti, A., and Billi, A., 2016, High precision analysis of an embryonic extensional fault-related fold using 3D orthorectified virtual outcrops: The viewpoint importance in structural geology: *Journal of Structural Geology*, v. 86, p. 200–210, doi: 10.1016/j.jsg.2016.03.009.
- Tavani, S., Granado, P., Corradetti, A., Girundo, M., Iannace, A., Arbués, P., Muñoz, J.A., and Mazzoli, S., 2014, Building a virtual outcrop, extracting geological information from it, and sharing the results in Google Earth via OpenPlot and Photoscan: An example from the Khaviz Anticline (Iran): *Computers & Geosciences*, v. 63, p. 44–53, doi: 10.1016/j.cageo.2013.10.013.
- Wernicke, B., Axen, G.J., and Snow, J.K., 1988, Basin and Range extensional tectonics at the latitude of Las Vegas, Nevada: *Geological Society of America Bulletin*, v. 100, p. 1738–1757, doi: 10.1130/0016-7606(1988)100<1738:BARETA>2.3.CO;2.
- Westoby, M.J., Brasington, J., Glasser, N.F., Hambrey, M.J., and Reynolds, J.M., 2012, ‘Structure-from-Motion’ photogrammetry: A low-cost, effective tool for geoscience applications: *Geomorphology*, v. 179, p. 300–314, doi: 10.1016/j.geomorph.2012.08.021.
- White, L., Alfarhan, M., Ahmed, T., Aiken, C., and Anonymous, 2008, Structural and orientation analysis of 3D virtual outcrop models: Abstracts with Programs - Geological Society of America, v. 40, p. 423–424.
- Zaidman, S., 2008, Global Positioning System Wide Area Augmentation System (WAAS) Performance Standard

Geology and Structure of the Ibex Hills and Saratoga Hills, CA

2.1 ABSTRACT

Our recent mapping in the Ibex Hills demonstrates Mesozoic contractional structures overprinted by Neogene extension and strike-slip deformation. The earliest deformation is interpreted as two phases of Mesozoic shortening, recorded primarily by overprinted fold systems. The oldest folds (F1) are tight to sub-isoclinal, approximately E trending folds with an axial planar to fanning pressure solution cleavage. F1 is overprinted by approximately N-S trending, more open folds that produce strong curvature in F1 axes and type 1 interference patterns. These folds are cut by a series of Neogene faults. The oldest identified faults consist of currently low to moderate angle, E-NE dipping normal faults which are folded about a SW-NE trending axis. That this folding postdates at least some of the extension suggests a component of syn-extensional shortening that is probably strike-slip related. Cross-cutting these east dipping faults are both NW and NE striking, high angle normal faults. In general, it appears that the NE striking high-angle faults are younger and displace the other normal faults, consistent with NW directed extension superimposed on older SW directed extension. Additionally, a major N-S striking, oblique-slip fault bounds the eastern flank of the range with slickenlines measured at rakes of <30 degrees which together with the map pattern suggests dextral-oblique movement along the east front of the range. In the central Ibex Hills, the oblique fault clearly cross-cuts low angle normal faults, however, to the north it appears to be truncated by normal faults, potentially signifying a zone of accommodation related to the adjacent Sheephead Fault (SF), overprinting by NW directed extension, or both. Transcurrent systems have been proposed to explain extension parallel folding and the geometry of folded low angle faults followed by NW striking faulting in the Ibex Hills aligns with these models. Collectively the field data suggest an early period of SW directed extension is recorded in the Ibex Hills, which was suggested by B. Troxel. The younger NE striking faults presumably record the younger NW directed extension during or after SF movement.

2.2 INTRODUCTION

The Death Valley extensional terrane has long been recognized as a prime example for studying continental extension (e.g. Snow, J. K. and Wernicke, B. P., 2000; Miller and Pavlis, 2005) due to

spectacular rock outcrop, abundant pre-extensional piercing points that constrain fault movement, and its relatively young age, allowing tight age constraints on deformation. Nonetheless, because any correlation, be it stratigraphic or structural, is an interpretation open to debate, there are questions which surround the nature of the geologic structures which accommodated Neogene extension in the Death Valley region. Understanding these structures has been a focus of numerous studies (e.g. Wernicke, 1981; Wernicke et al., 1988; Topping, 1993; Miller and Prave, 2002; Miller and Pavlis, 2005) and there is no consensus on the kinematic history of the region. The rolling hinge model is a widely-cited concept applied to this region, and this kinematic model is coupled with an inference of ~140 km of Neogene extension across the Death Valley extensional terrane based on a suite of Mesozoic and older markers (e.g. Snow and Wernicke, 2000). Inherent in the rolling hinge model is the interpretation of a single, regional detachment (Figure 2.1). In contrast, others emphasize strike-slip faulting and the development of pull-apart basins between the Furnace Creek and Southern Death Valley Fault systems and suggest significantly less extension than the rolling hinge family of models (Figure 2.1), in most cases using many of the same pre-extensional markers but different interpretations of those markers (Topping, 1993; Serpa and Pavlis, 1996; Miller and Pavlis, 2005).

The Ibex Hills are located in southern Death Valley and occupy a position that varies radically among different reconstructions. Two structural features in particular are especially important in this context, the Black Mountain Detachment and the strike-slip Sheephead Fault (Figure 2.1). Holm and Wernicke (1990), Holm et al. (1992), and Topping (1993) interpreted low-angle normal fault systems in the Ibex Hills (Figure 2.2) as the uppermost portion of a pre-extensional crustal block, essentially the up-dip portion of the Black Mountains Detachment system. This interpretation has been used to support the rolling hinge model with an implication for significant denudation and subsequent exposure of the crustal section in the western Black Mountains via a regional detachment (Wernicke, 1981; Snow and Wernicke, 2000). Alternatively, Troxel et al. (1992) recognized dikes and fault geometries immediately to the south of the Ibex Hills, in the Saddle Peak Hills (Figure 2.1), indicative of southwest directed extension that pre-dated northwest directed extension. This SW directed extension is widely interpreted to be coeval with the Kingston Range detachment immediately to the southeast

(Davis et al., 1993), including an extension derived Miocene basin system, the China Ranch basin (Scott et al., 1988). The Sheephead Fault is adjacent to the Ibex Hills, just to the north, and has been cited as playing a role as a displacement transfer structure in the extension (e.g. Wright et al., 1991; Serpa and Pavlis, 1996). Nonetheless, the sense of movement on the Sheephead fault has been debated with some supporting sinistral slip (e.g. Wright and Troxel, 1984; Serpa and Pavlis, 1996) while the most recent work has interpreted the fault as an overall dextral slip system (Renik, 2010), consistent with the tectonic model of Wright et al. (1991).

Given the Ibex Hills proximity to the Sheephead Fault along with its interpreted relationship to the Black Mountains Detachment, a better understanding of the geologic history of the range can shed light on both features. Despite the pivotal location of the Ibex Hills there has been little work done in the range. The most detailed published mapping in Ibex Hills is that of Wright et al., (1968), however, this was focused only on a small portion of the range as it concerned talc deposits in the region. Therefore, an analysis of the structures of the Ibex Hills is long overdue and is the goal of the work we present herein.

This study presents geologic mapping of the Ibex Hills and Saratoga Hills along with structural and kinematic interpretations, primarily of the northern Ibex Hills given its previously interpreted relationship to the Black Mountains Detachment (Figure 2.1). We present a geologic map with accompanying cross-sections and use these data to provide new perspectives on the structural geology of the range. We also use fault kinematic data based on slickenline data, in conjunction with our map pattern, to describe separate generations of faulting which created the presently attenuated appearance of the northern Ibex Hills, as well as the relationship to regional structures, namely the Black Mountain Detachment (Figure 2.1).

2.3 TECTONIC SETTING

The Death Valley region exposes rocks that range from middle Proterozoic to Quaternary in age. After the middle Proterozoic events that formed the crystalline basement for the region (Heaman and Grotzinger, 1992) the area experienced two cycles of sedimentary deposition: (1) middle Proterozoic deposition of the Crystal Spring Formation; and (2) Neoproterozoic to middle Paleozoic strata that form

a thick, miogeoclinal succession that are widely recognized as the passive margin assemblage deposited during the breakup of Rodinia (Stewart, 1972; Wright et al., 1974). The latter produced the bulk of the sedimentary sequence recognized in southern Death Valley, from the Horse Thief Spring Formation through middle Paleozoic units (Figure 2.2).

During the late Paleozoic and throughout the Mesozoic, much of western North America underwent a series of contractional deformation events. The Mesozoic events are collectively known as the Sevier orogeny (DeCelles, 2004). The Sevier orogenic belt is a zone of generally thin-skinned deformation that verges to the southeast and extends from the southern Canada into eastern California (DeCelles, 2004). In the Death Valley area, the Sevier fold-thrust system is complicated and appears to change strike from northeast to northwest (DeCelles, 2004). While some have included the northwest striking structures as part of the Sevier orogenic belt (e.g. DeCelles, 2004), others have proposed they are, in fact, a younger set of Laramide thrusts overprinting older Sevier structures (Miller, 2003; Pavlis et al., 2014). While previous work suggests that overall contractional deformation in the Death Valley region is thought to have ended no later than 70 Ma (Fleck, 1970; Walker et al., 1995), Pavlis et al. (2014) challenged that view with a hypothesis of significant Laramide-age deformation in the region.

Following Mesozoic-Paleogene contraction, the Death Valley region was part of a Cordilleran highland analogous to the Andean Altiplano, commonly referred to as the Nevada Plano (Ernst, 2009). Erosion during this interval variably exhumed the previously deformed miogeoclinal strata, recorded now as a widespread unconformity beneath Neogene strata with rocks beneath the unconformity, ranging in age from Proterozoic basement to Cambrian (e.g. Pavlis et al., 2014).

The next period of tectonic activity was Neogene extension associated with the Basin and Range which continues today in a transtensional regime (e.g. Norton, 2011). Despite the consensus that the region is undergoing transtension at the present time, there are still disagreements about what forces produced the major Neogene structures of the Death Valley extensional terrane (e.g. Holm and Wernicke, 1990; Holm et al., 1992; Miller and Pavlis, 2005). The primary debate centers on the origin of low-angle detachment systems that are exposed immediately to the north of the Ibex Hills in the core of the Black Mountains (Figure 2.1). In that area the detailed mapping by Wright and Troxel (1984) formed

the basis of some of the early hypotheses on the role of low-angle normal faults in extension (Wright and Troxel, 1973). Further studies (e.g. see review in Miller and Pavlis, 2005) revealed that successively deeper structural levels are exhumed from SE to NW across the Black Mountains, from high-grade metamorphic rocks in the Death Valley turtlebacks to low-temperature brittle deformation in the SE. Although this initial observation supports the concept of a single detachment system across the Black Mountains, several observations are at odds with this generalization. Serpa and Pavlis (1996) and Pavlis (1997) noted that structures within the Death Valley turtlebacks in the central Black Mountains showed evidence of an exhumed, deeper-level detachment that formed prior to the main Black Mountains detachment system. Moreover, Miller and Prave (2003) and reviewed by Miller and Pavlis (2005) argued against the occurrence of even a single detachment, arguing instead for complex block rotations within a 3D, transtensional environment. Additional complications include significant structural relief on fault systems within the central Black Mountains that include the antiforms of the Death Valley turtlebacks and curvilinear fault surfaces within the Amargosa chaos (Figure 2.1). These curvilinear surfaces are often assumed to be primary corrugations in fault systems (Otten, 1976), but Mancktelow and Pavlis (1994) and Serpa and Pavlis (1996) presented evidence that these features are folds that developed coincident with the extension due to distributed transcurrent motions accompanying the extension.

In contrast to the extensional structures to the north of the Ibex Hills, structures immediately to the south and east are different in both structural style and kinematics. The Kingston Range Detachment system (Figure 2.1) represents the most significant extension that predates northwest directed movement and is exposed most clearly along the front of the Kingston Range (Figure 2.1) and farther south in the Halloran Hills (e.g. McMackin, 1992; Davis et al., 1993; Fowler and Calzia, 1999). Initial discussion of detachment faulting in the vicinity of the Kingston Range placed such structures in the context of major northwest directed extension (Burchfiel et al., 1983). However, later work on the Kingston Range Detachment has led to the current acceptance of a top to the southwest sense of movement (e.g. McMackin, 1992; Davis et al., 1993). The timing of movement along the Kingston Range Detachment is constrained by a 13.4 Ma hypabyssal sill, which is cut by the detachment, and the 12.4 Ma Kingston

Peak pluton which cross-cuts the detachment (Calzia, 1990; Fowler and Calzia, 1999; Calzia and Ramo, 2000).

To the west and northwest of the Kingston Range lies a suite of Tertiary aged basins which have been key in understanding the evolution of southern Death Valley (Figure 2.1) (e.g. Wright, 1974; Scott et al., 1988; Topping, 1993; Prave and McMackin, 1999). These basins include the China Ranch Basin (Wright, 1954; Scott et al., 1988) and the Dumont Hills Basin (Prave and McMackin, 1999) (Figure 2.1), however, other work has envisioned these basins as part of a larger scale feature, the Greater Amargosa-Buckwheat-Sperry Hills Basin (GABS Basin) (Holm et al., 1994). In the latter context, the GABS Basin has since undergone significant attenuation through a combination of the Black Mountain Detachment and Grand View Fault (Topping, 1993; Holm et al., 1994). In general, these basins record a basin filling sequence of alluvial fans and fanglomerates, coarse sandstones, and fine sandstones and mudstones (e.g. Prave and McMackin, 1999). Understanding the evolution of this basin system is important for the competing models of Death Valley extension. For example, interpretation of these Tertiary basins as half-grabens is consistent with later extension along a detachment (e.g. Topping, 1993). Alternatively, other authors documented evidence of at least two source directions for the fanglomerates of the basins, more consistent with a strike-slip driven, “pull-apart” model of basin development (Prave and McMackin, 1999).

The presence of such a suite of complex features that surround the Ibex Hills suggests an intricate extensional history interacted to form the structures in the Ibex Hills. In line with that suggestion, the structure of the Ibex Hills is complicated by a number of cross-cutting relationships and structural overprinting. The body of published works concerning the Ibex Hills is limited and thus far the range has primarily been mentioned in its relationship to the Black Mountain Detachment (e.g. Snow, J. K. and Wernicke, B. P., 2000; Holm and Wernicke, 1990). Mapping by Wright et al. (1968) identified a set of low angle faults in the northern Ibex Hills which at the time were interpreted as thrust faults, however, these are now known to be currently low-angle normal faults. These faults displaced rocks as deep as the gneissic basement of the range. The presence of these low angle faults has resulted in the interpretation that they represent an up-dip extension of the Black Mountain Detachment (e.g.

Holm and Wernicke, 1990; Snow, J. K. and Wernicke, B. P., 2000). In addition to the normal faulting in the range, a reverse fault within the Noonday Formation was also mapped by Esparza, (2012) in his MS thesis which places the Radcliffe Member atop the Mahogany Flats member.

In addition, the southern Ibex Hills is also the type locality for the Ibex Formation (Wright and Troxel, 1984), however, herein we will use the terminology of Petterson et al. (2011) which redefined the Ibex Formation as an equivalent to the Radcliffe Member of the Noonday Formation. Geologic mapping in the relatively small area of the Ibex Formation type locality was also provided by Wright and Troxel (1984).

2.4 METHODOLOGY

2.4.1 Geologic Mapping

Initial reconnaissance geologic mapping work was conducted before entering the field area using remote sensing and image interpretation. Based on this it was determined that there was potential for a low-angle normal fault cutting up-section to the north within east dipping strata, suggesting the potential for a component of south-directed normal fault movement. This was of interest as it supported previously unaccounted for southwest extension within the Ibex Hills.

Following this field work began in earnest during the spring of 2016 where evidence was found for northwest directed extension in addition to the south-southwest directed extension, suggesting multiple episodes of extension occurred in the Ibex Hills. Collectively these observations confirm that the kinematics of the Ibex Hills, along with the adjacent Saratoga Hills to the south, have not been thoroughly resolved and warranted further investigation. Field work and mapping in the study area continued into the spring of 2017.

Field mapping was done using QGIS software installed on a Windows tablet, both a Dell Venue 8 and a Lenovo Thinkpad Tablet 2, following the procedures of Pavlis et al., (2010). QGIS is an open source GIS software which utilizes the format of ESRI shapefiles as well as a number of other formats for raster files (e.g. .jp2). Before beginning field work each season, shapefiles were created for field stations and notes, geologic contacts, and orientation data. While in the field the shapefiles were then used to input measurement data as well as mapped contacts into QGIS. This methodology of electronic

mapping allows for the use of multiple overlays such as satellite imagery, topography, etc., and for contacts and station information to be recorded and overlain on each of these layers thereby giving a better context of the area while in the field. In addition, utilizing the GPS capabilities of the tablet in sync with QGIS provides high-resolution, real-time geolocation of data, including structural measurements and plotted line work. In areas of superb outcrop such as the Death Valley region and other arid regions, electronic mapping allows for a more efficient method of following contacts and structures while in the field, potentially resolving problems that were not as easily resolvable with traditional methods.

Orientation data of rock units and geologic structures were collected in the form of strike-and-dip measurements and taken with a Brunton compass and/or an electronic equivalent. This information was then plotted on the digital map while in the field, allowing for real time interpretations to be made and speculative contacts to be drawn and adjusted as new information is acquired. Digital mapping with the QGIS software also allows for the input of field stations so that labels, notes about outcrops, photographs and other data objects can be included in the digital geologic map database. Post fieldwork, each day, the contacts and structures were adjusted and further annotated based on photo-interpretation, in order to have the cleanest interpretation possible for the following day.

The final map was produced by exporting the QGIS map to Adobe Illustrator for further refinement. The layers created in QGIS can be exported and converted to Adobe Illustrator format. Overlays that were previously used, such as satellite imagery, topographic maps, etc., can also be imported into Adobe Illustrator. Further adjustments to the contacts can be made during this step, but the primary focus was to produce a visually appealing and presentable map.

2.4.2 Cross-Section Construction

In addition to the geologic map, a number of cross-sections were generated based on projections of the collected surface orientation data and linework. These cross-sections were created primarily using the software package Move by Midland Valley Ltd. (<http://www.mve.com/software>).

The contact lines and orientation data were exported from QGIS as shapefiles and were then imported into Move 2017. A digital elevation model (DEM) was downloaded from the USGS National

Map Download Client (viewer.nationalmap.gov/). A 1x1 degree area DEM, which included the Ibex Hills and Saratoga Hills, was imported into Move along with the geologic mapping data. In the process of the import the DEM was cropped to only the study area. Within the Move program the contacts and orientation data were then projected to the DEM to produce a 3-dimensional surface model of the geologic features.

Once the 3-dimensional surface model was constructed, section traces were drawn in Move using the “Section” tool. With the section trace drawn the intersection of the DEM with the section was then collected which provided the topographic profile. In addition, the intersection of contact lines with the section were also collected which provided reference for the projection of contacts into the subsurface. Bedding orientations were also projected to the section line to further assist in contact projections.

Prior to construction of cross-sections, the stratigraphy of the study area was entered into Move. These data included the names of the units, their thicknesses, and their ages. This useful feature allows the user to draw a line, assign it a unit, and then construct the units above and below automatically, based on the provided stratigraphy. It is important to note, however, that the stratigraphic thicknesses of some of the mapped units, namely the Beck Springs Dolomite, the Kingston Peak Formation, and the Noonday Formation, change dramatically within the study area. Therefore, the thicknesses entered into the Move program were not always used in the projections of the cross-sections. To counteract this issue the program allows for the change of unit thicknesses “on the fly” when constructing different sections, thereby not effecting the thicknesses for other areas of the map.

Contacts were then drawn in the cross-section using the mapped contacts and their orientations to project them into the subsurface. For the orientations of faults, some were well exposed and could be measured in the field and those data were used, however, in some cases the faults were not exposed. In those cases, the orientation of the fault was estimated using the three-point method and this was then used in the cross-section. Cross-sections were created with northeast and northwest trends, in order to capture the multiple extension directions that were interpreted in the field.

2.4.3 Kinematic Analysis

Due to the potential of multiple extension directions (Fleming and Pavlis, 2015) the analysis of kinematic data is vital to understanding the extensional history of the Ibex Hills and Saratoga Hills. To do this, slickenline orientations were acquired in the field. In this study we use the modified odd-axis method to analyze the fault slip data (Krantz, 1988, 1989; Bruhn et al., 2004). The modified odd-axis method for kinematic analysis assumes fault sets within a fault zone form a rhombohedral family of surfaces that slip in response to an incremental strain field that correlates to the driving stresses, with a geometry predicted by the theory of Krantz (1988). In this method, the fault planes, slip vectors, and the poles to the movement plane for each fault (equivalent to the B axis of a focal mechanism) are plotted on a stereonet. This results in clusters of poles to fault planes to which a best fit pole or clusters can be determined (e.g. Carvell et al., 2014). A great circle is then fit to the plot of movement plane poles (B-axes) and the pole to that plane is the “odd-axis” of Krantz (1988). The odd axis will be either the contractional axis or extension axis, which can generally be easily determined from a few slip surfaces with slip sense. The advantage of this approach relative to conventional paleo-stress techniques (Marrett and Allmendinger, 1990) is that all slickenside measurements can be used in the analysis, even if only a few have known slip sense. The intermediate and maximum extension directions are defined as the obtuse and acute bisectors of the movement plane pairs (Krantz, 1988; Carvell et al., 2014).

Also, because this area undoubtedly contains complex structural geometries inherited from both its Mesozoic history and from one or more phases of extension, it was anticipated that standard mapping alone may not unambiguously resolve the geometry of the study area. Thus, structure-from-motion (SfM) photogrammetry (e.g. Westoby et al., 2012) was used on a key outcrop which exhibited complex fold structures interpreted to represent older, Mesozoic events. The use of these techniques allows for the further analysis of the outcrop in 3-dimensions post-field, at the home institution, therefore assisting in an accurate interpretation of the geology (Fleming and Pavlis, 2018).

Using the model, the orientations of the folds throughout the outcrop were determined. Along with the data collected from the model there was also data collected from the field which consisted of the orientations of bedding and foliation planes as well as fold hinges, where accessible, and foliation-

bedding intersections. These data were then plotted on stereonet using Rick Allmendingers Stereonet program (<http://www.geo.cornell.edu/geology/faculty/RWA/programs/stereonet.html>).

2.5 RESULTS AND OBSERVATIONS

2.5.1 Map Units: Stratigraphy of the Mapped Area

The Death Valley region has a well-known stratigraphy (Figure 2.2), but the Ibex Hills contain complex lateral facies changes in many of the units. Thus, lithostratigraphic units vary across the mapped area and the stratigraphic features that were important to this study are described.

Neoproterozoic to Cambrian Stratigraphy

The bedrock of the Ibex Hills includes Mesoproterozoic basement and overlying Mesoproterozoic, Neoproterozoic, and Paleozoic sedimentary rocks with several unconformities bounding sequences within the stratigraphic assemblage (Figure 2.2). The most extensive and complex stratigraphic assemblage in the study area is the Pahrump Group which forms the base of the sedimentary cover across much of the region. The Pahrump Group is comprised of four formal lithostratigraphic units (Figure 2.2): the Crystal Springs Formation, Horse Thief Springs Formation, Becks Spring Formation, and Kingston Peak Formation (Wright et al., 1974; Mahon and Link, 2013). Overlying the Pahrump group are the Neoproterozoic Noonday, Johnnie, and Stirling Formations followed by Ediacran-Cambrian strata of the Wood Canyon Formation and overlying Paleozoic rocks (Figure 2.2) (Wright et al., 1974). In general, these formal units are sufficiently thick that they are insufficient as map units for the scale of this study. Thus, the units were subdivided into informal members described here.

The Crystal Springs Formation is the oldest sedimentary unit in the mapped area and is made up of carbonate and siliciclastic rocks intruded by mafic sills ranging up to 450-m in thickness (Wright et al., 1974). The sills are medium to coarse grained diabase and gabbro which have been dated to 1.084 Ga, and these intrusive contacts have created talc deposits throughout the area (Heaman and Grotzinger, 1992). The Crystal Springs Formation has traditionally been divided into three informal members, the lower, middle, and upper units, in addition to the Mesoproterozoic intrusions (e.g. Wright et al., 1974).

Diabase intrusions are abundant in the lower and middle Crystal Springs members but their presence in the upper member has been controversial. Calzia (2008) mapped intrusions within the upper Crystal Springs member in the Kingston Range, implying the upper member is a part of the same depositional sequence as the lower and middle members. In contrast, Mahon et al. (2013) recently redefined what had been mapped as the upper member of the Crystal Springs Formation as a separate, distinctly younger rock unit, the Horse Thief Springs Formation which spans ~150 m. This redefinition was based on detrital zircon studies which yielded Neoproterozoic zircons in the unit, indicating a maximum depositional age of 770 Ma, much younger than the ~1.1Ga dates of the mafic intrusions within the lower and middle members of the Crystal Springs Formation. We found no indications of intrusion into the upper Crystal Springs/Horse Thief Springs Formation, however, and will therefore use the terminology of Mahon et al. (2013).

The map presented herein displays the Crystal Springs as separated into Crystal Springs Lower Member and Crystal Springs Upper Member, with units of each shown where applicable (Plate 1). The lower member of the Crystal Springs consists of a basal conglomerate unit which marks the unconformity with the underlying basement rock (Plate 1 and Figure 2.2). Above this the lower Crystal Springs is dominated by the second map unit of cross-bedded and planar bedded quartzite (Figure 2.2). The units of the Crystal Springs Upper member consist of two layers of maroon to green-black shales which sandwich a unit of orange to tan dolomite (Plate 1). The upper unit of maroon shales marks the top of the Crystal Springs Upper Member; however, this space is also occupied by the diabase intrusive in some places. The overlying Horse Thief Spring Formation is marked by a thin, 5-10 meter, layer of chert-pebble conglomerate which contains clasts of the Crystal Springs Formation.

The Becks Springs Formation reaches ~350-m thick in the southern portion of the map area and is dominated by grey-blue dolomite interpreted to have been deposited in a shallow platform environment (Wright et al., 1974; Mahon et al., 2013). However, the overall thickness in the mapped area is highly variable. In the Saratoga Springs area, at the south end of the mapped area, the Beck Springs is at its thickest, but farther north it is drastically reduced as the unit is successively cut out along the overlying unconformities. In the central to northern Ibex Hills the Beck Springs Formation

thins to ~100 meters until eventually it is cut out of the sequence completely where Kingston Peak and Noonday Dolomite lie directly atop the Horse Thief Springs Formation (Plate 1). The basal Beck Springs Formation is a gradational contact with the underlying Horse Thief Springs. In the presented map (Plate 1) the contact between the Horse Thief Springs and Beck Springs Formation is marked by the first presence of the blue-grey dolomite of the Beck Springs Formation.

The Becks Springs Formation records paleoclimate change in two ways. First, the laminated carbonates in the lower Becks Springs are believed to record a flooding event within the Amargosa Aulacogen (Wright et al., 1974). Second, the contact between the Becks Springs Formation and the overlying Kingston Peak Formation marks a change from a relatively warm climatic regime into a glacial regime (Corsetti and Kaufman, 2005). Indeed, this transition and the overlying rocks of the Kingston Peak Formation are a major piece of evidence for the “Snowball Earth” hypothesis (Hoffman et al., 1998; Corsetti and Kaufman, 2005).

The Kingston Peak Formation contains a diverse range of rock types including siltstones, sandstones, and conglomerates (Wright et al., 1974; Corsetti and Kaufman, 2003). In this work the terminology of Macdonald et al. (2013) is used to map the members of the Kingston Peak Formation. Macdonald et al. (2013) mapped four member in the southern Death Valley region, KP1-4, however, in this mapping only the KP1-3 units were recognized in the mapped area (Plate 1). KP1 consists of thinly bedded shales and sandstones (Macdonald et al., 2013) and reaches ~250 m in thickness at the southern end of the map area (Plate 1). The contact with the underlying Beck Springs Formation was mapped at the base of the first thick sequence of thinly bedded shales (Plate 1). KP2 is unconformably above the lower KP1 member and consists of poorly bedded diamictites, predominately with a dark colored mudstone matrix in the map area, which contains clasts of the Crystal Springs Formation and basement rock (Macdonald et al., 2013). The KP2 member reaches ~375 m in thickness in the southern Saratoga Hills (Plate 1). The uppermost member of the Kingston Peak Formation that was mapped in this study was the KP3 unit which contains interbedded sandstones and shales along with layers of diamictites (Plate 1). The clasts of the diamictites range from Crystal Springs Formation to Beck Springs Formation.

The thickness of the Kingston Peak Formation changes significantly throughout the region and this change has been attributed to the presence of the Nopah Upland along the northern extent of the Amargosa Aulacogen (Wright et al., 1974), and presumably marks a Precambrian normal fault system. This paleogeographic feature is somewhat suspect, however, given the complexity of Mesozoic and Cenozoic deformation. The variability in thickness is apparent in the study area, however, showing a similar change as the Beck Springs Dolomite (Plate 1). In the Saratoga Hills and the nearby Saddle Peak Hills the Kingston Peak Formation is observed to be up to ~1200-m in thickness (Macdonald et al., 2013). Farther north in the Ibex Hills this thickness changes leaving only small lenses, only 5-10 meters or so in thickness, of KP3 sitting unconformably beneath the Noonday Dolomite Formation and above the Horse Thief Formation (Plate 1).

The ~200-m thick Noonday Formation overlies the Kingston Peak Formation and records a dramatic warming of Earth's climate at the end of the Snowball Earth (Corsetti and Kaufman, 2005; Mahon et al., 2013). Recent work by Petterson et al., (2011) has divided the Noonday Dolomite into three members, based in part on exposures of what Wright and Troxel (1974) had originally defined as the Ibex Formation with a type section in the southern Ibex Hills. The Petterson et al. (2011) stratigraphy includes the Sentinel Peak Member, Radcliff Member, and the Mahogany Flats Member, divisions that are retained in this study (Plate 1).

The Noonday Formation is overlain by two thick Neoproterozoic units: the Johnnie Formation and Stirling Formation. These units crop out extensively in the eastern and southeastern Ibex Hills (Figure 2.3). The Johnnie Formation consists of siliciclastic and carbonate rocks indicative of a shallow marine environment with periodic fluvial influences (Wright et al., 1974). A change to cross-bedded strata marks the transition from the upper Noonday Formation to the Johnnie Formation, and analyses of these beds indicates a northerly sediment source from a southeasterly striking paleo-slope (Wright et al., 1974). An oolite marker bed, part of the formal Rainstorm Member, (Stewart, 1972; Summa, 1993; Corsetti and Kaufman, 2005) is a convenient contact used here for division of the upper Johnnie Formation. The top of the Johnnie Formation is a major sequence boundary with incised valleys and channel conglomerates along the contact marking significant topographic relief prior to deposition of the

overlying Stirling Quartzite (Summa, 1993). In this study the Johnnie Formation was divided into three informal members, a lower mixed clastic-carbonate member, a middle shale-rich member, and an upper carbonate-dominant member. Much of the Johnnie Formation in the northern Ibex Hills is extensively faulted and attenuated and only the middle and upper members were exposed in that portion of the mapped area (Plate 1). The middle member of the Johnnie Formation in this study was defined by a base of pebbly, coarse tan dolomites. The middle member of the Johnnie Formation also contains purple, red, to brown mudstones. The upper member of the Johnnie Formation was defined at the base of the Johnnie Oolite (Plate 1). Above the Johnnie Oolite is ~150' of interbedded clastic rocks and a layer of tan dolomite.

The Johnnie Formation is disconformably overlain by the Stirling Quartzite which includes conglomerates and sandy carbonate facies but is, overall, siliciclastic. These deposits are generally interpreted to represent a marginal marine environment with lagoon pools (Corsetti and Kaufman, 2003). Based on the consistent orientation of cross-beds in the Johnnie Formation and the Stirling Quartzite, the sediment source was the same for the two formations (Wright et al., 1974). The age of the Stirling Quartzite has been estimated to be between 580-544 Ma based on fossil correlations and the overlying Precambrian/Cambrian boundary (Wright et al., 1974).

In the map area the Stirling Quartzite is divided into lower, middle, and upper members (Plate 1). The lower member is defined as a light colored quartzite which lies atop the upper Johnnie Formation (Plate 1). The middle member of the Stirling Quartzite consists of purple to brown shales which are overlain by a second sequence of quartzite which defines the upper member of the formation (Plate 1).

The Wood Canyon Formation is an Ediacran-Early Cambrian aged unit which conformably overlies the Stirling Quartzite (Mahon and Link, 2013) and is exposed at the northeastern edge of the Ibex Hills. The Wood Canyon Formation is divided into a lower member, middle member, and upper member (Corsetti and Kaufman, 2003). The lower member is predominately marine shale and mudstone with a few carbonate beds. The middle member is conglomeratic and interpreted to be continental in origin. The upper member consists of mixed siliciclastics and carbonates of marine origin. Ediacran

fossils are abundant in the lower member. These fossils underlie the Precambrian-Cambrian boundary in the uppermost section of the lower member (Corsetti and Kaufman, 2003).

The youngest pre-Cenozoic rocks exposed in the Ibex Hills and Saratoga Hills belong to the Zabriskie Quartzite that crops out along a fault contact in the easternmost flank of the northern Ibex Hills. In general, it is a well cemented quartzite which is light gray to pink in color (Mahon and Link, 2013). The Zabriskie Quartzite marks the final deposition of coarse sediment before the carbonate dominated system of the overlying Cambrian passive margin (Stewart, 1972; Prave, 1992).

Cenozoic Rocks

Pre-extensional to syn-extensional Miocene volcanic and sedimentary rocks are found in the Ibex Pass area, adjacent to the Ibex Hills. The stratigraphically lowest of the rocks in this sequence is a ~100-m thick dacite that lies in angular unconformity with underlying sedimentary units. Above the dacite is a ~250-300-m sequence of thick pyroclastic deposits that include pyroclastic flows, lahars, and intermittent lava flows (Canalda, 2009) (Luckow et al., 2005). This sequence is diverse and contains volcanic breccias and conglomerates that range in composition from trachyandesite to rhyolite (Canalda, 2009). Interbedded near the top of the pyroclastic sequence is a white to buff colored, 1-10m thick tuff (Figure 2.5). Topping (1993) correlated this unit with the ~9-10 Ma Rhodes Tuff (Topping, 1993), but Luckow et al., (2005) and Canalda (2009) have instead correlated this tuff with a similar tuff in the 12-14 Ma Wingate Wash volcanics of the Panamint and Owlshhead Mountains. The Ibex Pass volcanic sequence is capped by two megabreccia sheets separated by poorly exposed gravels. The lower megabreccia sheet consists primarily of granite clasts, and the other consists of carbonates that appear to be derived from Becks Springs Dolomite. Previous work has classified the granitic megabreccia as a landslide deposit with a Kingston Peak granite source (Topping, 1993; Holm, 1995), but Lauren Wright (personal communication to Pavlis, 1995) inferred that the rocks had a local source just east of the Ibex Hills.

2.5.2 Geologic Mapping

General Map Relationships

The Ibex Hills and the Saratoga Hills, in general, contain steeply dipping rocks, comprised primarily of the Proterozoic Pahrump Group (Plate 1). Only at the northern extent of the Saratoga Hills are younger rock units exposed, primarily of the Johnnie Formation in fault contact with the older Pahrump Group (Plate 1).

At the northern extent of the Ibex Hills the map pattern is significantly altered and is dominated by the Noonday and Johnnie Formations, along with portions of younger formations, especially in the northwest corner of the mapped area (Plate 1). Structural complexity increases dramatically to the north from relatively simple, homoclinal rocks from the Saratoga Hills to the central Ibex Hills to complexly faulted rocks in the northern Ibex Hills (Plate 1). The orientations of the rocks in the north are also much more sporadic, primarily due to the complex faulting, but dips are also generally shallower than those to the south (Plate 1).

One of the more striking differences between the Ibex Hills and the Saratoga Hills is the significant changes in stratigraphy between the two (Plate 1). In the Saratoga Hills the Beck Spring Dolomite is ~400 meters in thickness. However, in the central to northern Ibex Hills the Beck Spring Dolomite thins to less than 100 meters in thickness and eventually is cut out of the section completely along overlying unconformities (Plate 1). A similar pattern is seen for the Kingston Peak Formation which makes up the majority of the eastern flank of the Saratoga Hills with nearly 900 meters of the Kingston Peak section exposed (Plate 1). In the northern Ibex Hills the unit is all but cut out with only small lenses of the upper member exposed below the Noonday Dolomite (Plate 1).

An important map relationship in the Ibex Hills is the contact with the Cenozoic deposits of the adjacent Ibex Pass basin. The volcanics of Ibex Pass are exposed along the southeastern flank of the Ibex Hills and lie with angular unconformity on the older Pahrump Group rocks in a bowl-like exposure, bounded by faults (Plate 1). In this area the dominant volcanic unit is a purple colored, maroon to dark brown in weathering, phenocryst rich intermediate to felsic volcanic rock. This unit is mapped as a Tertiary aged andesite (Figure 2.3 and Plate 1). The phenocrysts consist of 1-3 cm plagioclase and

amphiboles. This andesite unit stratigraphically overlies a white, tuff layer which contains small grains of mica speckled throughout. This white ash, in turn, overlies an older felsic volcanic unit which sits on gravel deposits that are directly above the angular unconformity. Felsic intrusions permeate the andesite unit and weather reddish brown which phenocrysts dominated by plagioclase (Figure 2.3). Also present in the area is an outcrop of basaltic rocks which appear to overlie the felsic deposits, however, the contact is not exposed (Plate 1). The youngest volcanic unit exposed in the southern Ibex Hills is a felsic unit, mapped as rhyolite, which overlies the basalt flow (Figure 2.3 and Plate 1).

Canalda (2009) mapped a lithologically similar succession just to the north, on the northwest flank of the Saddle Peak Hills. At that location there are purple volcanic units which lay depositionally below a white tuff layer that is lithologically similar to the white tuff in the southern Ibex Hills. Given that a tuff would likely have significant lateral continuity, the two are tentatively correlated. Assuming this correlation suggests that the upper volcanics in the southern Ibex Hills represent localized deposits of a younger age (Figure 2.3). The geometry of the angular unconformity between the Ibex Hills volcanics and those farther northeast in Ibex Pass is similar (Canalda, 2009). Canalda (2009) recorded a post-depositional tilting of the volcanics of $\sim 30^\circ$ which is consistent with orientations measured in the southern Ibex Hills, albeit with a more northerly strike (Plate 1).

Also present in the Cenozoic deposits along the eastern flank of the Ibex Hills are multiple, mono-lithologic mega-breccias. The lowest of these megabreccias consists of clasts interpreted to be sourced from the Kingston Range granitic intrusion to the east (Topping, 1993; Fowler and Calzia, 1999; Calzia and Rämö, 2005). Farther up the section is another mono-lithologic megabreccia of the Beck Spring Dolomite. The megabreccia of Beck Spring Dolomite is exposed not only in Ibex Pass, but in the northern Ibex Hills (Plate 1). It is important to note that the granite megabreccia mapped adjacent to the central Ibex Hills (Plate 1) has not been previously discussed in the literature of the region. The implications of this deposit are significant to reconstructions of the area given the use of the Kingston Peak Granite deposits as piercing points for offset in the southern Death Valley region (e.g. Topping, 1993).

2.5.3 Fault Geometry in the Ibex Hills

The northern Ibex Hills exhibit a complex interaction between low-angle normal faults, a combination of northeast and northwest striking normal faults of moderate to high angle, and a steep oblique fault along the eastern flank of the range which are interpreted as having a dextral-normal sense of movement (Figure 2.2). To best understand the relative timing of these structures, field observations are as follows.

Low-Angle Normal Faults

We recognize five sets of currently low-angle normal faults in the northern Ibex Hills (Plate 1 and Figure 2.2). This sequence of faulting is not seen in the southern Ibex Hills nor within the Saratoga Hills to the south (Plate 1 and Figure 2.1). The structurally lowest fault in this sequence, dubbed Fault A herein, places primarily the middle Crystal Springs Formation in the hanging wall against both crystalline basement and the lower Crystal Springs (Figure 2.2). Structurally above Fault A is a series of low angle faults which carry Horse Thief Springs, the Mahogany Flats member of the Noonday Formation, and the Johnnie Formation in their hanging walls, dubbed Fault B, C, and D respectively (Figure 2.2). The structurally highest low-angle fault, dubbed Fault E carries the Stirling Quartzite and the Wood Canyon Formation in the hanging wall and is only exposed in the farthest northwest corner of the map area (Figure 2).

Field relationships clearly show that, in general, all of the currently low-angle normal faults are cross-cut by northeast striking normal faults (Figure 2.4). The relationship with northwest striking normal faults is slightly different as they cross-cut the low-angle faults up to Fault D (Figure 2.4). In addition, the relationship between the low-angle faults and the steep frontal fault to the east is also somewhat ambiguous (Figure 2.4). In the central Ibex Hills, the oblique frontal fault appears to cross-cut Fault A as well as Fault B (Figure 2.4). However, in the northern Ibex Hills the frontal fault appears to project into the adjacent basin to the northeast, essentially the northern continuation of the Ibex Pass basin (Figure 2.4).

In addition to their currently low dip, the low-angle normal faults intersect bedding at angles as low as $\sim 10^\circ$, however they range up to nearly 70° (Figure 2.5). Analysis of the cutoff angles of the low-

angle faults shows that ~80% of the faults have cutoff angles of less than 60° (Figure 2.5). This observations suggests the low angle faults either nucleated as relatively low-angle faults or they cut beds with a significant pre-extensional dip. The orientation of the cutoff lines was also estimated (Figure 2.5) to evaluate extension direction with a caveat that initial dip would complicate interpretation. These estimates are somewhat variable (Figure 2.5) with a spread ranging from southwest-northeast to southeast trends.

Fault A and Fault B both cut up stratigraphic section to the north-northwest (Figure 2.2). This relationship is less clear for the structurally higher Fault C as its geometry is partially obstructed by down to the northwest movement of the northeast striking normal faults as well as the hanging wall of Fault D. However, Fault C does appear to cut out section of the Radcliffe Member of the Noonday Formation toward the northwest, although it is possible this effect is due to lateral stratigraphic changes of the unit (e.g. Corsetti and Kaufman, 2005). Fault D has a more clearly defined geometry in the mapped area. In the east-central portions of the range the Johnnie Oolite is placed directly against the Mahogany Flats Member of the Noonday along Fault D (Plate 1 and Figure 2.4). Farther to the north and west Fault D cuts down section into the middle member of the Johnnie Formation (Plate 1).

These observed field relationships of the low-angle normal faults support the possibility of at least two extension directions related to the low-angle normal faults in the Ibex Hills based on the directions the faults cut down stratigraphic section. Specifically, Fault A and B are interpreted as motion on a top sw fault, or southwest directed extension whereas the structurally higher low-angle faults, as well as NE striking normal faults, are the result of northwest directed extension based on opposite stratigraphic cut-offs.

The northern Ibex Hills contain few well exposed fault surfaces, however, those that were yielded important kinematic information. Figure 2.6 shows the orientations of faults in the area alongside the collected slickenlines. The fault planes were collected primarily from Fault B, Fault C, and Fault A (Figure 2.4). The stereonet plot for measured fault planes show fault planes with opposing dip directions present in the study area which converge around a slightly plunging southwest to northeast trending axis (Figure 2.6). In general, the current dips of the low-angle normal faults plotted in Figure

2.5 range from 10-40°. Figure 2.6 also displays the slickenlines we measured in the northern Ibex Hills alongside their respective fault planes. The rake of the slickenlines are all currently greater than 70 degrees (Figure 2.5).

A plot of all of the measured poles to low angle faults shows a distinct scattering of fault poles along a steeply dipping, NW striking great circle (Figure 2.6). This distribution of fault surfaces indicates potential folding which may be similar in origin to, but geometrically distinct, from that inferred to the north by Mancktelow and Pavlis, (1994). Alternatively, the fault plane orientations could simply be a product of their original corrugated geometry being curved along strike which can also be seen to some extent with the nearby Kingston Range Detachment (Fowler and Calzia, 1999). This hypothesis is analyzed further below.

Figure 2.7 (see associated .pdf) shows the cross-sections developed for the map area. The interpretations of the low-angle normal faults within the cross-sections are two-fold: the structurally lower Fault A and Fault B represent earlier southwest directed movement perhaps temporally associated with the Kingston Peak Detachment (e.g. Fowler and Calzia, 1999), whereas Fault C and the structurally higher normal faults were the result of later northwest directed movement likely related to the northeast striking normal faults seen in the Ibex Hills, albeit as an earlier phase of deformation as they are cross-cut by them (Figure 2.4 & 2.7). The interpretations of the low-angle faults are based on the fact that Fault A and Fault B both cut down stratigraphic section to the south (Plate 1 and Figure 2.4). The orientation of the fault-bedding cutoff lines is consistent with multiple extension directions given that they trend to both the southeast and the southwest-northeast (Figure 2.5). In addition, we suggest that the current fault plane orientations suggest either folding about a southwest-northeast axis or reflect an original corrugated fault geometry, both of which are consistent with southwest directed extension along the faults. The interpretation of Fault C as a northwest directed structure was based on the field relationships and projections of the structurally lower faults in cross-section (Figure 2.4) which suggested the fault cross-cuts the structurally lower faults to the northwest.

Younger Normal Faults

Cross-cutting the low-angle normal faults of the northern Ibex Hills are north-northeast striking, down to the northwest, normal faults as well as some generally high-angle northwest striking faults (Figure 2.4). The orientations of these normal faults range from relatively moderate dips of $\sim 50^\circ$ to very high dips of 80° or greater. Figure 8 shows a stereonet of the moderate to steeply dipping normal faults in the northern Ibex Hills. The majority of the measured faults in the northern Ibex Hills strike to the northeast with a strike range of $\sim 30^\circ$ to $\sim 70^\circ$ (Figure 2.8). A second family of faults can be seen in the data (Figure 2.8) which strike predominately north-south to northwest-southeast. These north-south striking faults tend to dip at higher angles than the predominately northeast striking faults with many of them oriented near vertical to vertical (Figure 2.8).

Figure 2.5 also shows the geometry of the fault-bedding cutoffs for the higher angle normal faults in the northern Ibex Hills. The majority of the faults have cutoff angles of $>60^\circ$, although some fall below that mark (Figure 2.5). The range of cutoff angles is likely due to pre-extensional dip of the beds. A key insight of the fault-bedding cutoffs, however, is the orientation of the cutoff lines, which consistently trend northeast-southwest (Figure 2.5). This cutoff line orientation is consistent with more recent northwest directed extension recorded by normal faults in the Ibex Hills.

The influence of both the northeast and northwest striking normal faults in the northern Ibex Hills can be seen most clearly in the southern portion of Figure 2.4 where they cut into basement rock and displace the Crystal Springs Formation and the overlying Horse Thief Springs Formation. The faulting in the area results in a sequence of blocks in which the hanging walls of the faults are being dropped down to the north and to the northwest (Plate 1 and Figure 2.4).

In the field, the relationship between the northeast-southwest striking faults and the low-angle normal faults is consistently that of the former cross-cutting the latter (Figure 2.4). Similarly, the northwest striking faults clearly displace the low-angle normal faults but their relationship with the northeast striking normal faults is more ambiguous as there are limited locations showing the cross-cutting relations between the two families of faults.

Farther south in the study area in the Saratoga Hills, the deformation decreases significantly in its apparent complexity (Plate 1 and Figure 2.9). Most notably the low-angle normal faults in the style of the northern Ibex Hills are mostly limited to a northeast striking fault which displaces the Johnnie Formation down to the north-northwest (Plate 1 and Figure 2.4 and 2.9), although another small displacement of the Beck Springs Formation is present farther south (Plate 1). Elsewhere in the southern Ibex Hills and Saratoga Hills, the faulting predominately consists of moderate to high-angle normal and oblique faults which strike either to the northeast or the northwest (Figure 2.9).

Despite the similar orientations of the higher angle normal faulting in the southern Ibex Hills to that in the northern Ibex Hills (Figure 2.4 and 2.9), the cross-cutting relationships are somewhat different. At the southern extent of the Ibex Hills a pair of prominent northwest striking, high-angle faults clearly truncate smaller north-northeast striking faults (Figure 2.9). These north-northeast striking normal faults in general have a down to the northwest sense of movement, however, some have a minor down to the southeast sense of displacement. However, farther south in the Saratoga Hills the high-angle, west-northwest striking faults appear to be truncated by northeast striking normal faults bringing down the Johnnie Formation in the hanging wall (Figure 2.9).

Eastern Boundary Fault

The Ibex Hills is bounded on its eastern flank by a very steeply dipping, north-south to northeast-southwest striking fault (Figure 2.4 and 2.9; Plate 1), herein referred to as the Eastern Boundary Fault. The trace of the fault is most prominent along the central portion of the range. Along the northern extent of the Ibex Hills the trace of the Eastern Boundary Fault is tentatively projected as continuing into the adjacent Ibex Pass basin, to the northeast, however it's trace is not exposed. The continuation of the Eastern Boundary Fault to the northeast is interpreted as a splay of the primary fault trace as it does not appear to continue farther into the range (Plate 1). In the southern portion of the Ibex Hills the Eastern Boundary Fault projects into the adjacent Tertiary basin (Plate 1 and Figure 2.6).

In the northern portion of the map area the Eastern Boundary Fault carries the upper Johnnie Formation and Stirling Quartzite in its hanging wall (Figure 2.4). Farther south the fault cuts down section and carries portions of the Noonday Formation, the Beck Springs Dolomite, and eventually the

upper Crystal Springs Formation in its hanging wall (Plate 1). Projecting the Eastern Boundary Fault trace to the north suggests that the Johnnie Formation and younger rocks of the northernmost Ibex Hills are in the footwall of the fault (Plate 1). Given this correlation, the Eastern Boundary Fault appears to have an approximate heave of 4 km, based on the map distance between the Stirling Quartzite in the central Ibex Hills to that in the north (Plate 1).

2.5.4 Folding in the Ibex Hills

Within the Ibex Hills there are outcrops which exhibit ductile deformation ranging from open to isoclinal folding (Figure 2.10 and 2.11) (Fleming and Pavlis, 2016). The folding is best seen in the Radcliffe member of the Noonday Formation. The focus of fold studies was primarily conducted on a large outcrop in the northern Ibex Hills which exhibits significant, outcrop scale folding with clear curved fold axes visible in the field (Figure 2.10).

The focus outcrop is comprised of interbedded shale and carbonate in the upper part of the Radcliffe member. Lithologically the Radcliffe member of the Noonday Formation, consists of three distinct units (Wright and Troxel, 1984). The lowest ~5 meters is a basal conglomerate marking an erosional contact with the Sentinel Peak member (Wright and Troxel, 1984). The middle portion of the Radcliffe member spans ~100 meters of section and consists of a dolomite member and a thick (~90 m) member comprised of arkose and shale (Wright and Troxel, 1984; Corsetti and Kaufman, 2005). Atop the dolomite and arkose member is a limestone, an interbedded shaly limestone, and dolomite sequence (Corsetti and Kaufman, 2005; Wright and Troxel, 1984).

The outcrop itself is approximately 60 meters in length and 10 meters in height, exposed in an east-west channel in the northern Ibex Hills (star in Figure 2.4). The face of the outcrop is relatively steep and near vertical in places. The steepness of the outcrop face makes it difficult to conduct traditional map-based analysis making it a good candidate for 3D analysis using SfM photogrammetry models.

The outcrop lies within a valley that exposes highly folded upper Radcliff member beds. The Radcliffe member in the outcrop area is bounded to the southwest and east by down to the east normal faults (Figure 2.4). The fault to the southwest cuts out lower Radcliff member, placing the folded upper

beds against the Sentinel Peak member, which lacks the complex mesoscopic folding due to its massive bedding. To the northeast the Mahogany Flats member of the Noonday lies in stratigraphic continuity with the Radcliff member (Figure 2.4) but also lacks the conspicuous folding seen in the underlying Radcliff member, indicating detachment along layering near the top of the Radcliff, likely related to offset along the surface of Fault C.

The folds exhibited within the outcrop range from open to sub-isoclinal with the tighter folds typically within the interbedded shales (Figure 2.10). Changes in fold axis orientation are apparent across the outcrop varying from steeply plunging to the northeast to more gently plunging to the southeast. A prominent spaced, fanning cleavage is present throughout the outcrop and, in general, intersects the limbs of the folds at high angles (Figure 2.11). Small scale, steeply dipping faults, ranging from ~1-3 meters of apparent offset, permeate the outcrop and obstruct the bedding traces.

2.5.5 Kinematic Analysis

Kinematic analysis was conducted on two dozen pairs of fault planes and associated slickenlines for the Eastern Frontal Fault using the Odd Axis Method of Krantz (1988) (Figure 2.12). In addition, the same method was used on a small number of the low-angle normal faults of the Fault B. These data were limited due to limited preservation of faults surfaces in the area (Figure 2.12).

The Eastern Boundary Fault does in fact exhibit an orthorhombic fault geometry (i.e. two sets of conjugate fault systems), albeit with a more dominant north-northeast striking set (Figure 2.12). In general, the slickenlines have rakes of 30° or less, mostly from the south-southwest (Figure 2.12). The slickenlines were paired with their corresponding poles to fault planes and a best-fit movement plane was created for the pair, with the movement plane poles (B axes) plotted (Figure 2.12). The result is a distinct cluster of B axes (Figure 2.12B) plunging moderately to steeply to the north. With a master fault dipping steeply to the ESE, this B axis cluster, together with the corresponding odd axis (red dot, Figure 2.12B) and known stratigraphic shifts indicate the odd axis is an extension direction and the eastern boundary fault is an oblique, dextral-normal slip fault. This is in accordance with the average orientation of the fault and its inferred slip vector, also plotted on Figure 2.12B.

Combining the results of the kinematic data of the Eastern Boundary Fault (Figure 2.12) with general map pattern, the fault is interpreted to have an oblique, right-lateral sense of movement with the hanging wall moving down to the east (Plate 1 and Figure 2.3). This interpretation was supported by the fact that the slickenlines along the Eastern Boundary Fault are predominately shallowing plunging and trending to the south along the approximately north-northeast fault trace. Together with the map pattern of younger units displaced to the east the field data supports a “odd-axis” of shortening to the south-west.

The same methodology was also used for the low-angle normal faults of Fault B (Krantz, 1988). Although the data set was limited for these faults, there was a consistent geometry seen between the slickenlines and the fault planes which align well with the general map pattern, suggesting even the limited analysis sheds light on the kinematics of the study area. Figure 2.12C shows the results of the Krantz (1988), as adapted by Bruhn et al. (2004), methodology which gave an “odd-axis” trending to the west-northwest and plunging $\sim 60^\circ$. A steeply plunging to vertical “odd-axis” requires dip-slip or near dip-slip (Krantz, 1988; Krantz, 1989). Stratigraphic shifts and slickenline kinematics clearly indicate this odd axis is the contraction axis. Thus, with an intermediate strain axis (B axis) to the south, the extension axis would currently plunge shallowly to the ESE. Note, the low-angle fault analysis is also consistent with east range tilting, assuming original Andersonian (vertical) stress/strain axes (Figure 2.12C).

Given the limited data set for the kinematics of Fault B, the measured fault planes were also rotated based on an estimated range tilt for the Ibex Hills (Figure 2.12D). This estimate of tilting was derived from measurements in the volcanic deposits in the southern Ibex Pass area which happen to correlate well with previous tilting estimates used by Canalda (2009) of $\sim 30^\circ$ about a nearly north-south horizontal axis (Plate 1). This estimate of 30° is also supported by cross-section reconstructions of the Saratoga Hills, which are discussed in the following sections. When the tilt is restored for the low-angle faults, the currently southeast dipping faults dip to the southwest (Figure 2.9). In addition, the west to northwest dipping faults are restored to higher dips but still in the same direction (Figure 2.9). The presence of west-southwest dipping, low-angle faults after restoration of range tilt, further supports the

presence of southwest directed extensional structures in the Ibex Hills. Figure 2.9D shows the fault planes together with the best fit plane to the B-Axes and their geometry suggests an ~E-W directed slip vector (i.e. 90°) from the fault plane-B-Axes best fit intersection). However, given the potential for syn-extensional, clockwise rotation in the region (e.g. Serpa and Pavlis, 1996) the slip vector likely had a more southwesterly orientation originally.

2.5.6 Fault Reconstructions

To develop a reasonable model for the structural history of the Ibex Hills and the Saratoga Hills, estimates of fault displacement were reconstructed using cross-sections made throughout the ranges (Plate 1). The results for the displacement along the low-angle faults and the higher-angle, northeast and northwest striking faults are presented along with the reconstructed sections (Figure 2.13, 2.14, and 2.15: see associated .pdfs). Table 1 summarizes the total amounts of heave and stretch for sections A-A', B-B', and D-D' to best compare the extension recorded in the norther Ibex Hills and the Saratoga Hills.

Figure 2.13 shows the cross-sections from the study area after fault movement along the high-angle normal faults and oblique faults is restored. The restoration of the Saratoga Hills is complete at this phase as there were no mapped low-angle faults like those seen in the northern Ibex Hills (Figure 2.13B). Therefore, analyzing the restored section of the Saratoga Hills sheds light onto the pre-extensional geometry, which is obscured by the low angle faults to the north (Figure 2.13).

The total heave calculated from restoration of the section in the Saratoga Hills is 1.7 km (Figure 2.13B). After reconstruction of the extension, a northwest trending fold pair remains within the units and is interpreted to represent a pre-extensional fold geometry for the Saratoga Hills. Given that the high-angle normal faults cross-cut the low-angle faults across both the studied ranges the folding seen in the restored Saratoga Hills section must predate the most recent northwest directed extension. The approximate dip of the layering in the restored section of the Saratoga Hills is $\sim 30^\circ$, which is consistent with dip measurements observed in the Tertiary volcanics of Ibex Pass (Canalda, 2009) as well as the mapping presented herein (Plate 1). Taken together this suggests that prior to extension bedding in the range was gently dipping to flat lying, with a steeper dip on the short limb of the fold pair.

Restoration in the northern Ibex Hills was a more complex process given the interpretation of two phases of extension at nearly ninety degrees to each other (Figure 2.14 and 2.15). Figure 2.14 shows the steps of restoring B-B', the restoration first restores motion along the high-angle normal faults (Figure 2.14B). After high-angle normal faulting is restored the earlier geometry of the low-angle normal faults is revealed. At this stage, however, the effects of range tilting remain, because the low-angle normal faults retain their easterly dip (Figure 2.14B); i.e. apparent thrust motion but younger-on-older stratigraphic juxtaposition. To correct for this tilt, the section was rotated 30° counterclockwise about a horizontal axis oriented 005° (Figure 2.14C). This rotation axis is based on the tilt of Neogene volcanic and sedimentary units above the unconformity to the south. Note that the origin of this tilt is unconstrained in the mapped area, but presumably represents a deeper detachment as envisioned by Serpa et al. (1988), relatively young folding across the range (e.g. Miller et al., 2005) or both. Figure 2.14C also includes projected beds in the footwall of Fault C, although the orientations of these beds is not well constrained as they are currently below the Tertiary basin to the east of the Ibex Hills (Figure 1). Given the presence of faulted Johnnie Formation atop much of the northern Ibex Hills (Plate 1) two inferred faults were projected into the restoration at the point of Figure 2.14C. Without these faults the Johnnie Formation could not be restored to a geometry consistent with the underlying section. Given the general presence of northeast striking structures in the Ibex Hills this inference of them in the Fault D hanging wall is a reasonable assumption. Because Fault D is younger than Fault C from field relationships, the next step was to restore Fault D, collectively with the inferred faults of its hanging wall, with a horizontal displacement of ~1.4 km (Figure 2.14D). Finally, Fault D (Figure 2.14E) was restored with a heave of ~3.2 km. The total heave along Faults C and D is ~4.6 km (Figure 2.14) and the total heave of the high-angle normal faults across the section was 550 m (Figure 2.14B). Taken together this restoration indicates 5.1 km of northwest directed, horizontal displacement for the northern Ibex Hills (Table 1).

The restoration of section A-A' followed the same initial steps of that of B-B', specifically the restoration of high-angle normal faults and range tilting, with the same range tilt used in section A-A' (Figure 2.15A-C). Fault E was also contained in A-A' and was restored alongside the higher angle

normal faults (Figure 2.15B) as it is interpreted as part of the northwest directed extensional regime and restoration of this section was intended to highlight southwest directed extension. The hanging walls of Fault C and Fault D were removed for the rest of the restoration as they were restored out of the line of section from the previous steps (i.e. Figure 2.14). As in the A-A' restoration the footwalls and hanging walls of the faults were projected upwards using the known stratigraphy to constrain the reconstructions (Figure 2.15C). That is, because younger faulting and erosion have excised part of this footwall, we assume a simple, continuous section was present prior to faulting; a reasonable assumption unless unrecognized thrust systems were present prior to extension. A key difference in the projected stratigraphy for A-A', as opposed to B-B', was the lack of the Kingston Peak Formation and Beck Springs Formation which are not present below the Noonday Formation in ranges north of the Ibex Hills (Wright et al., 1974). Restored movement along Fault A and Fault B totaled ~2.4 km of heave (Figure 2.15E). The effects of the high-angle fault restoration were minimal, therefore, the southwest directed extension in the range is primarily accommodated by the low-angle faults (Figure 2.15) with a net horizontal displacement of ~2.4 km across the mapped area (Table 1).

2.5.6 Fold Analysis

Initial observations of the Ibex Hills field focus site in the Noonday Formation showed clear signs of a complex fold geometry. Non-cylindrical folds are apparent at the outcrop scale, with mesoscopic folds showing curved hinges and changes in fold axis orientation within ~1m observed in some well exposed structures.

To better understand the geometry of these non-cylindrical folds, separate domains of the outcrop were analyzed and their fold axes determined from groupings of 2 or more planar measurements in each domain. These domains were determined based on perceived changes in fold orientation while in the field as well as analyzing the point cloud models. In addition to the field data, measurements from the point cloud were also plotted with the field data.

The fold axes determined from both the field measurements and the corrected point clouds are indistinguishable and indicate F1 axes scattered around an ~E-W, gently-plunging cluster that shows significant variation in plunge consistent with the observed curved fold axes (Figure 2.16A). Further

validation of this scattering of F1 fold orientations is seen in a plot of foliation-bedding intersections (Figure 2.16B) which is indistinguishable from the fold axis plot (Figure 2.16A), an expected result for an axial planar cleavage. The similarity in foliation-bedding intersections with F1 axes supports the field observation that the cleavage is associated with the main close to sub-isoclinal folds representing D1 structures.

Cleavage orientations alone were also plotted, coming from both the outcrop as well as nearby exposures of the Radcliffe Member (Figure 2.17). The poles to the cleavage measurements, while somewhat scattered, fit to a north-northwest striking, southwest dipping great circle (Figure 2.17). The pole to this great circle suggests a fold axis of the D1 cleavage about a shallowly plunging, northeast trending fold axis (Figure 2.17). This fold axis of the cleavage planes is in line with the great circle distribution of the F1 fold axis, further supporting a D2 event which refolded the initial structures.

With this geometric perspective, we then took the high-resolution 3D lines representing layers traced on the 3D model, together with the orientation data, and developed a 3D geologic model of the outcrop using Move 2016. This model was developed from serial sections aided by extrusions parallel to local fold axes, and illustrates the refolding shown as conspicuous curvature of the main folds in the outcrop (Figure 2.18-as 3Dpdf). Specifically, the layers form type 2 interference patterns (terminology of Ramsay,1967) but the 3D visualization shows their true geometry rather than a simple planar intersection of the complexly folded surface. In addition to the folding, the 3-dimensional mapping of the bedding traces also highlighted a south verging thrust fault which divides the outcrop (Figure 2.18) but was not immediately apparent in the field. The thrust fault surface is parallel to the initial fold axes and the adjacent beds exhibit drag into the fault. It is therefore interpreted as a product of D1 deformation which was then overprinted by D2 (Figure 2.18).

2.6 DISCUSSION

2.6.1 Structural Evolution of the Ibex Hills and Saratoga Hills

The geology of the Ibex Hills and Saratoga Hills records a multi-phase deformational history which includes at least two-phases of contraction and two phases of extension. The contractional history is best displayed by the results of working with the high-resolution 3D outcrop model. In this area,

which is presumably indicative of the mapped area contractional structures, early NW trending (modern coordinates) folds were produced. This early deformation was an intense, ductile deformational event associated with a conspicuous axial-planar cleavage. These early fold systems were then clearly overprinted by NE trending open folds that produced curvature in the F1 fold axes as well as folding of the pressure-solution cleavage. Note, that this contractional history is geometrically distinct from overprints recognized just to the east in the Resting Spring and Nopah Ranges where Pavlis et al. (2014) documented early NE trending structures associated with a low-grade cleavage overprinted by NW trending fold and thrust systems. This suggests either this region experienced a distinctly different kinematic history, or the Ibex Hills have experienced a rigid body, vertical axis rotation of $\sim 90^\circ$; a problem that is discussed further below.

The earliest extensional phase recorded in the Ibex Hills is a top to the southwest movement along Fault A and Fault B (Plate 1 and Figure 2.4). Initial map observations supported this hypothesis as the traces of both Fault A and Fault B appeared to cut up section to the north (Plate 1). Additionally, the measurements of faults surfaces along Fault B, when corrected for range tilting, dip predominately to the southwest and west-southwest (Figure 2.12D). Restoring the movement along Faults A and B results in an estimated stretch of ~ 1.54 in the range, which approximates the southwest extension recorded in the northern Ibex Hills (Table 1).

Importantly, no previous mapping of the Ibex Hills has documented these southwest directed extensional structures. Recognizing these older extensional structures in the Ibex Hills is key for the accuracy of future models of the region as previous models have either omitted the range or included it as a portion of the Black Mountain Detachment Fault (e.g. Holm and Wernicke, 1990; Snow and Wernicke, 2000).

Cross-cutting Fault A and B in the northern Ibex Hills are Faults C and D, interpreted here as originally down to the northwest normal faults (e.g. Figure 2.14). These faults record ~ 4.6 km of heave to the northwest and place the upper Noonday Formation and younger rocks atop the crystalline basement of the region (Plate 1). More recent northwest directed extension is also present in the Ibex Hills as well as farther south in the Saratoga Hills (Plate 1; Figure 2.13 and 2.14). This extension is

represented by moderate to high-angle normal faults which clearly cross-cut the currently low-angle faults, Fault A-E.

The most recent faulting, which may be coeval with the youngest, northwest directed extension, occurred along the Eastern Boundary Fault (Plate 1; Figure 2.4). The presence of the Eastern Boundary Fault is interpreted here as related to the most recent phase of transtension in the Death Valley region as it cross-cuts earlier normal faulting in the Ibex Hills (Figure 2.4) (e.g. Norton, 2011). Although the trace of the Eastern Boundary Fault is obscured in the northern portion of the study area, the fault displaces the Johnnie and Stirling Formation ~4 km to the southeast relative to the footwall positions of these rocks (Plate 1).

2.6.2 Implications for Extensional Models of the Region

Previous workers have associated the faulting in the northern Ibex Hills with the Black Mountain Detachment Fault (e.g. Holm and Wernicke, 1990; Snow, J. K. and Wernicke, B. P., 2000) and one of the principal goals of this study was to analyze this possibility. Based on the mapping and structural analysis presented herein, the data does not support a single detachment surface, which is necessary for Black Mountain Detachment Fault and associated rolling-hinge model for the Death Valley region (e.g. Snow, J. K. and Wernicke, B. P., 2000). Regardless of the extension directions which are preserved in the Ibex Hills, the reconstructions presented here do not indicate the presence of a single detachment to which the Faults A-E sole into, necessitated by the rolling-hinge models of the area. Based on cross section restorations the northwest directed displacement recorded in the Ibex Hills was, in total, ~5 km (Figure 2.14). The fact that no large-scale displacement is needed to restore Faults C and D is difficult to rectify with them being part of a regional detachment surface that extended far to the east and south of the Ibex Hills. While the Ibex Hills have no doubt been transported along other regional structures, for example the Sheephead Fault, or faults within the Ibex Pass area (e.g. Canalda, 2009) it does not appear a single structure is responsible for such movement. One variant on the single detachment model that is allowable from the data is that the Ibex Hills represent a piece of the extensional detachment system that was close to, or at, the breakaway for the Black Mountains detachment. That is, motion on the northwest directed faults is limited to ~5km which could be because these rocks were left behind as deformation

progressed to the northwest along a rolling hinge. Note, however, that even this conclusion is at odds with reconstructions of the extension by Snow and Wernicke (2000) which would place the breakaway significantly south and east of the Ibex Hills.

Further complicating the application of the rolling-hinge model to the Ibex Hills is the evidence for southwest directed extensional structures that pre-date the northwest directed structures. While the presence of such structures does not necessarily disprove a potential detachment surface in the range, it does require a reassessment of the assumptions made by previous models (e.g. Holm and Wernicke, 1990; Topping, 1993). These previous works suggest a single extension direction for the Ibex Hills, which based on the mapping and associated data presented herein, is not the case (Plate 1).

Contrary to the single detachment model, the data presented in this study supports two phases, southwest and northwest directed extension, of currently low-angle normal faulting exposed in the northern Ibex Hills (Plate 1). The existence of southwest directed extension is supported by mapped fault surfaces which cut up section to the north in the study area, namely Faults A and B (Figure 2.4). Further supporting the interpretation of southwest directed normal faulting are the current fault plane orientations in the range (Figure 2.6 and 2.12). While unexposed in the northernmost area of the map, fault orientations of Fault B most commonly dip to the southwest and when rotated about the inferred range tilting of the area, dip shallowly to the southwest (Figure 2.12D).

In addition to the orientation data, the stratigraphy of the footwall of Fault B also suggest a northeasterly source (Plate 1; Figure 2.15). The unconformity below the lower Noonday Formation is preserved and sitting atop the Horse Thief Formation in the northern Ibex Hills (Plate 1). If, in fact, the footwall material was derived from the southeast, implied by northwest directed extension, this unconformity is out of place. Ranges to the southeast, such as the Saddle Peak Hills, contain the Kingston Peak Formation and Beck Springs Formation below the Noonday Formation (e.g. Wright et al., 1974; Mahon and Link, 2013). Instead, the presence of the basal Noonday unconformity above the Horse Thief Formation suggest a source to the east, perhaps as far as the Nopah Range, now ~25 km away (Figure 2.1).

2.6.3 Genesis of Curved Fault Surfaces in the Ibex Hills

At large scale the northern Ibex Hills display a broad synformal structure in the map traces of units (Plate 1). Stereonet analysis of low-angle fault orientations in the area, beyond those of only the Fault B, supports this observation and suggests an apparent curvature of the fault surfaces about a northeast-southwest directed axis (Figure 2.6). While some of this is certainly due to different initial geometries of the various low-angle normal faults mapped in the area (e.g. Fault A vs Fault D), the curved geometry is observed at all structural levels (Figure 2.12C). One explanation of this curved fault geometry is the presence of corrugated, “spoon” shaped fault surfaces. This corrugation coupled with a listric geometry of the low-angle faults could explain the overall “bowl” shape of the northern Ibex Hills (Plate 1).

The presence of corrugated normal faults has previously been recognized in Death Valley as far back as the work of Otten (1976) in the Black Mountains. More recent work has continued to model the mechanisms responsible for the corrugations and apparent extensional folding seen the southern Black Mountains (e.g. Mancktelow and Pavlis, 1994). In addition to the Black Mountains, the Kingston Range Detachment has also been observed as a corrugated, non-planar fault surface (McMackin, 1992; Fowler and Calzia, 1999). In all cases, such corrugations in the fault surfaces trend parallel to the extension direction.

Another possibility is that the curved fault surfaces have, in fact, been folded after their initial movement. The mechanism behind this folding is not immediately obvious, however, it would most likely be related to more recent, transtensional kinematics in the Death Valley region (e.g. Topping, 1993; Serpa and Pavlis, 1996; Norton, 2011). Previous work by Mancktelow and Pavlis (1994) proposed the presence of transcurrent related folding in southern Death Valley. This process essentially requires a step-over in a transcurrent system which results in low-angle detachment faulting which is then rotated about a vertical axis during the progressive shear of the transcurrent faulting.

The most convenient regional structure which could account for post or syn-extensional transcurrent deformation would be the Sheephead Fault which is mapped just to the north of the Ibex Hills (Figure 2.1). The sense of offset along the Sheephead Fault has been debated with some supporting

a right-lateral fault (e.g. Renik and Christie-Blick, 2013) while others suggest a left-lateral sense of motion (e.g. Topping, 1993; Serpa and Pavlis, 1996) along the fault. The determination of the Sheephead Faults kinematics is not the focus of this study, however, the implications of this debate for the Ibex Hills cannot be ignored as a right-lateral Sheephead Fault is a better fit for the transcurrent fold model of Mancktelow and Pavlis (1994), as the model results in a sequence of southwest directed faults, given an easterly striking right-lateral fault, which are later rotated and folded. However, evidence presented in the next chapter is more consistent with a left-lateral Sheephead Fault. Considering this, perhaps a different model is required to fold the low-angle faults of the Ibex Hills. One option for this is a step-over in a left-lateral Sheephead Fault which would likely result in compression of the northern Ibex Hills and thus fold the older normal faults in the range.

Given the two options discussed above for the curved fault planes in the northern Ibex Hills, the model of more recent folding of the faults, regardless of the kinematics of the Sheephead Fault, is preferred over the explanation requiring initial corrugated fault geometry. This preference is based on the folding of older F1 fold axes and related foliations which aligns with the curvature seen in the faults (Figure 2.6). In addition, the general map pattern shows a synformal structure for not just the fault traces but also the rock units in the area (Plate 1). If there was no post-extensional folding, and only corrugations, one would only expect a curvature of the fault surfaces and not rock units and their structural fabrics. The mechanism behind such post-extensional folding in the Ibex Hills is not obvious, however, transverse structures are present in the Ibex Hills and Saratoga Hills, most notably the Eastern Boundary Fault. The kinematic analysis, along with the fact that it cross-cuts normal faults in the Ibex Hills, of the Eastern Boundary Fault suggest syn to post-extensional oblique fault movement which supports the potential for transcurrent deformation in the study area (Plate 1). It also would seem that the timing of this recent folding in the Ibex Hills would be constrained to after the low-angle faulting, but before the most recent, high-angle normal faulting, given the latter appear consistent in their orientation (e.g. Figure 2.5). Recent, as young as Quaternary, syn to post-extensional, folding in the southern Death Valley region has been recognized in the Tecopa Basin to the east (Miller et al., 2005) and strikingly similar geometries of folded low-angle normal faults have been mapped in the Amargosa Chaos area to

the northwest (Castonguay, 2013). However, in both cases the fold axes are trending to the northwest, nearly 90° to the synform of the Ibex Hills. The variance in the geometry of young fold axes in the southern Death Valley region may be explained by differences in syn-extensional rotation of the region, however, this rotation is unconstrained in many places (e.g. Serpa and Pavlis, 1996; Guest et al., 2003).

2.6.4 Correlations within the Ibex Pass Basin

The volcanic and intrusive package mapped at the southern extent of the Ibex Hills (Plate 1) contains a tuff unit which is tentatively correlated to that which was mapped by Canalda (2009). This suggests the volcanic package of the southern Ibex Hills is largely younger than those in Ibex Pass, to the east. Currently the age of these Ibex Pass volcanics are of unknown age, however, previous work has suggested the package correlates to those in Wingate Wash which range in age from ~12.5-14 Ma (Luckow et al., 2005; Canalda, 2009). K-Ar dating of the volcanics in Ibex Pass (Figure 1) gave an age of ~12 Ma (Calzia, unpublished). In addition, the granitic mega-breccia overlies the volcanic deposits in Ibex Pass, and presumably are also younger than those in the southern Ibex Hills. Topping (1993) presented age constraints which suggested the deposition of granitic mega-breccias sourced from Kingston Peak took place until ~7.8 Ma, based on an interbedded tuff unit. Taken together the data suggests that the majority of the volcanic deposits of the southern Ibex Hills were deposited between ~12-7.8 Ma.

2.7 CONCLUSIONS.

The Ibex Hills and Saratoga Hills expose complexly deformed rocks ranging from 1.7 Ga basement rock to the Cambrian aged Zabriski Quartzite (Plate 1). Exposed in the southern Ibex Hills, is an angular unconformity between the Tertiary volcanics of Ibex Pass with the bedrock in the southern Ibex Hills (Plate 1). Six distinct Tertiary units were mapped in the area, including a white tuff layer which appeared to underlie the majority of the other deposits and correlated with a tuff previously mapped by Canalda (2009) further east in Ibex Pass (Figure 2.1).

The most recent pre- Quaternary units in the Ibex Pass area are gravels and megabreccias which contain clasts of granite interpreted to be sourced from the Kingston Range to the east. Overlying

the granite bearing units is another megabreccia consisting of clasts of the Beck Spring Dolomite. This same megabreccia unit is also seen in the northern Ibex Hills (Plate 1).

The northern Ibex Hills is a structurally complex sequence of low-angle normal faults placing units as young as the Johnnie Formation against Precambrian basement rock (Plate 1 and Figure 2.4). These low-angle normal faults appear to be folded about a northeast-southwest axis, consistent with the broader map pattern of the area. This geometry, along with folded cleavage planes, support a folding event younger than the low-angle normal faulting of the Ibex Hills. The low-angle normal faults are cut by high-angle normal faults which exhibit down to the northwest motion in their hanging walls (Figure 2.4 and 2.7). In addition to the northwest directed extension recorded in the study area, there is compelling evidence for southwest directed extension in the northern Ibex Hills (Plate 1; Figure 2.12).

The complexity of the northern Ibex Hills is not seen farther south in the study area where the structure is dominated by steeply dipping normal and oblique faulting (Plate 1). Northwest directed extension structures typical of the southern Death Valley region are well exposed in the boundary between the Saratoga Hills and the southern Ibex Hills (Plate 1 and Figure 2.9). Younger, generally right-lateral to oblique faults strike to the northwest and are interpreted to cross-cut some of the normal faults in this area (Figure 2.9). These high-angle oblique to strike-slip faults are most obvious in the Saratoga Hills where they are clearly exposed and are the dominant structure, especially in the central and southern portions of the range (Figure 2.9).



Figure 2.1. Location map showing the Ibex Hills (IH), Saratoga Hills (SH), Saddle Peak Hills (SPH), Black Mtn Detachment Fault (BMD), and Sheephead Fault (SF)

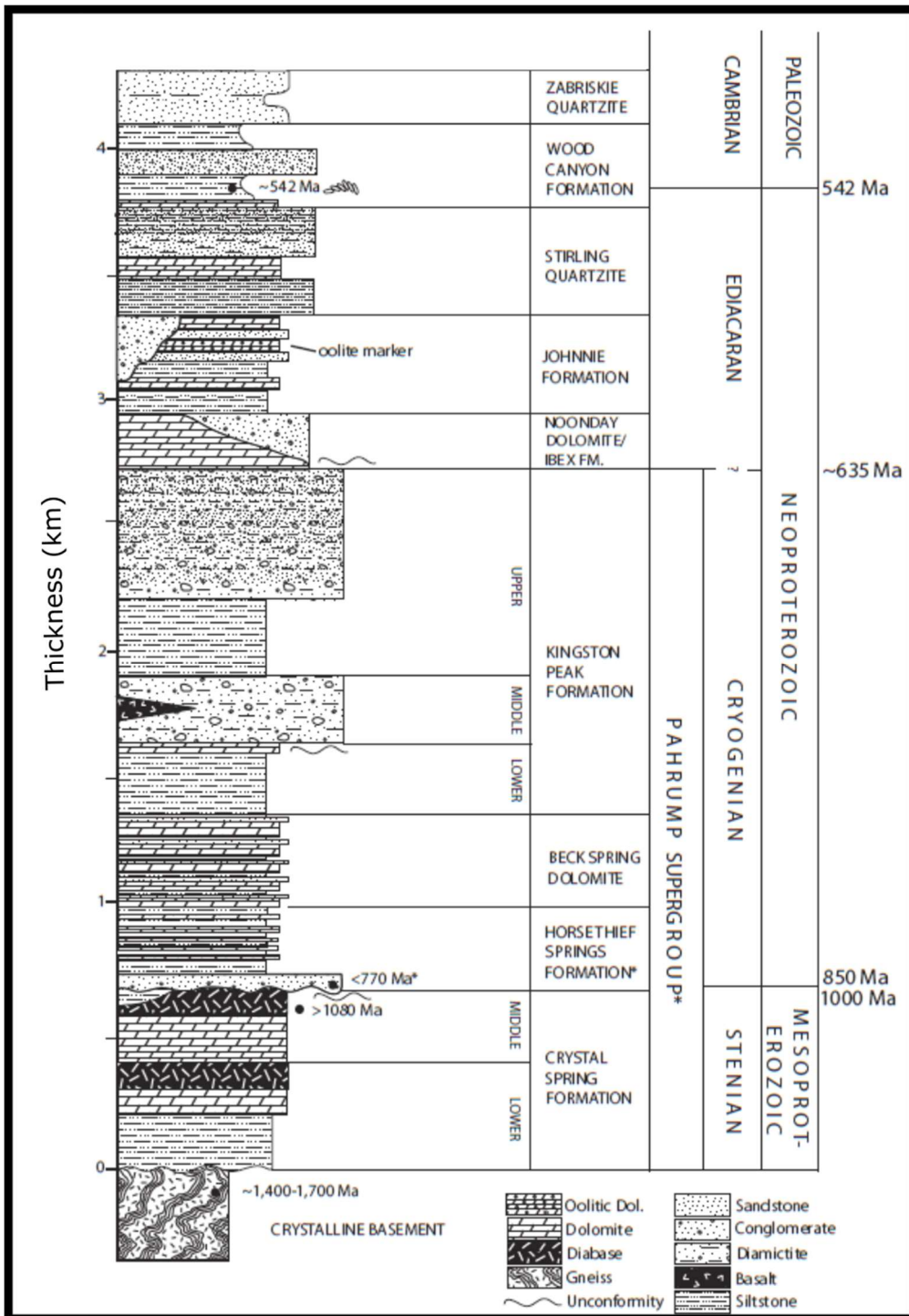


Figure 2.2. Generalized stratigraphy of the southern Death Valley area. Modified from Mohn and Link (2011)

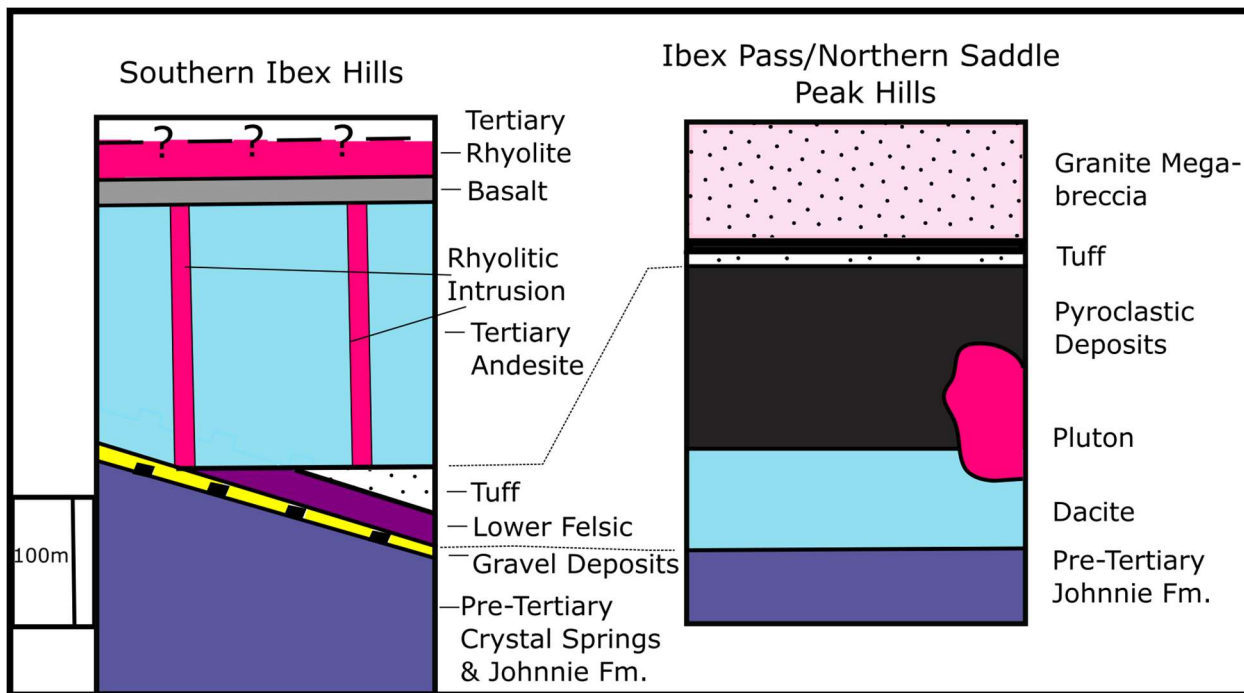


Figure 2.3. Comparison of the volcanic and igneous deposits of the southern Ibex Hills (this study) and those of Ibex Pass (Canalda, 2009).

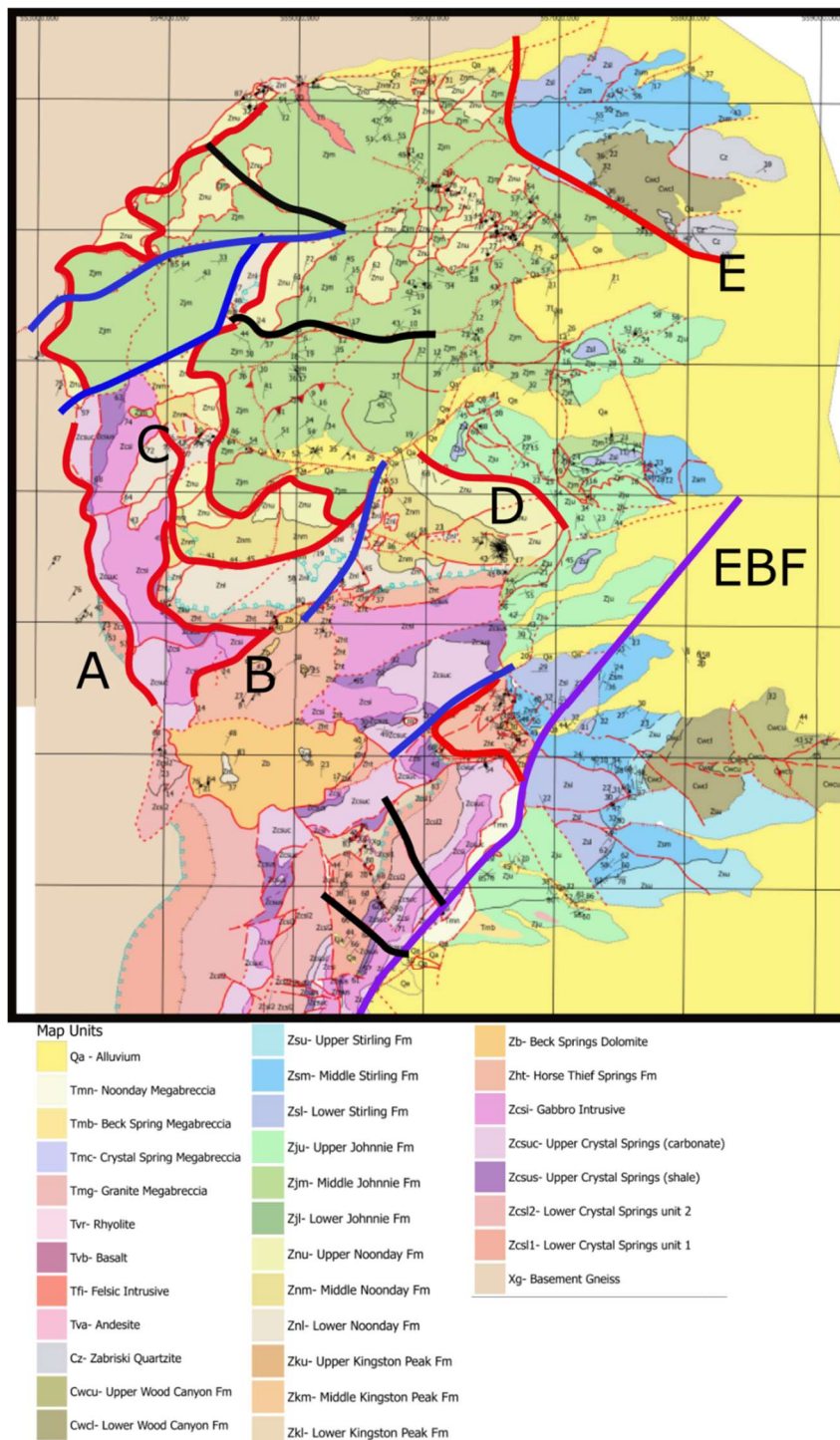


Figure 2.4. Geologic Map of the northern Ibex Hills. Highlighted are select faults of the area to show key cross-cutting relationships. Red-low-angle faults, Blue- northeast striking normal faults, Black-northwest striking faults, Purple-Eastern Boundary Fault. Letters indicate the fault names used in the text. EBF- Eastern Boundary Fault

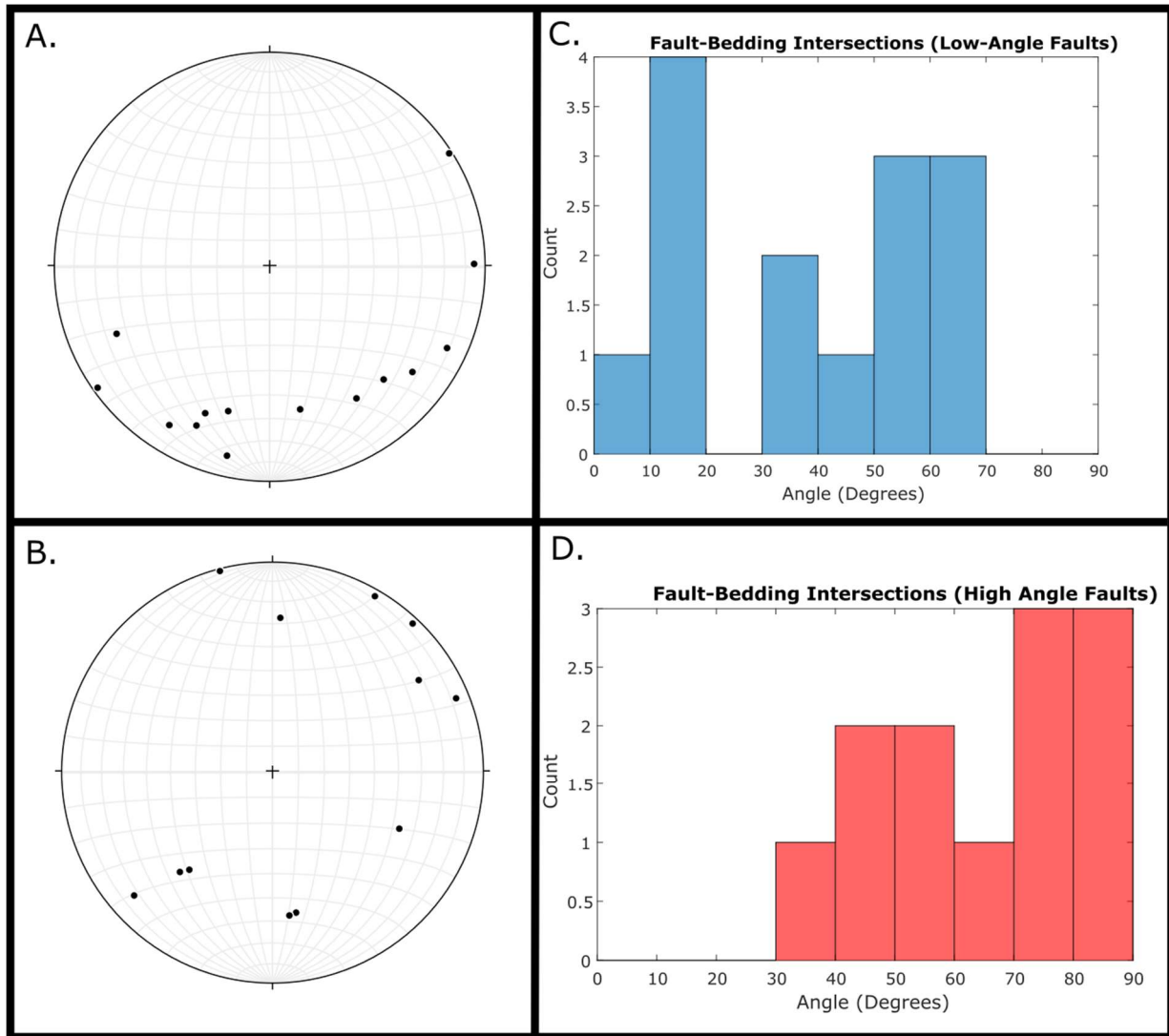


Figure 2.5. A. Lines of fault-bedding intersections of the low-angle normal faults in the Ibex Hills. C. Histogram of the angle of fault-bedding intersections of the low-angle normal faults in the Ibex Hills. B. Lines of fault-bedding intersections of the high-angle normal faults in the Ibex Hills. D. Histogram of the angle of fault-bedding intersections of the high-angle normal faults in the Ibex Hills.

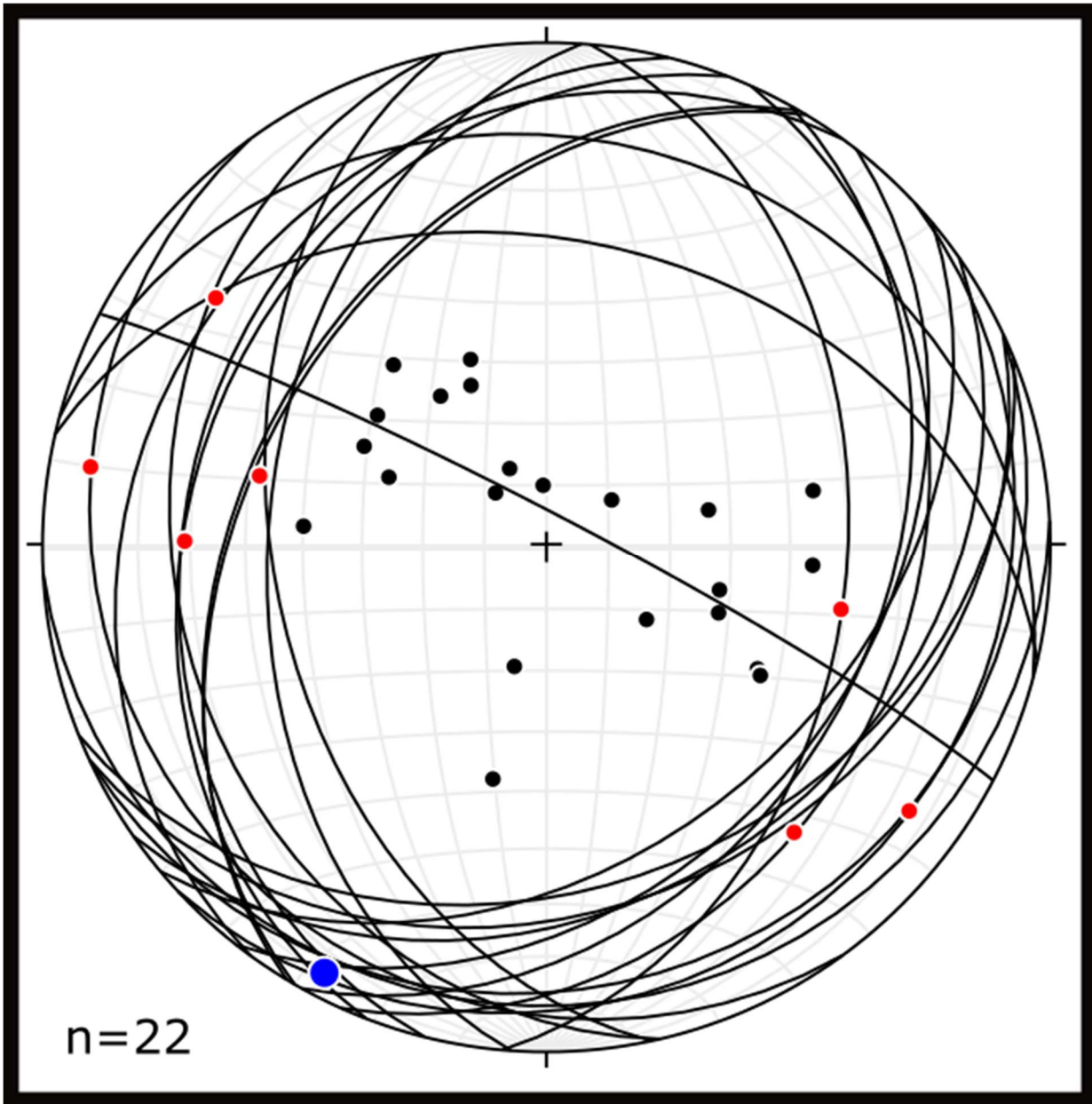


Figure 2.6. Stereonet of the low angle normal faults in the northern Ibex Hills. Red poles are slickenlines and black are the poles to the fault planes. Blue indicates the “fold” axis of the faults.

Figure 2.7. See associated .pdf. Cross-sections created for the study area. The right is a perspective DEM view of the area which has the placement of the cross-sections. IH- Ibex Hills, SH-Saratoga Hills. Abbreviations on sections follow those of the geologic map (Plate 1).

N = 47

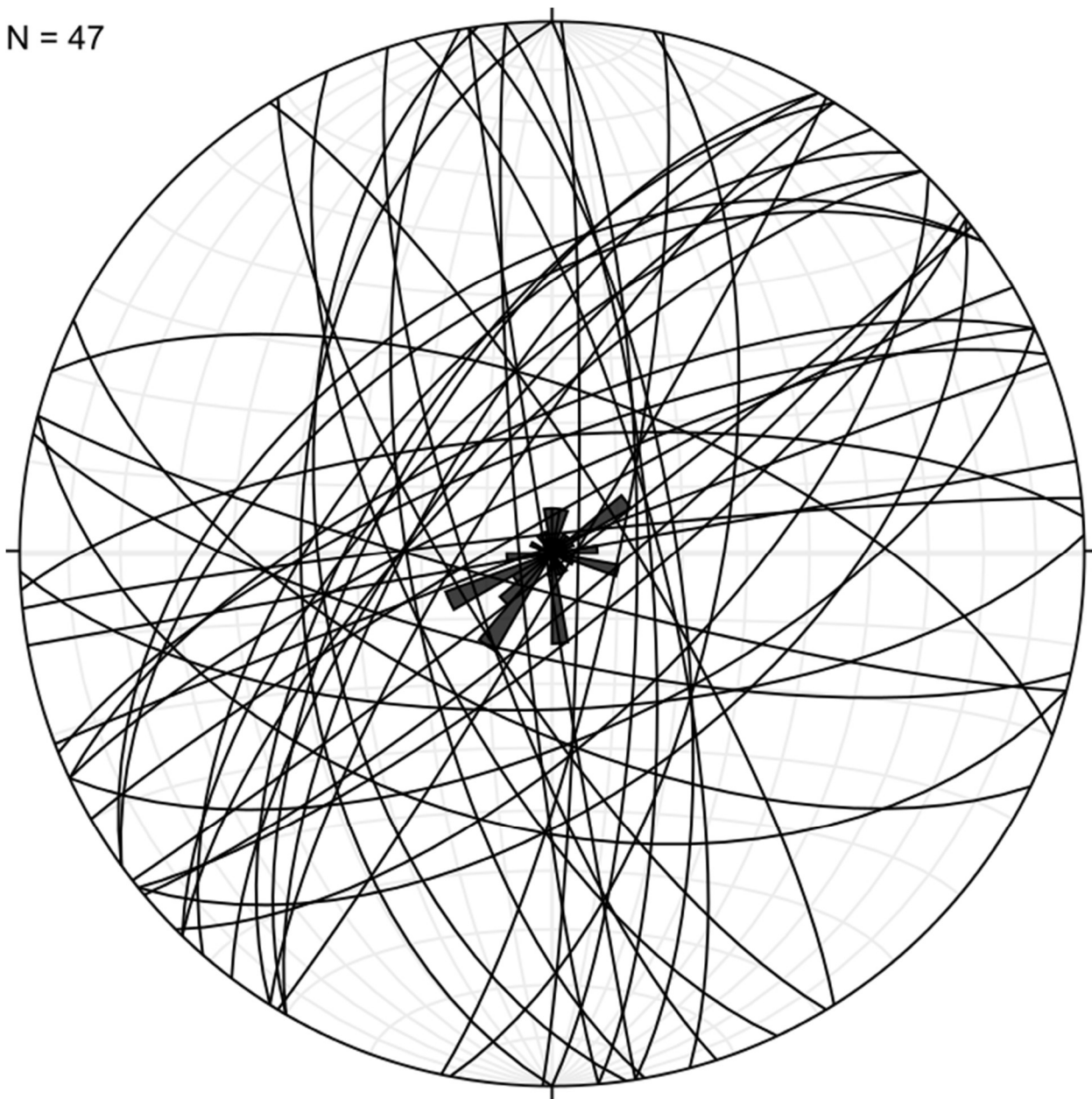


Figure 2.8. Stereonet of the moderate and high angle fault planes in the Ibex Hills. Rose diagram illustrates the dominate strikes seen in the field area.

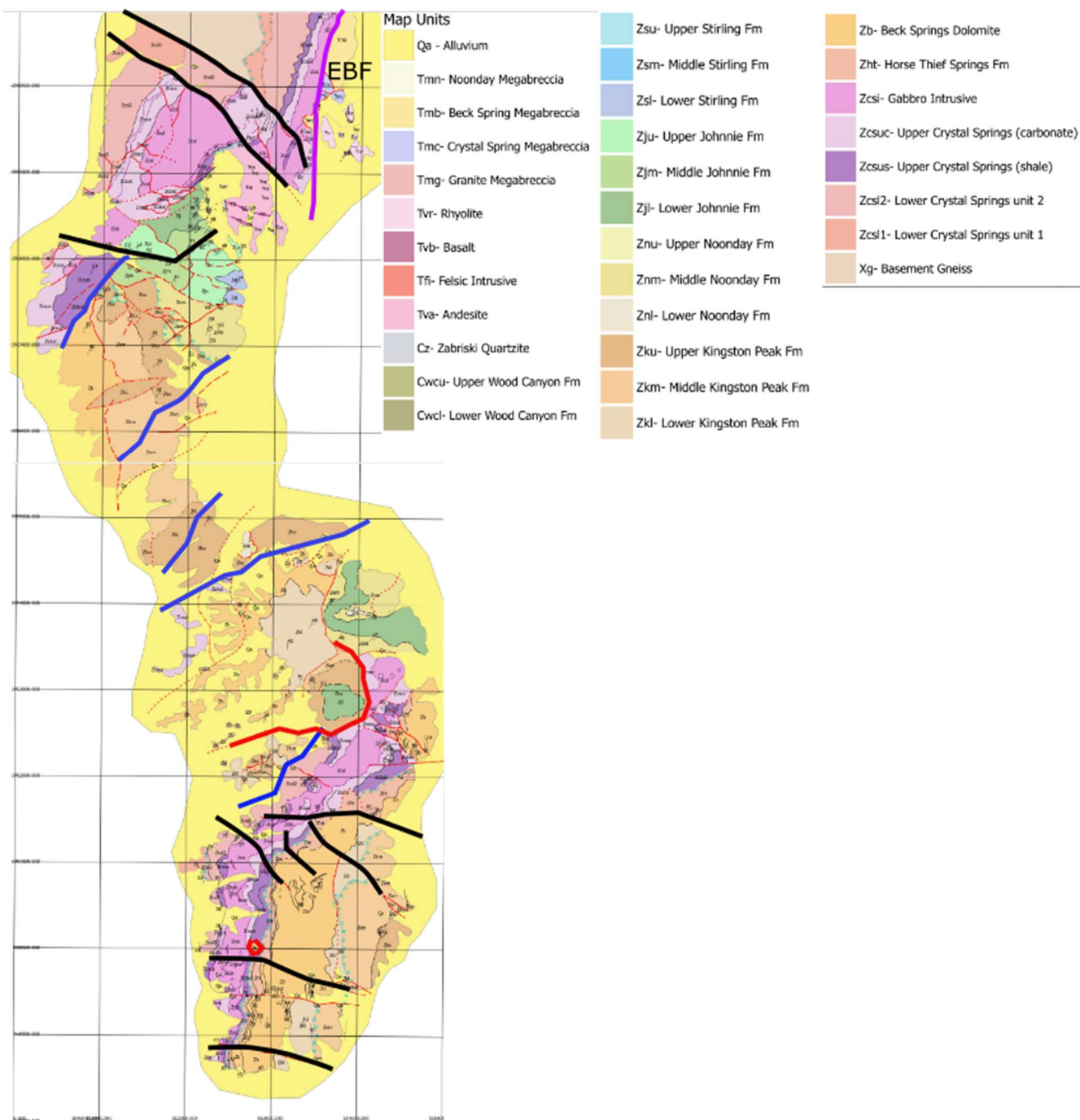


Figure 2.9. Geologic map of the southern Ibex Hills and Saratoga Hills with simplified fault traces of select faults. Black-northwest striking faults, Blue-northeast striking normal faults, Red- Low angle normal faults. EBF-Eastern Boundary Fault.



Figure 2.10. Field photograph showing the tight to isoclinal folds in the Radcliffe Member of the Noonday.

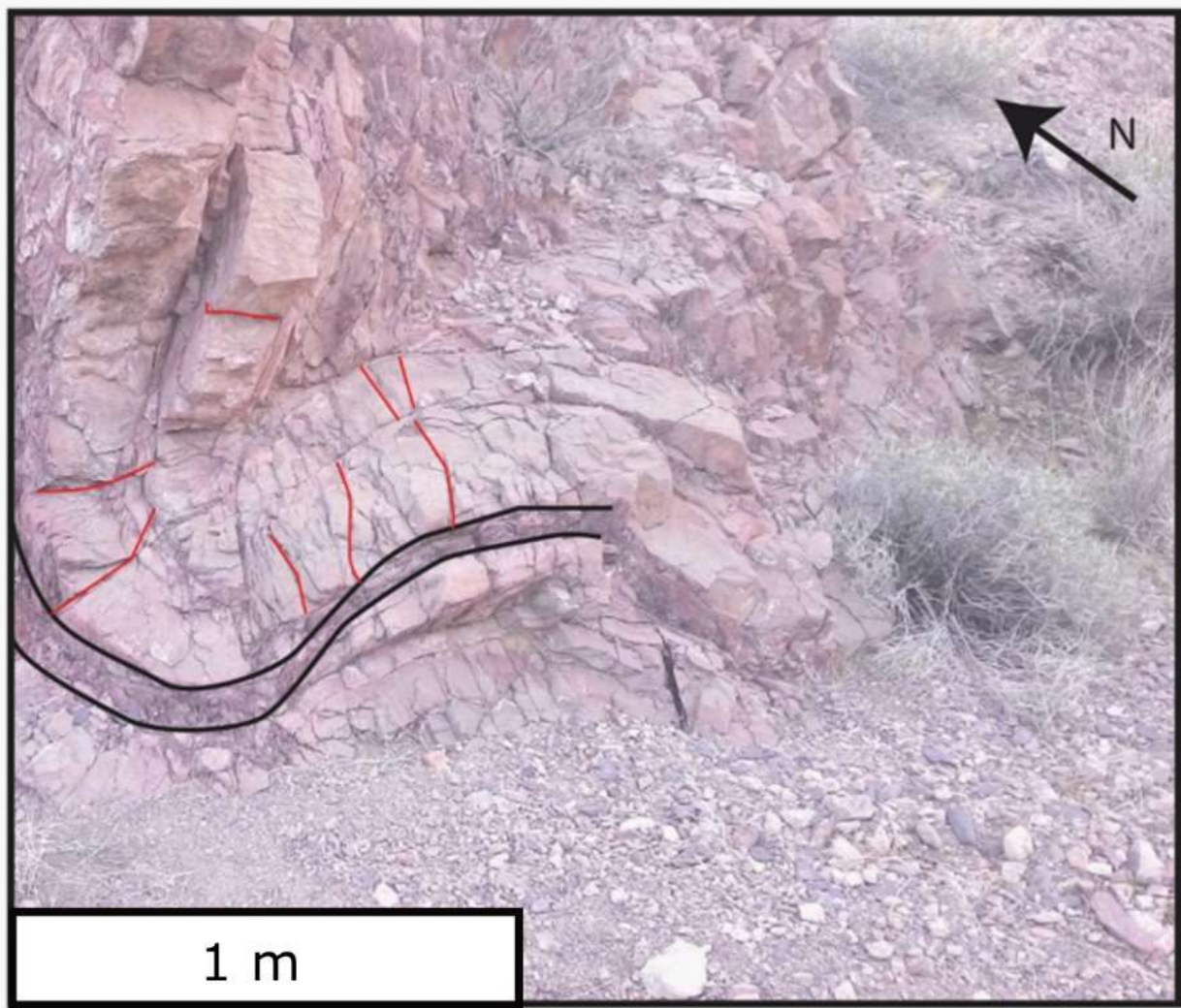


Figure 2.11. Field photograph annotated to show the cleavage (in red) present in the Radcliffe folds.

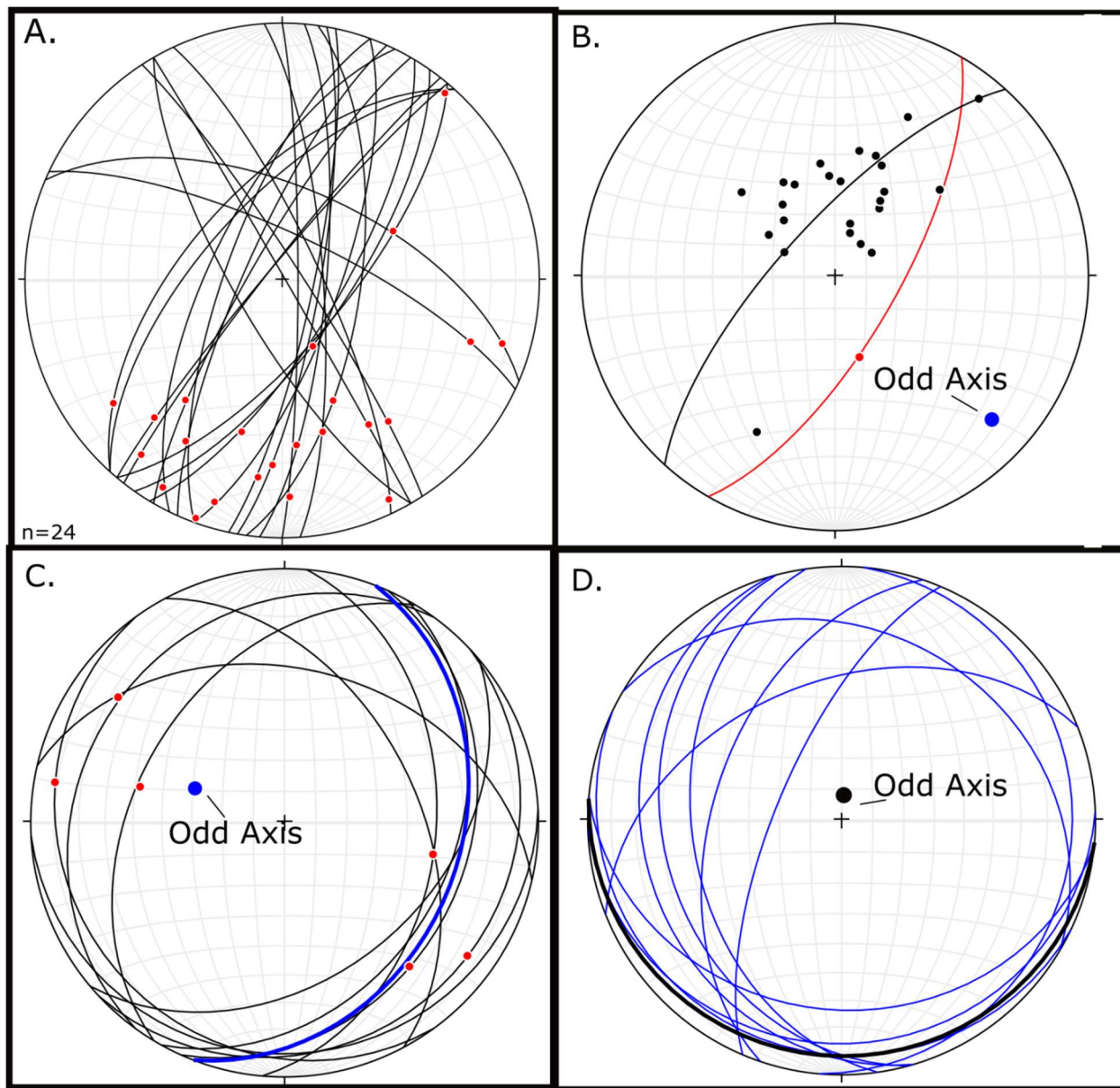


Figure 2.12. A. Stereonet of fault planes and slickenlines along the Eastern Boundary Fault. B. Plot of the B-Axes and their best fit plane, the pole to which is the “Odd-Axis”. Red plane indicates the map trace of the EBF with the rake of the slip vector also plotted. C. Low angle faults and slickenlines (red) of Fault B. Blue pole indicates the “Odd-Axis” determined via the methods discussed in the text and Krantz (1988) and its corresponding plane (also blue) is the best fit to the B-Axes. D. Rotated orientations of Fault B to correct for range tilt along

Figure 2.13. See associated pdf. A. Cross-section D-D' in the Saratoga Hills showing the current geometry of the range. B. After the fault movement has been restored across the range.

Figure 2.14. See associated .pdf. A. Cross-section of the current geometry along section B-B'. B. Section B-B' after restoration along the high-angle normal faults. C. Section B-B' after a 30° rotation about a horizontal axis to restore range tilt. Also note the projected geology in the hangingwall in order to restore the low-angle fault movement. D. After the restoration of Fault D. E. After the restoration of Fault E.

Figure 2.15. See associated .pdf. A. Cross-section of the current geometry along section trace A-A'. B. Cross-section of A-A' after the restoration of movement along high-angle normal faults C. Section A-A' after rotation of 30° about a horizontal axis to correct range tilt. Also note the lack of the structurally higher faults D and E and the projection of footwall rocks in order to restore the interpreted SW extension. D. After the restoration of Fault B. E. After the restoration of Fault A.

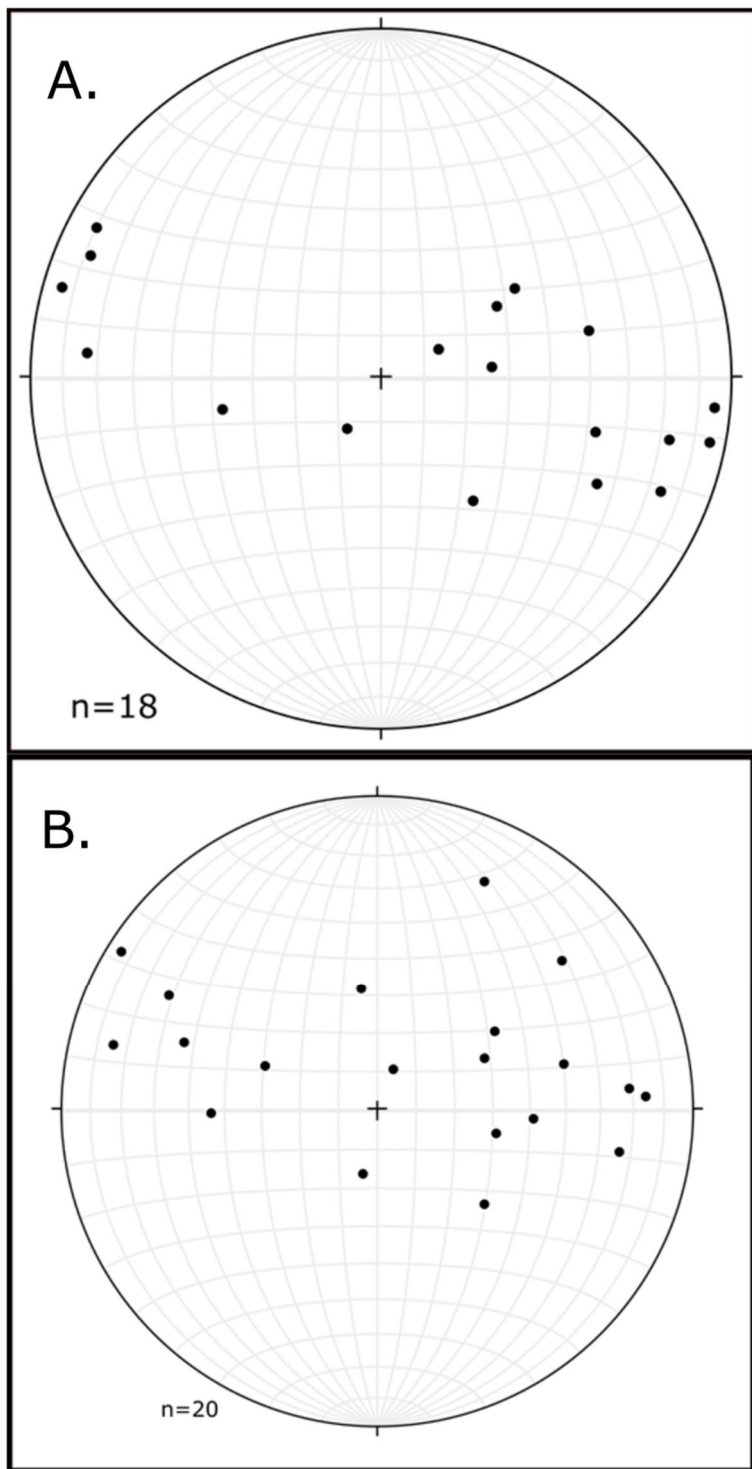


Figure 2.16. A. Fold axis determined from the SfM point cloud and field data from the Radcliffe outcrop in the Ibex Hills. B. Foliation-Bedding intersections from the same outcrop. Note the similarity in spread between the two plots.

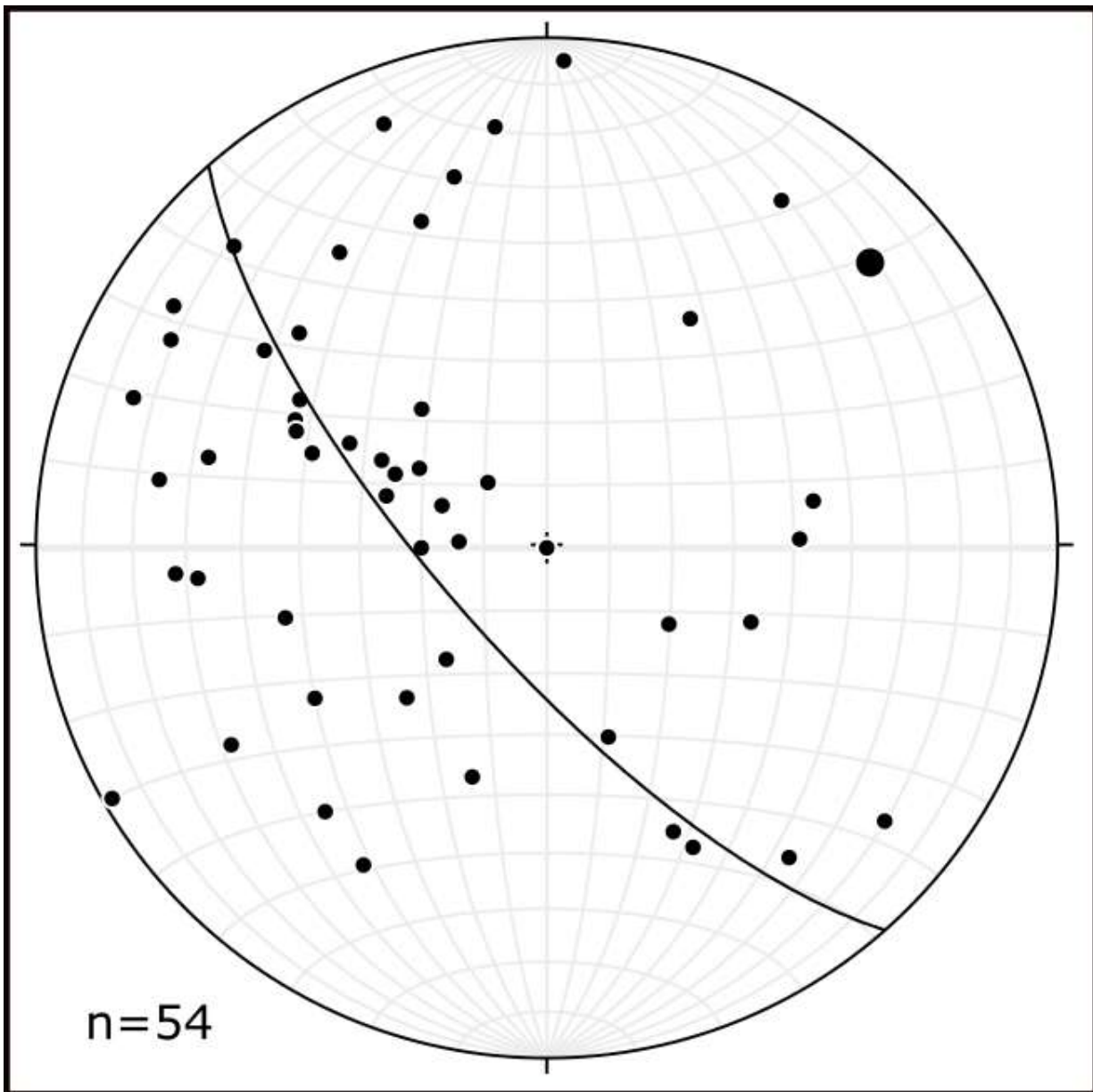


Figure 2.17. Stereonet of poles to foliation measured in the Radcliffe Member in the Ibex Hills. Great circle is the best fit to the data and the large pole indicates the interpreted fold-axis of F2.

Figure 2.18. See associated 3D .pdf. Structural model created in Move by Midland Valley for the folded outcrop in the Ibex Hills, as discussed in the text.

Table 2.1. Summary of the total stretch (Lf/Lo) and Heave recorded in the three restored sections presented in this study.

Section	A-A'	B-B'	D-D'
Stretch	1.52	2.36	1.2
Heave	2.4 km	5.1 km	1.7 km

Plate 1. Geologic Map of the study area. See attached .pdf.

References

- Bruhn, R.L., Pavlis, T.L., Plafker, G., and Serpa, L., 2004, Deformation during terrane accretion in the Saint Elias Orogen, Alaska: *Geological Society of America Bulletin*, v. 116, p. 771–787, doi: <http://0-dx.doi.org.lib.utep.edu/10.1130/B25182.1>.
- Burchfiel, B.C., Walker, D., Davis, G.A., Wernicke, B., and Anonymous, 1983, Kingston Range and related detachment faults; a major “breakway” zone in the southern Great Basin: *Abstracts with Programs - Geological Society of America*, v. 15, p. 536.
- Calzia, J., 1990, Geological studies in the Kingston Range, southern Death Valley [Ph.D. Dissertation]: University of California Davis.
- Calzia, J.P., and Ramo, O.T., 2000, Late Cenozoic crustal extension and magmatism, southern Death Valley region, California (D. R. Lageson, Ed.): *GSA Field Guide*, v. 2, p. 135–164.
- Calzia, J.P., and Rämö, O.T., 2005, Miocene rapakivi granites in the southern Death Valley region, California, USA: *Earth-Science Reviews*, v. 73, p. 221–243, doi: [10.1016/j.earscirev.2005.07.006](http://dx.doi.org/10.1016/j.earscirev.2005.07.006).
- Canalda, S.M., 2009, Magnitude of right-lateral offset on the southern Death Valley fault zone from Miocene volcanic assemblages [M.S.]: The University of Texas at El Paso, 155 p., <http://0-search.proquest.com.lib.utep.edu/pqdtglobal/docview/305068006/abstract/FFFE661790334E34PQ/2?accountid=7121> (accessed February 2015).
- Carvell, J., Blenkinsop, T., Clarke, G., and Tonelli, M., 2014, Scaling, kinematics and evolution of a polymodal fault system: Hail Creek Mine, NE Australia: *Tectonophysics*, v. 632, p. 138–150, doi: [10.1016/j.tecto.2014.06.003](http://dx.doi.org/10.1016/j.tecto.2014.06.003).
- Castonguay, S.R., 2013, Structural evolution of the virgin spring phase of the amargosa chaos, Death Valley, California, USA: Ph.D. Thesis, <http://adsabs.harvard.edu/abs/2013PhDT.....212C> (accessed October 2016).
- Corsetti, F.A., and Kaufman, A.J., 2005, The relationship between the Neoproterozoic Noonday Dolomite and the Ibex Formation; new observations and their bearing on “snowball Earth” (J. P. Calzia,

Ed.): Earth-Science Reviews, v. 73, p. 63–78, doi: <http://0-dx.doi.org.lib.utep.edu/10.1016/j.earscirev.2005.07.002>.

Davis, G.A., Fowler, T.K., Bishop, K.M., Brudos, T.C., Friedmann, S.J., Burbank, D.W., Parke, M.A., and Burchfiel, B.C., 1993, Pluton pinning of an active Miocene detachment fault system, eastern Mojave Desert, California: *Geology*, v. 21, p. 627–630, doi: 10.1130/0091-7613(1993)021<0627:PPOAAM>2.3.CO;2.

DeCelles, P.G., 2004, Late Jurassic to Eocene evolution of the Cordilleran thrust belt and foreland basin system, western U.S.A.: *American Journal of Science*, v. 304, p. 105–168, doi: 10.2475/ajs.304.2.105.

Ernst, W.G. (Ed.), 2009, Rise and fall of the Nevadaplano; Part I: *International Geology Review*, v. 51, p. 583–775.

Esparza, O., 2012, Structural analysis of the central Ibex Hills, Death Valley, California [M.S.]: The University of Texas at El Paso, 76 p., <http://0-search.proquest.com.lib.utep.edu/pqdtglobal/docview/1294191201/abstract/DD795681463A4DCCPQ/1?accountid=7121> (accessed February 2015).

Fleck, R.J., 1970, Tectonic Style, Magnitude, and Age of Deformation in the Sevier Orogenic Belt in Southern Nevada and Eastern California: *Geological Society of America Bulletin*, v. 81, p. 1705–1720, doi: 10.1130/0016-7606(1970)81[1705:TSMAAO]2.0.CO;2.

Fowler, T.K., and Calzia, J.P., 1999, Kingston Range detachment fault, southeastern Death Valley region, California; relation to Tertiary deposits and reconstruction of initial dip (L. A. Wright, Ed.): *Special Paper - Geological Society of America*, v. 333, p. 245–257.

Guest, B., Pavlis, T.L., Golding, H., and Serpa, L., 2003, Chasing the Garlock: A study of tectonic response to vertical axis rotation: *Geology*, v. 31, p. 553–556, doi: 10.1130/0091-7613(2003)031<0553:CTGASO>2.0.CO;2.

Heaman, L.M., and Grotzinger, J.P., 1992, 1.08 Ga diabase sills in the Pahrump Group, California: Implications for development of the Cordilleran miogeocline: *Geology*, v. 20, p. 637–640, doi: 10.1130/0091-7613(1992)020<0637:GDSITP>2.3.CO;2.

Holm, D.K., Pavlis, T.L., and Topping, D.J., 1994, Black Mountains crustal section, Death Valley region, California (S. F. McGill, Ed.): Geological Society of America, Cordilleran Section, Annual Meeting, Guidebook., v. 27, p. 31–54.

Holm, D.K., Snow, J.K., and Lux, D.R., 1992, Thermal and barometric constraints on the intrusive and unroofing history of the Black Mountains: Implications for timing, initial dip, and kinematics of detachment faulting in the Death Valley Region, California: *Tectonics*, v. 11, p. 507–522, doi: 10.1029/92TC00211.

Holm, D.K., and Wernicke, B., 1990, Black Mountains crustal section, Death Valley extended terrain, California: *Geology*, v. 18, p. 520–523, doi: 10.1130/0091-7613(1990)018<0520:BMCSDV>2.3.CO;2.

Krantz, R.W., 1988, Multiple fault sets and three-dimensional strain; theory and application: *Journal of Structural Geology*, v. 10, p. 225–237.

Krantz, R.W., 1989, Orthorhombic fault patterns; the odd axis model and slip vector orientations: *Tectonics*, v. 8, p. 483–495, doi: <http://0-dx.doi.org.lib.utep.edu/10.1029/TC008i003p00483>.

Macdonald, Prave, A.R., Petterson, R., Smith, E.F., Pruss, S.B., Oates, K., Waechter, F., Trotsuk, D., and Fallick, A.E., 2013, The Laurentian record of Neoproterozoic glaciation, tectonism, and eukaryotic evolution in Death Valley, California: *Geological Society of America Bulletin*, v. 125, p. 1203–1223.

Mahon, R.C., and Link, P.K., 2013, EdMap geologic map of the Saddle Peak Hills 7.5' quadrangle, Death Valley National Park, San Bernardino County, California: Abstracts with Programs - Geological Society of America, v. 45, p. 372.

Mancktelow, N.S., and Pavlis, T.L., 1994, Fold-fault relationships in low-angle detachment systems: *Tectonics*, v. 13, p. 668–685, doi: 10.1029/93TC03489.

Marrett, R., and Allmendinger, R.W., 1990, Kinematic analysis of fault-slip data: *Journal of Structural Geology*, v. 12, p. 973–986, doi: 10.1016/0191-8141(90)90093-E.

McMackin, M.R., 1992, Tectonic evolution of the Kingston Range, Death Valley, California [Doctoral]: Pennsylvania State University at University Park, University Park, PA, United States (USA),

[search.proquest.com.lib.utep.edu/georef/docview/50366954/citation/42CA980148AE48F3PQ/10](http://0-search.proquest.com.lib.utep.edu/georef/docview/50366954/citation/42CA980148AE48F3PQ/10)
(accessed March 2016).

Miller, M.G., 2003, Basement-involved thrust faulting in a thin-skinned fold-and-thrust belt, Death Valley, California, USA: *Geology*, v. 31, p. 31–34, doi: 10.1130/0091-7613(2003)031<0031:BITFIA>2.0.CO;2.

Miller, D.M., Menges, C.M., and McMackin, M.R., 2005, Geomorphology and tectonics at the intersection of Silurian and Death Valleys; 2005 guidebook, Pacific Cell, Friends of the Pleistocene: Friends of the Pleistocene, Pacific Cell, <http://0.search.proquest.com/georef/docview/916837582/AC014133B3594E5CPQ/1> (accessed August 2018).

Miller, M.B., and Pavlis, T.L., 2005, The Black Mountains turtlebacks: Rosetta stones of Death Valley tectonics: *Earth-Science Reviews*, v. 73, p. 115–138, doi: 10.1016/j.earscirev.2005.04.007.

Miller, M.G., and Prave, A.R., 2002, Rolling hinge or fixed basin?: A test of continental extensional models in Death Valley, California, United States: *Geology*, v. 30, p. 847–850, doi: 10.1130/0091-7613(2002)030<0847:RHOFA>2.0.CO;2.

Norton, I., 2011, Two-stage formation of Death Valley: *Geosphere*, v. 7, p. 171–182, doi: 10.1130/GES00588.1.

Otten, J., 1976, Geologic Features of the Central Black Mountains, California:

Pavlis, T.L., Langford, R., Hurtado, J., and Serpa, L., 2010, Computer-based data acquisition and visualization systems in field geology: Results from 12 years of experimentation and future potential: *Geosphere*, v. 6, p. 275–294, doi: 10.1130/GES00503.1.

Pavlis, T.L., Rutkofske, J., Guerrero, F., and Serpa, L.F., 2014, Structural overprinting of Mesozoic thrust systems in eastern California and its importance to reconstruction of Neogene extension in the southern Basin and Range: *Geosphere*, v. 10, p. 732–756, doi: 10.1130/GES00993.1.

Prave, A.R., and McMackin, M.R., 1999, Depositional framework of mid- to late Miocene strata, Dumont Hills and southern margin Kingston Range; implications for the tectonostratigraphic evolution

of the southern Death Valley region (L. A. Wright, Ed.): Special Paper - Geological Society of America, v. 333, p. 259–275.

Renik, B., and Christie-Blick, N., 2013, A new hypothesis for the amount and distribution of dextral displacement along the Fish Lake Valley–northern Death Valley–Furnace Creek fault zone, California-Nevada: *Tectonics*, v. 32, p. 123–145, doi: 10.1029/2012TC003170.

Scott, R.K., Wright, L.A., and Drake, R.E., 1988, Thrust fault-related monolithologic breccias and cyclic playa-lake deposits in the Miocene China Ranch Basin, Death Valley region, California: *Abstracts with Programs - Geological Society of America*, v. 20, p. 229.

Serpa, L., and Pavlis, T.L., 1996, Three-dimensional model of the late Cenozoic history of the Death Valley region, southeastern California: *Tectonics*, v. 15, p. 1113–1128, doi: 10.1029/96TC01633.

Serpa, L., Voogd, B.D., Wright, L., Willemin, J., Oliver, J., Hauser, E., and Troxel, B., 1988, Structure of the central Death Valley pull-apart basin and vicinity from COCORP profiles in the southern Great Basin: *Geological Society of America Bulletin*, v. 100, p. 1437–1450, doi: 10.1130/0016-7606(1988)100<1437:SOTCDV>2.3.CO;2.

Snow, J.K., and Wernicke, B.P., 2000, Cenozoic tectonism in the central Basin and Range; magnitude, rate, and distribution of upper crustal strain: *American Journal of Science*, v. 300, p. 659–719, doi: 10.2475/ajs.300.9.659.

Stewart, J.H., 1972, Initial Deposits in the Cordilleran Geosyncline: Evidence of a Late Precambrian (<850 m.y.) Continental Separation: *Geological Society of America Bulletin*, v. 83, p. 1345–1360, doi: 10.1130/0016-7606(1972)83[1345:IDITCG]2.0.CO;2.

Topping, D.J., 1993, Paleogeographic reconstruction of the Death Valley extended region: Evidence from Miocene large rock-avalanche deposits in the Amargosa Chaos Basin, California: *Geological Society of America Bulletin*, v. 105, p. 1190–1213, doi: 10.1130/0016-7606(1993)105<1190:PROTDV>2.3.CO;2.

Troxel, B.W., Calzia, J.P., Pavlis, T.L., and Anonymous, 1992, SW-directed extensional features and related magmatism, southern Death Valley region and the Kingston Range: *Abstracts with Programs - Geological Society of America*, v. 24, p. 87.

Walker, J.D., Burchfiel, B.C., and Davis, G.A., 1995, New age controls on initiation and timing of foreland belt thrusting in the Clark Mountains, southern California: *Geological Society of America Bulletin*, v. 107, p. 742–750, doi: 10.1130/0016-7606(1995)107<0742:NACIOA>2.3.CO;2.

Wernicke, B., 1981, Low-angle normal faults in the Basin and Range Province: nappe tectonics in an extending orogen: *Nature*, v. 291, p. 645–648, doi: 10.1038/291645a0.

Wernicke, B., Axen, G.J., and Snow, J.K., 1988, Basin and Range extensional tectonics at the latitude of Las Vegas, Nevada: *Geological Society of America Bulletin*, v. 100, p. 1738–1757, doi: 10.1130/0016-7606(1988)100<1738:BARETA>2.3.CO;2.

Westoby, M.J., Brasington, J., Glasser, N.F., Hambrey, M.J., and Reynolds, J.M., 2012, ‘Structure-from-Motion’ photogrammetry: A low-cost, effective tool for geoscience applications: *Geomorphology*, v. 179, p. 300–314, doi: 10.1016/j.geomorph.2012.08.021.

Wright, L.A., 1954, Geology of the Alexander Hills area, Inyo and San Bernardino counties, Map Sheet no. 17 of Jahns, R. H., ed., *Geology of southern California: Geology of the Alexander Hills area, Inyo and San Bernardino counties, Map Sheet no. 17 of Jahns, R. H., ed., Geology of southern California*, <http://0.search.proquest.com/georef/docview/53068351/A2875BFE68CE436DPQ/1> (accessed August 2018).

Wright, L., 1974, Geology of the southeast quarter of the Tecopa quadrangle, San Bernardino and Inyo Counties, California:

Wright, L., and Troxel, B., 1984, Geology of the northern half of the confidence hills 15-minute quadrangle, death valley region, eastern california; the area of the amargosa chaos: *California Division of Mines and Geology*.

Wright, L.A., and Troxel, B.W., 1973, Shallow-Fault Interpretation of Basin and Range Structure, Southwestern Great Basin: John Wiley & Sons, New York, <http://0-search.proquest.com.lib.utep.edu/georef/docview/52433136/2630E80EC9F84A79PQ/4> (accessed January 2017).

Wright, L.A., Troxel, B.W., Williams, E.G., Roberts, M.T., and Diehl, P.E., 1974, Precambrian sedimentary environments of the Death Valley region, eastern California: *Death Valley Publ. Co.*;

Shoshone; CA, <http://0-search.proquest.com.lib.utep.edu/georef/docview/52351472/2DAD0567B15240FFPQ/2?accountid=7121> (accessed February 2015).

Regional Correlations of the Ibex Hills in the Southern Death Valley Region, CA

3.1 ABSTRACT

The Ibex Hills occupies an important position in the context of southern Death Valley tectonics as it is often incorporated as an up-dip portion of the Black Mountain Detachment Fault, a critical interpretation for the structural evolution of the region. In addition, it is proximal to both the Sheephead Fault Zone and the Grand View Fault, structures which have been incorporated into regional constructions in the past. Despite these factors the Ibex Hills have not been thoroughly considered for previous reconstructions of the southern Death Valley region. In this chapter the Ibex Hills are correlated across the region using a 3D structural model created in Move by Midland Valley. Geologic mapping done in the Ibex Hills revealed a previously unmapped granitic mega-breccia which provides a minimum amount of displacement to within 10 km of the Kingston Range. Further piercing lines were provided by an intrusive unit in the northern Ibex Hills as well as the unconformity which underlies the lower Noonday Dolomite. The results of the reconstruction imply a significant amount, >25 km, of strike-slip movement along a combination of the Sheephead Fault Zone and the Grand View Fault. In addition, a component of clockwise rotation is needed to properly restore the granitic mega-breccia of the Ibex Hills. This model is also consistent with an early phase of southwest directed extension which is preserved in the Ibex Hills, followed by more recent, northwest directed extension.

3.2 INTRODUCTION

The Ibex Hills of southern Death Valley, CA are adjacent to the Black Mountains/Armargosa Detachment, the Sheephead Fault, and the Grand View Fault which have all been suggested to be key elements for regional reconstructions (Figure 3.1) (Holm and Wernicke, 1990; Snow and Wernicke, 2000; Renik and Christie-Blick, 2013). However, despite the ranges proximity to these vital piercing lines, the Ibex Hills and their place in the regional context have not been well analyzed (e.g. Topping, 1993). The work of this chapter attempts to fill this gap in knowledge by providing reconstructions of the Ibex Hills in the regional context of southern Death Valley, based on newly acquired data and interpretations, in part presented in the previous chapter, as well as a synthesis of previous work (e.g. Wright, 1974; Wright and Troxel, 1974; Topping, 1993; Canalda, 2009; Renik and Christie-Blick, 2013).

The competing hypotheses concerning the tectonic evolution of the southern Death Valley region can be grouped into two camps: 1) models that consider the extension in the region to have occurred primarily along a single detachment surface (i.e. the Black Mountain Detachment Fault), the “rolling-hinge model” (Holm and Wernicke, 1990; Topping, 1993; Snow, J. K. and Wernicke, B. P., 2000), and 2) models suggesting extension took place along multiple, discrete faults throughout the region (Wright et al., 1991; Serpa and Pavlis, 1996; Miller and Pavlis, 2005; Topping, 2018). The resulting reconstructions from the two models result in significant differences in the magnitude of crustal extension in the Death Valley region, ranging from as low as 30% (e.g. Wright and Troxel, 1973) to as high as 400% (e.g. Stewart, 1983; Snow, J. K. and Wernicke, B. P., 2000). An important factor in the different tectonic models for the region is the relative influence of strike-slip faults. Given that Death Valley has long been at the center of the discussion of continental extensional and transtensional tectonics, since the coining of the term “pull-apart basin” was suggested for the formation of the modern

valley itself (Burchfiel and Stewart, 1966), it is logical that insight into this region will broaden our knowledge of the subject as a whole.

The nature of the “rolling-hinge” model is such that it does not require significant movement along other faults beyond the primary detachment fault, and strike-slip systems are inferred to be largely passive, displacement transfer structures in the shallow crust (Holm and Wernicke, 1990; Snow and Wernicke, 2000). In contrast, other models of Death Valley extension suggest a history of pull-apart basin development, in essence, discrete sets of normal faults bounded by basin-flanking strike-slip faults which developed to accommodate the extension (e.g. Wright et al., 1991; Topping, 2018). Indeed, Serpa and Pavlis (1996) emphasized the role of distributed transtension across the region, implying strike-slip systems were the driver to the extension, rather than passive displacement transfer zones. The models relying on discrete faulting are further supported by seismic imaging in Death Valley which indicates an upper-crust dominated by discrete, brittle deformation without the presence of a regional detachment (Serpa et al., 1988).

Geologic mapping and cross-section interpretation of the Ibex Hills presented in the previous chapter is at odds with the “rolling-hinge model”, given the evidence found for multiple generations of extensional faulting with different extension directions. These geologic mapping products also allow for the correlation of a number of features in and around the Ibex Hills to those elsewhere in southern Death Valley, most notably a regional unconformity below the Noonday Formation (Wright et al., 1974) and a mono-lithic granitic mega-breccia mapped along the eastern flank of the Ibex Hills (Figure 3.2). Using these features as piercing lines a 3-dimensional reconstruction of the Ibex Hills was created using Move 2017 software by Midland Valley Ltd. (www.mve.com). In addition, key cross-cutting relationships mapped in the Ibex Hills, along with previous work in nearby areas (e.g. Mahon and Link, 2013; Bidgoli et al., 2015) provided temporal and/or kinematic context for the model. The results of this work offer further constraints upon the magnitude of strike-slip movement in southern Death Valley and also

provide a source for the southwest directed extensional faults mapped in the Ibex Hills which further complicates the hypothesis of a regional detachment.

3.3 PREVIOUS WORK

Reconstructions of the southern Death Valley region have been the subject of debate for decades and the Ibex Hills is in the midst of these reconstructions, south of the regional Sheephead Fault and Grand View Fault, and containing the previously interpreted trace of the Black Mountain Detachment (Figure 1) (Holm and Wernicke, 1990; Holm and Dokka, 1993; Topping, 1993; Renik, 2010). The nature of these structures is key to the “rolling-hinge” model (e.g. Snow and Wernicke, 2000) as well as to alternative hypotheses which highlight more discrete faulting (e.g. Miller and Pavlis, 2005). An understanding of previously proposed models is important in highlighting the significance of this work and an overview is provided below.

3.3.1 Rolling-Hinge Model

The explanation of a single detachment surface to accommodate high magnitudes of extension in Death Valley was initially proposed by Stewart (1983) to explain the absence of the stratigraphic section, seen in the Panamint Range, in the Black Mountains (Figure 3.1). Stewart (1983) suggested that the Panamint Range was originally atop the Black Mountains before being transported ~80 km along a detachment surface. It is also important to note, especially in the context of the Ibex Hills, that the detachment surface of Stewart (1983) would include the Amargosa Fault of Noble (1941) (previously described as the “Amargosa Thrust” before the acceptance of low-angle normal faults). This same Amargosa Fault, and its up-dip exposure mapped in the Ibex Hills, would be called upon in later extensional models as the primary detachment surface (e.g. Holm and Wernicke, 1990; Holm and Dokka, 1993; Topping, 1993).

Although there have long been proponents of large scale, low-angle detachment faulting within the Death Valley region (e.g. Stewart, 1983), the specific mechanics of the “rolling-hinge” model were

not well laid out at the time. Further interest in the concept of low-angle normal faults led to multiple models to explain them. Prominent among them is the concept of an isostatically rebounding footwall (Spencer, 1984) which was proposed to explain the low-angle, even reverse dip structures seen along the boundary of the Colorado Plateau and the Basin and Range Province (Wernicke and Axen, 1988) as well as across the Death Valley region (Hamilton, 1988). This model evolved into what came to be known as the “rolling-hinge” model. The concept of the “rolling-hinge” model consists of an initial breakaway fault which soles into a primary detachment surface (Buck et al., 1988; Wernicke and Axen, 1988). In these models, as movement continues along the breakaway fault, the resulting denudation causes isostatic rebound and folding of the lower crust in the footwall of the detachment, which ultimately decreases the dip of the breakaway fault until it can no longer support active movement (Figure 3.3). As extension continues along the detachment a new frontal fault forms ahead of the folded footwall rocks and the process continues (Figure 3.3). This propagation of the uplifted, folded footwall rocks is what gives the “rolling-hinge” model its namesake (Figure 3.3).

The application of the rolling-hinge model to Death Valley is central to many models which suggest a high magnitude of extension for the region (e.g. Snow and Wernicke, 2000), although it is not the only process put forth to accommodate such high rates of extension (e.g. Topping, 2018). The models are attractive for the Death Valley region because they can account for the well-documented east to west age progression of extensional structures first recognized by Wright et al. (1989).

Most of the high-magnitude extensional models hinge on the correlation of major thrust sheets and other pre-extensional markers within the central Basin and Range Province (Wernicke et al., 1988; Snow and Wernicke, 2000). Particularly central to these models is the interpretation that the same thrust can be correlating across the region including the Panamint thrust in the northern Panamint Range, the Chicago Pass Thrust of the Nopah and Resting Springs Ranges, and the Wheeler Pass thrust in the Spring Mountains (Figure 3.1). This interpretation allows restoration of the Panamint Range, Black

Mountains, Nopah Range, and Resting Springs Range to a small pre-extensional sliver (Wernicke et al., 1988; Snow and Wernicke, 2000). The implication of this restoration is one of significant regional extension, which is most commonly accommodated using a rolling-hinge detachment model (Wernicke et al., 1988; Holm and Wernicke, 1990; Holm and Dokka, 1993; Snow and Wernicke, 2000; Norton, 2011). While not all models required the entirety of the Panamint Range block to restore atop the Black Mountains the concept of a single, rolling-hinge detachment in Death Valley remains prominent in the literature (Wernicke et al., 1988; Holm and Wernicke, 1990; Holm and Dokka, 1993; Snow and Wernicke, 2000).

3.3.2 Discrete Fault Models

Other authors have suggested that extension in the Death Valley region has been accommodated by multiple sets of discrete faults including both normal faults and strike-slip systems (Wright and Troxel, 1973; Serpa and Pavlis, 1996; Miller and Prave, 2002; Miller and Pavlis, 2005; Renik and Christie-Blick, 2013). Early work by Wright and Troxel (1973) interpreted a combination of shallow crustal faults, which terminate around the contact with crystalline basement, and larger normal faults which penetrate basement and accommodate the majority of the regional offset (Figure 3). Based on their cross-section reconstructions Wright and Troxel (1973) estimated ~30-50% extension across the region, much lower than the later work involving the rolling-hinge model (Wernicke et al., 1988; Snow and Wernicke, 2000).

More recent work has utilized more detailed geologic mapping which typically contradicted the accuracy of piercing lines used by Snow and Wernicke (2000) and other related work (Luckow et al., 2005; Pavlis, T.L et al., 2012, 2014; Renik and Christie-Blick, 2013). Work in the southern Panamint Range and Owshead Mountains (Figure 1), for example, found a complex suite of early to middle Miocene, syn-extensional basins associated with sinistral and sinistral-normal sets of faults and relatively low extension magnitudes (Luckow et al., 2005; Pavlis, T.L et al., 2012). This mapping

contradicts one component of most large-scale detachment models of the region that restore this region to a thin sliver in map view (Wernicke et al., 1988; Holm and Wernicke, 1990; Snow and Wernicke, 2000). In contrast, other recent work suggests even more extreme extension across the Panamint Range with inference the range exhumes a window in a detachment system (Norton, 2011).

Other recent work has complicated the interpretation of the large magnitude of displacement of the Panamint Range, (Miller and Pavlis, 2005; Renik and Christie-Blick, 2013; Pavlis et al., 2014). Reanalysis of pre-extensional markers has led to reconstructions of Death Valley which require only modest extension (Figure 3.3) (Renik and Christie-Blick, 2013; Pavlis et al., 2014). In addition, Pavlis et al. (2014) recognized evidence for two shortening events in the Death Valley region which was previously not considered by earlier reconstructions (e.g. Snow and Wernicke, 2000), and concluded that all previous reconstructions were invalid in light of that observation.

3.4 GEOLOGIC SETTING

The reconstruction model presented in this chapter is based on regional correlations mapped in the Ibex Hills and adjacent Ibex Pass to other locales in southern Death Valley (Figure 3.1). To provide context for these correlations I review several important structures and stratigraphic relationships across the ranges that are key to the analysis here.

3.4.1 Sheephead Fault

The Sheephead Fault is an east-west to southeast striking feature in southern Death Valley, to the east of modern Death Valley (Figure 3.1). The fault is most clearly exposed along the southern flank of the Black Mountains at Sheephead Pass (Wright and Troxel, 1984; Renik, 2010). In single detachment models, the Sheephead fault has been interpreted as simply a continuation of the Black Mountain Detachment (Holm and Wernicke, 1990; Holm and Dokka, 1993; Snow and Wernicke, 2000) but has been interpreted very differently by others.

One critical issue with the Sheephead fault is the interpretation of the fault trace on either side of the exposures at Sheephead pass. To the west of Sheephead Pass, the fault becomes difficult to

distinguish from the other complex faults of the Amargosa Chaos. Specifically, from Sheephead Pass to Jubilee Pass, numerous low-angle structures clearly separate shattered cover from basement (Wright and Troxel, 1984) and the Sheephead fault either merges with these low-angle structures or is one of several discrete, higher angle faults within the basement. Farther west, from near Jubilee Pass westward, a moderately north-dipping fault separates Tertiary rocks of the Amargosa Chaos Basin from basement (Wright and Troxel, 1984) suggesting either a steep strike-slip fault rotated to lower angle or a moderate angle normal fault system (e.g. Topping, 1993). To the east of Sheephead Pass the fault has previously been mapped as continuing across basinal cover directly into the Alexander Hills (e.g. Wright, 1974) or in other interpretations the fault is shown as displaced by the dextral Grandview Fault (e.g. Topping, 1993).

Despite the exposure of the Sheephead Fault, the kinematics of the fault is still a topic of debate. Many authors have suggested dextral movement along the Sheephead Fault (e.g. Wright, 1974; Stewart, 1983; Wright et al., 1991; McMackin, 1992; Prave and McMackin, 1999; Renik, 2010; Renik and Christie-Blick, 2013) and the fault played heavily in Wright et al.'s (1991) inference that the fault was a dextral southern boundary to an earlier, proto-Death Valley pull-apart basin. In contrast, others have interpreted a sinistral movement of the fault (e.g. Wright and Troxel, 1984; Holm and Wernicke, 1990; Topping, 1993; Mancktelow and Pavlis, 1994; Serpa and Pavlis, 1996; Snow and Wernicke, 2000). Indeed, Pavlis, in Holm et al. (1994) presented fault kinematic data in support of sinistral-oblique motion, at odds with the interpretation of Renick (2010). The fault was a key element of reconstructions by Serpa and Pavlis (1996) in their inference that the fault was an old, eastern extension of the Garlock fault, forming a key transrotational feature during the Miocene extension.

3.4.2 Grand View Fault

The Grand View Fault bounds the eastern side of the Black Mountains and the western side of the Greenwater Range (Figure 3.1) but is covered by Quaternary deposits along most of its interpreted

trace (Hillhouse, 1987; Topping, 2018; Fridrich and Thompson, 2011). The Grand View Fault is interpreted as having a dextral sense of movement with as much as 15 km of offset (Topping, 1993). Of additional importance to the work presented here, the Grand View Fault offsets the deposits of the China Ranch Basin (Prave and McMackin, 1999), which includes the Sperry Hills basin deposits of Topping (1993) (Figure 3.1). Because of the extensive Quaternary cover, an allowable interpretation is that the Grand View Fault becomes the Sheephead Fault west of the Kingston Peak Range (Figure 3.1), rather than the more widely cited connection defining the Sheephead fault trace (e.g. Wright, 1974; Topping, 1993; Prave and McMackin, 1999). Here I use the interpretation of Topping (1993) that the Grand View Fault is independent of the Sheephead Fault and the structure in the Alexander Hills is the Grand View Fault (Figure 3.1).

3.4.3 Ibex Pass

The Neogene deposits in the Ibex Pass area (Figure 1) are essential to reconstructing the offset of the adjacent Ibex Hills range, providing both kinematic and temporal constraints (e.g. Topping, 1993; Canalda, 2009). Within Ibex Pass is a sequence of Tertiary volcanic deposits which were studied in detail by Canalda (2009). In the northern Saddle Peak Hills these volcanic deposits lie above a marked angular unconformity on Neoproterozoic rocks ranging in age from Noonday Formation to Stirling Quartzite, but in the Ibex Hills this unconformity was only found at one locality in the southern Ibex Hills (Figure 3.4). However, an intrusive unit similar to those mapped by Canalda (2009) was mapped in the northern Ibex Hills (Figure 3.5). In both areas the volcanic rocks either lie directly on Neoproterozoic, or are separated by a thin, poorly exposed gravel.

The Neogene volcanic sequence begins with ~100 meters of massive, variably altered dacite (Figure 3.4 and 3.5) (Candalda, 2009; Mahon and Link, 2013). Above the dacite unit is a pyroclastic unit, upwards of 300 meters thick. This unit is comprised of volcanic breccias and conglomerates ranging

from trachyandesite to rhyolite (Canalda, 2009). The lower dacite and pyroclastic units are intruded by a trachyte to trachyandesite that is intensely altered and forms a poorly defined pluton just north of the Saddle Peak Hills (Canalda, 2009). Atop the pyroclastic section in Ibex Pass is a distinctive tan to white tuff unit which reaches ~10 meters in thickness and ranges from a lithic tuff to a more ash dominated deposit (Canalda, 2009). A similar white tuff occurs in the southern Ibex Hills Tertiary section, but in that section the tuff lies below a sequence of volcanic flows (Figure 3.4), rather than within the pyroclastic unit seen to the north in Ibex Pass (Figure 3.4 and 3.5). This tuff unit at the southern Ibex Hills is tentatively correlated to that of Canalda (2009) which implies the volcanics of the Ibex Hills represent a younger sequence than those to the north of the Saddle Peak Hills (Figure 3.4).

The tuff unit of Ibex Pass has been interpreted differently by previous workers. Topping (1993) correlated this tuff to the ~10 Ma Rhodes Tuff, which would make the Ibex Hills rocks broadly correlative to the rocks of the Amargosa Chaos Basin. Alternatively, Canalda (2009) correlated the rocks to the volcanic units in the northeastern Owlhead Mountains, consistent with a tentative correlation by Luckow et al. (2005).

Geologic mapping also confirmed the presence of a granitic mega-breccia along the flank of the central Ibex Hills (Figure 3.2), which was also mapped north of the Saddle Peak Hills by Canalda (2009). In some locations in Ibex Pass mono-lithic breccias of Beck Spring Dolomite and the Noonday Formation overlie the granitic mega-breccia (Figure 3.2), the granitic breccia itself is presumably sourced from the Kingston Peak Granite (e.g. Topping, 1992; Canalda, 2009). This mega-breccia deposit is a key piercing line for the reconstruction discussed herein as it must be restored to within a reasonable landslide runout range from Kingston Peak (Figure 3.1).

3.5 METHODOLOGY

3.5.1 Creation of 3D Geologic Model

Move 2017 by Midland Valley (www.mve.com) was utilized to create the 3-dimensional model and reconstruction of the Ibex Hills (Figure 6, see 3D pdf). The piercing lines for the reconstruction were primarily the result of recent geologic mapping of the Ibex Hills, presented in the previous chapter, in combination with previous work in the region (e.g. Wright and Troxel, 1974; Topping, 1993; Canalda, 2009; Renik, 2010; Mahon and Link, 2013).

The first step in the reconstruction was to build 3-dimensional layers representing the major fault surfaces of the Ibex Hills, namely Fault A, Fault B, Fault C, and Fault D (to use the terminology of Chapter 2) (Figure 3.5). The process of creating these fault surfaces is relatively straight forward in Move 2017 once cross-sections of the study area have been constructed. In order to simplify the process, the cross-sections used for building the model were those in which slip on high-angle normal faults had already been restored (Chapter 2). Using these cross-sections, surfaces were created to connect the corresponding contacts between the sections (i.e. the Noonday Fault in Section A was “connected” to Section B via a 3-dimensional surface). This process is accomplished in Move 2017 by using the function of “create surface from lines” option under the “Surface” dialog box in the main toolbar of the program (Figure 3.7).

After the initial surface is created it can then be extended to the desired area and adjusted and smoothed to fit other lines, points, etc. This step is essential as the initial surfaces will only fill the area between the selected lines. Additionally, I found that selection of more than two lines per surfaces created unrealistic surfaces and therefore extending the surfaces is necessary to fill the study area. The extended areas of the plane can then be fit to relevant contacts elsewhere in the map area. This process of surface construction was repeated for the formational contacts of the northern Ibex Hills for the reconstruction (Figure 3.7).

In addition to the low angle faults in the Ibex Hills, the fault planes of the Sheephead Fault, the Eastern Boundary Fault of the Ibex Hills, and the Grand View Fault were incorporated into the model as well (Figure 3.6). The traces of these faults were taken from previous work (Wright, 1974; Topping,

1993; Renik, 2010), however, given the uncertainty of the trace of the Sheephead Fault it was simply projected into Ibex Pass until it merged with the Grand View Fault (Figure 3.6). Cross-sections of the southern Nopah Range, the Alexander Hills, and the Saddle Peak Hills were also put into the model for reference (Figure 3.1 and 3.6).

3.5.2 Determining Piercing Lines for Reconstruction

In order to reconstruct the kinematic history of the Ibex Hills in the context of the southern Death Valley region, reasonable piercing lines needed to be determined for the model. These piercing lines arise mostly from the geologic mapping discussed in the previous chapter, although one of the key depositional observations of the Noonday Formation was previously observed by Wright and Troxel (1974). Figure 8A-F (see 3D pdfs) show the steps of reconstructing the Ibex Hills within the southern Death Valley region using these piercing lines.

In the northernmost Ibex Hills, a previously unmapped igneous body was recognized within the the Johnnie Formation (Figure 3.5). The contact of the igneous deposit with the Johnnie Formation is similar to the intrusive unit that was mapped by Canalda (2009) at the northern end of the Saddle Peak Hills (Figure 3.5). The map pattern of the igneous unit in the Ibex Hills suggests an intrusive origin as it is bounded on both sides by the Johnnie Formation and appears to pinch out ~500 meters along strike (Figure 3.5). Phenocrysts of plagioclase and amphiboles are present in the rock and it weathers to a deep maroon. This fits reasonably well with the descriptions provided by Canalda (2009) of the Saddle Peak Hills intrusion (Figure 3.5). Geologic mapping presented in the last chapter placed this igneous deposit, and the Johnnie Formation it is in contact with, in the hanging-wall of “Fault D” (terminology of this work). Given that Fault D is interpreted as having a northwest directed sense of movement in the hanging-wall, a source area of the northern Saddle Peak Hills and/or Ibex Pass area is a likely candidate (Figure 3.5). Based on this evidence, the igneous deposit of the northern Ibex Hills was used as a piercing point to reconstruct the cumulative northwest directed extension in the range (Figure 3.5 and 3.8A&B).

Another key deposit in the Ibex Hills is the granitic megabreccia found along its eastern flank of the range and across broad regions of the Ibex Pass area (Figure 3.2). Previous work by Topping (1993)

used similar deposits to reconstruct movement along the Amargosa Detachment and the Grand View Fault by interpreting a Kingston Range granite source, a large a granitic intrusion in the Kingston Range (Figure 3.1). Later work has also supported the presence of landslide derived, Kingston Range granite in Ibex Pass (e.g. Calzia and Ramo, 2000; Canalda, 2009). However, this study recognized exposures of the granitic megabreccia in the Ibex Hills ~10-12 km farther west than those previously mapped. Assuming the same source as the other granitic rocks found in Ibex Pass, the reconstruction of the newly mapped megabreccia to within 10 km of the Kingston Range is required. This estimate of 10 km is based on a compilation of empirical data for landslide runouts, presented by Topping (1993).

The unconformity at the base of the Noonday Formation is exposed in the hanging-wall of the southwest directed, low-angle faults of the Ibex Hills (Figure 3.9). The units present immediately below the Noonday Formation unconformity are variable throughout the southern Death Valley region (Wright and Troxel, 1974). In the southernmost portion of the region, thick sequences of the Beck Springs Dolomite and Kingston Peak Formation lie below the unconformity, however, farther north, these units are stratigraphically cut out until the lower Noonday Formation is directly atop the Crystal Springs Formation and 1.7 Ga crystalline basement rock (Wright and Troxel, 1974). Wright and Troxel (1974) interpreted this change as evidence for a regional, east-west basin known as the Amargosa Aulacogen. In the northern Ibex Hills, the basal Noonday unconformity is exposed directly above ~100 meters of the Beck Spring Dolomite, in its southernmost exposure (Figure 3.9). Farther north in the Ibex Hills the unconformity cuts out the Beck Spring Dolomite and Noonday rests above the Horse Thief Springs Formation and minor lenses, ~5-10 meters in thickness, of the upper Kingston Peak Formation (Figure 3.8). The nearest eastern equivalent to this relationship is seen in the Alexander Hills to the southern Nopah Range (Figure 3.9) (Wright, 1974; Wright and Troxel, 1974). Restoring this unconformity is a requirement of any reconstruction of the Ibex Hills and is therefore a key piercing line for this work.

3.5.3 Other Considerations

In order to accurately reconstruct the structures of the Ibex Hills, two other regional effects were considered. The first of these is the tilting of the ranges which occurred during extension. To estimate the magnitude of this range tilting the orientation of volcanic deposits in the southern Ibex Hills was

used. In this case, volcanic layering is oriented at an approximately north-south strike, dipping $\sim 30^\circ$ to the east. The estimate of 30° is consistent with the evidence found elsewhere in Ibex Pass by Canalda (2009). The second consideration was that of clockwise vertical axis rotation which has been suggested for Death Valley, primarily because of rotation of the Mojave block to the south and paleomagnetic data from plutonic rocks in the Black Mountains (e.g. Serpa and Pavlis, 1996; Guest et al., 2003). Estimates for the amount of clockwise rotation in Death Valley range up to 45° (Guest et al., 2003), however, previous regional models have used variable estimates (e.g. Serpa and Pavlis, 1996). Constraints on this rotation were not found directly in geologic mapping in the Ibex Hills, however, it was found that reconstruction was not feasible without some clockwise rotation of the range (Figure 3.8). Two options are presented in the final reconstructions: the first incorporates significant left-lateral offset along the Sheephead Fault (Figure 3.8E), the second option only incorporates the Sheephead Fault as a minor feature which accommodates regional clock-wise rotation (Figure 3.8F). In both cases rotation was required to bring the granite megabreccia to within 10 km of the Kingston Range, with a minimum of 15° needed between the two options (Figure 3.10).

3.6 RESULTS

3.6.1 Northwest Directed Extension

Figure 3.6 shows the model of the Ibex Hills with the high-angle normal faults of the range as well as the inferred range tilt restored. The piercing line of the northwest directed extension is the intrusive mapped by Canalda (2009) which lies 14 km southeast of the northern Ibex Hills intrusive (Figure 3.5). The first step in the model reconstruction involved the restoration of both the Eastern Boundary Fault (EBF) and Fault D (Figure 3.8A). The EBF was interpreted to have a horizontal, right-lateral, offset of 4 km, based on the geologic mapping presented in the previous chapter of this dissertation, and this was the value used in this step of the model (Figure 3.8A). Following this Fault C was then restored, combined with Fault D the cumulative low-angle restoration for this step was 5.1 km (Figure 3.8B). In addition, the restoration of the EBF restored the intrusive of the northern Ibex Hills another 3.9 km closer to those of Ibex Pass (Figure 3.11).

After these restoration steps, there is still ~5 km of horizontal distance between the northern Saddle Peak Hills and the northern Ibex Hills (Figure 3.8B). To accommodate this motion there may be other structures, in addition to Faults C and D, that are not clearly present in the Ibex Hills. Alternatively, the reconstructions of movement along Faults C and D done in the previous chapter may have been underestimated. Given the reconstructions of the previous chapter relied on an inferred footwall stratigraphy, as it is currently buried in the basin adjacent to the Ibex Hills (Figure 3.1), an unrecognized pre-extensional geometry of the footwall could result in an underestimate of Fault C and D offset. Therefore, since the source of the additional offset is currently ambiguous, a simple southeastward translation of 5 km was performed on Faults C and D, along with their respective hanging walls to fully restore the intrusion to a position atop the intrusion in the Saddle Peak Hills (Figure 3.12, see 3D pdf). Figure 3.12 also contains a cross-section of the Saddle Peak Hills to compare to the restored surfaces. A key similarity seen in the Saddle Peak Hills cross-section is the presence of two, nearly parallel, low-angle normal faults which carry the Noonday Formation and the Johnnie Formation in their respective hanging-walls (Figure 3.12) (Mahon and Link, 2013). This is analogous to “Fault C” and “Fault D” of the Ibex Hills and when they are restored they line up roughly with the two low-angle faults of the Saddle Peak Hills (Figure 3.12).

The timing of this movement is interpreted to have occurred no earlier than 7.8 Ma which is based on the work of Topping (1993). The pre-7.8 Ma stratigraphy of the Sperry Hills Basin and the Amargosa Basin, which include the granite megabreccias of Ibex Pass, contains rock avalanche deposits associated with the Kingston Range, suggesting that until 7.8 Ma the basin was within 10 km of the range (Topping, 1993). Based on these interpretations northwest directed extension and transtension did not occur until ~7.8 Ma (e.g. Topping, 1993; Prave and McMackin, 1999). Further constraints of northwest extension in the region is provided by zircon (U/Th)-He in Confidence Wash, west of the Ibex Hills (Bidgoli et al., 2015). The data of Bidgoli et al. (2015) are consistent with an onset of extension at ~8 Ma and show a plateau at ~6 Ma, which the authors interpreted as a westward migration and shift to a more transtensional dominated regime.

In addition, while the age of the volcanics of the Ibex Hills have not been determined, unpublished K-Ar data indicates an ~12 Ma age for the dacite package in Ibex Pass (Calzia and Ramo, 2000; Canalda, 2009) which is consistent with its position in the hanging-wall of the younger normal faults of the Ibex Hills. The EBF is also constrained by the volcanics of the Ibex Hills as it cuts them in the southern part of the range. Additionally, the EBF appears to behead the Noonday and Becks Springs mega-breccias along the central portion of the range. These mega-breccias, which overly the granitic mega-breccia, are likely coeval with EBF movement.

3.6.2 Offset Along the Sheephead Fault and/or Grand View Fault

The next step of the reconstruction was to restore the Ibex Hills such that the granite megabreccia is within 10 km of the Kingston Range (Figure 3.8C and E). In order to accomplish this, two options were considered: 1) a Grand View Fault only option and 2) a Grand View and Sheephead fault option.

In the first case, attempting to restore the Ibex Hills in a single step, it became clear that movement only along the Grand View Fault would not place the megabreccia within 10 km of the Kingston Range and a 30° vertical axis rotation was needed to place it in an allowable position (Figure 3.8C and 3.10). Without this vertical axis rotation, the megabreccia was restored too far south of the Kingston Range (Figure 3.10). After the clockwise rotation of 30° a heave of 28 km along the Grand View Fault was used to bring the granite megabreccia of the Ibex Hills to within 10 km of the Kingston Range (Figure 3.2 and 3.8C). This magnitude of offset is of greater magnitude than that given by Topping (1993) by more than 10 km. While it should be acknowledged that some of the offset used herein could be, and must be to some extent, accommodated by normal faulting between the Ibex Hills, Saddle Peak Hills, and other ranges to the east (Figure 3.1), the model still suggests previous work underestimates the magnitude of right-lateral offset in the region.

The timing of movement along the Grand View Fault is no more constrained than that of northwest directed extension in the Ibex Hills and these may, in fact, have been concurrent events in a context of overall northwestward movement. The restoration of the Ibex Hills along the Grand View Fault fits well with the results of the previous chapter, which suggest early southwest directed extension.

Assuming this is correct the source of the hanging-walls of these early faults must come from the northeast, which at the stage of Figure 3.8C indicates the southern Nopah Range as it contains the same basal Noonday Unconformity-Horse Thief Springs Formation contact found in the Ibex Hills (Figure 3.9). Given the presence of the Beck Springs Formation and Kingston Peak Formation in the Alexander Hills and the Kingston Range, the Nopah Range is the most plausible candidate.

The second option considered in the model was one which incorporated offset along the Sheephead Fault, north of the Ibex Hills (Figure 3.1). In this scenario 12 km of right-lateral slip was restored along the Sheephead Fault, which was simply the maximum amount allowed in the model without moving the Ibex Hills east of the Grand View Fault (Figure 3.1). Following this the Ibex Hills were then translated ~20 km along the Grand View Fault (Figure 3.8E). In this scenario a restoration of clockwise, vertical axis rotation is again required, however, in this case it is a minimum of 15° (Figure 3.8E and 3.10). The offset along the Grand View Fault in this second option is closer to, albeit still greater than, the 15km magnitude suggested by Topping (1993).

3.6.3 Southwest Extension

The final stage of the Ibex Hills restoration is restoring the movement of the low-angle, southwest directed normal faults of the range (Figure 3.8D and E). The unconformity at the base of the Noonday Formation was a key piercing line in restoring the motion of the Ibex Hills and to equivalents in the Nopah Range and Alexander Hills (Wright, 1974) to estimate the offset of this contact (Figure 3.8D&E and Figure 3.13). At the southern end of the Nopah Range the lower Noonday Formation is in contact with the uppermost Crystal Spring Formation (Wright, 1974). This is equivalent to the contact between the Noonday Formation and the Horse Thief Springs Formation seen in the Ibex Hills.

Faults A and B were then restored a total of 2.4 km horizontally for both of the model options discussed above (Figure 3.8D&E). After the reconstruction of the low-angle normal faults a horizontal distance of ~10.5 km remains between restored Ibex Hills and the northernmost Alexander Hills (Figure 3.13) for both options, suggesting significant southwest directed extension effected the range beyond that of Faults A and B. Given the proximity of the Kingston Range Detachment it is likely that this could

have accommodated much of this offset, although previous estimates only suggest ~6 km of southwest directed extension for the Kingston Range Detachment (Figure 3.13).

The timing of the modeled southwest directed extension is interpreted to have occurred between ~13.4-12.4 Ma. This is based on the cross-cutting relationships of the Kingston Range Detachment and ~13.4 Ma sills as well as the timing of emplacement for the Kingston Peak granite, which is interpreted to have ceased movement along the detachment (Davis et al., 1993; Fowler and Calzia, 1999; Calzia and Ramo, 2000). Given the proximity of the restored Ibex Hills to the Kingston Range it is likely that the extension of the two ranges is at the very least temporally related, making this a reasonable estimate for southwest directed movement in the Ibex Hills. However, Canalda (2009) mapped a number of minor north-northwest striking normal faults and northeast striking sinistral faults in Ibex Pass which kinematically agree with southwest directed extension (Figure 3.5). Assuming an ~12Ma age for the volcanics of Ibex Pass, this suggests southwest directed extension may have persisted past previous estimates.

3.7 DISCUSSION

The position of the Ibex Hills in the context of the southern Death Valley region is the result of both southwest directed extension and later northwest directed strike-slip and normal faulting (Figure 3.8). The model presented here suggests that the Ibex Hills rocks lay just south of the Nopah Range prior to extension (Figure 3.1, 3.8 and 3.10). Given the proximity to the trace of the Kingston Range Detachment (Figure 3.1) the southwest-directed normal faults of the Ibex Hills likely records extension related to the detachment. Previous work identified multiple listric normal faults in the hanging wall of the Kingston Range Detachment which generally have horizontal offsets of 1-2 km (Fowler and Calzia, 1999). Given the total heave of Faults A and B is 2.4 km they may very well represent such hanging wall faults.

After reconstruction of the Ibex Hills along the Grand View Fault, more than 10 km remains between the northern Alexander Hills and the restored Ibex Hills (Figure 3.8 D&E). The fact that the basal Noonday unconformity found in the Ibex Hills is not present south of the Nopah Range suggests further restoration is needed. One possibility is the Ibex Hills were transported along the Kingston

Range Detachment, in line with the interpretation of Faults A and B as faults in the hanging wall of the detachment. If this is the case, it potentially updates the previous estimates of 6 km of displacement along the Kingston Range Detachment (Fowler and Calzia, 1999) to up to 10 km of horizontal displacement (Figure 3.13). However, evidence for left-lateral slip along northeast striking faults in the Ibex Pass area (Canalda, 2009) would suggest some amount of southward translation of the Ibex Hills after movement on the Kingston Range Detachment. This translation may make up for the differences in offset for the Kingston Range Detachment in this scenario and those of previous authors (e.g. Fowler and Calzia, 1999), Nonetheless, little constraint is provided for the strike-slip movement in Ibex Pass at this time. Additionally, a northeast striking, left-lateral offset of ~1.5 km is mapped between the Nopah Range and the Alexander Hills which would also accommodate some of the remaining 4 km (Figure 3.13).

Better constraints on the amount of clockwise rotation in southern Death Valley would refine the reconstruction presented here, however, the model strongly supports a vertical axis rotation for the Ibex Hills. The estimate of 15-30° is likely on the high end for the Ibex Hills, again because of the unknown sinistral offset within Ibex Pass which would decrease the necessary rotation to align the Ibex Hills granite megabreccias to the runout zone of the Kingston Range (Figure 3.8C). In the first model option presented here (Figure 3.8E), the Sheephead Fault is interpreted as a passive to sinistral structure, and accommodates clockwise rotation (Figure 3.8E).

Rotation of the Ibex Hills might also explain the folding and reverse faulting of the low-angle fault systems, as discussed in the last chapter. If the Ibex Hills rotated as an individual block, and at a different rate than the surrounding area, there would likely be some regions of compression in the range. Alternatively, if the Sheephead Fault was a dextral structure, the folding may have been produced due to contractional “step-over” in the fault trace via the mechanisms outlined by Mancktelow and Pavlis (1994) (Figure 3.9). Previous supporters of this scenario have suggested that the Sheephead Fault may have accommodated upwards of 18 km of dextral offset (Renik, 2010; Renik and Christie-Blick, 2013). In the second model option presented here the Sheephead Fault is interpreted to have transported the Ibex Hills ~12 km in a right-lateral sense.

Of the two scenarios for the Sheephead Fault the sinistral hypothesis is preferred here, based on the evidence for regional rotation elsewhere in southwestern Death Valley (e.g. Serpa and Pavlis, 1996; Guest et al., 2003), the need for a structure to accommodate that motion assuming it extends into southeast Death Valley, and the fit with the general map pattern of the region (Figure 3.9) (Wright and Troxel, 1984). In addition, the kinematics of the “Eastern Boundary Fault”, presented in the previous chapter, indicate a highly oblique, right-lateral sense of movement which is consistent with northeastward translation of the Ibex Hills (Figure 3.9) (Fleming and Pavlis, 2018). Given that the northern trace of the Eastern Boundary Fault is ambiguous in the Ibex Hills, the structure may be a conjugate to a left-lateral Sheephead Fault in this rotational system.

Another possible piece of evidence for the sinistral Sheephead Fault hypothesis are the similarities between the low-angle faulting of the Ibex Hills and those recognized by Castonguay (2013) in the Amargosa Chaos to the northwest (Figure 3.1). Most notably a sequence of localized, low-angle normal faults which appeared to have been folded after their inception (Castonguay, 2013). Currently, there is ~15km between the northern Ibex Hills and the Amargosa Chaos along the approximate trace of the Sheephead Fault (Figure 3.14). Assuming a 30° clockwise rotation of the Ibex Hills took place, an estimate of ~10km of movement would have occurred along the arc of that rotation using an inferred radius equal to the length of the Ibex Hills, 19km (Figure 3.14). Since the radius of such a rotation is not known this is interpreted as a conservative estimate since it was likely a regional event with an axis of rotation farther south than the Ibex Hills, and therefore resulting in a larger radius and arc length. The remaining 5km of offset between the Amargosa Chaos and the Ibex Hills can be almost entirely accommodated by ~4.5km of offset inferred between the Ibex Hills and the adjacent area of Confidence Wash (Figure 3.1 and 3.14). The estimated offset between the Ibex Hills and the Confidence Wash area was based on outcrops of Beck Spring Dolomite (Figure 3.14). Assuming the Beck Spring Dolomite of the Confidence Wash area was displaced from the Ibex Hills the current distance of 4.5km between the two provides an approximation of that displacement (Figure 3.14). These offset estimates, alongside the similarities of the northern Ibex Hills and the Amargosa Chaos, are consistent with a sinistral Sheephead Fault that displaced the two.

The reconstruction of the Ibex Hills is an example of how important it is to consider the multi-phase extensional and transtensional history of the Death Valley region. While alluded to, previous extensional models have all but ignored the presence of southwest directed extension as far west as the Ibex Hills. Additionally, the fact that the bulk of the transport seen by the Ibex Hills was accommodated by strike-slip faults, regardless of whether it was the Grand View Fault alone or in combination with a right-lateral Sheephead Fault, highlights the influence of these types of structures in the region and is counter to the notion of a single regional detachment surface (e.g. Snow and Wernicke, 2000). Although the existence of a more localized detachment (i.e. the Black Mountain/Amargosa Detachment) perhaps continuous with the Amargosa Chaos (Figure 3.1) is not precluded by this work.

It is also important to note that after the final step of reconstruction, the dip of Faults A and B remains quite low, $<30^\circ$ for the most part (Figure 3.8 D and E). A simple explanation for this mechanically difficult orientation is that this reconstruction only considered the range tilt of the Ibex Hills, as that was the only constraint directly measured. However, it remains likely that the hanging wall rocks of the Ibex Hills incurred multiple phases of tilting, and the assumption here is an oversimplification.

3.8 CONCLUSIONS

Data presented here suggests that the Ibex Hills contain displaced bedrock from early southwest directed extension, originally located south of the Nopah Range and displaced ~ 13 km (Figure 3.8 and 3.13). This material was then transported to the northwest upwards of 28 km along the dextral Grand View/Sheephead Fault system after ~ 8 Ma (Topping, 1993). Northwest directed extension was also taking place during that time, reflected in the Ibex Hills by low angle normal faults and younger, high-angle faults that cut them. The structurally highest of these low-angle normal faults, Faults C and D, fit well with the geology of the Saddle Peak Hills to the southeast and suggest a collective heave of up to 14 km (Figure 3.8 and 3.11). The normal faulting of the Ibex Hills likely persisted until at least ~ 6 Ma, based on nearby thermochronology (Bidgoli et al., 2015). The reconstruction presented here also suggests between 15 - 30° of clockwise rotation was incurred by the Ibex Hills.

Despite its position in the southern Death Valley region, little attention has been given to the Ibex Hills, however, the model presented here shows it contains key piercing lines for regional reconstructions. The complexity found in the range, along with evidence for multiple extension directions and later shortening, also highlights the importance of employing 3-dimensions in any reconstructions in the Death Valley region.

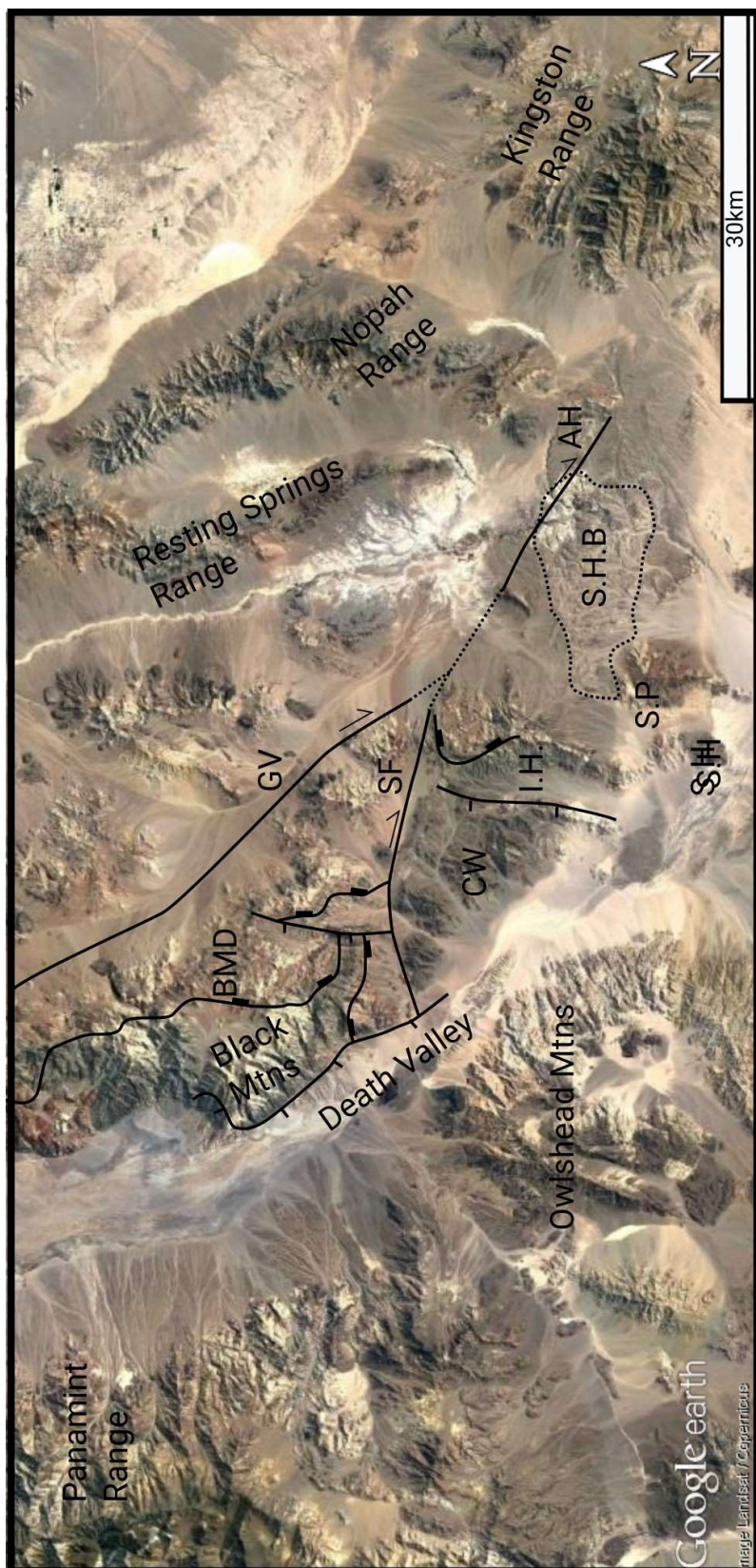


Figure 3.1. Map of key geographical and geologic features discussed in the text. AH- Alexander Hills, GV- Grand view Fault, SF-Sheephead Fault, BMD-Black Mtn. Detachment, CW-Confidence Wash, IH- Ibex Hills, SP-Saddle Peak Hills, SH-Saratoga Hills, SHB – Sperry Hills Basin.

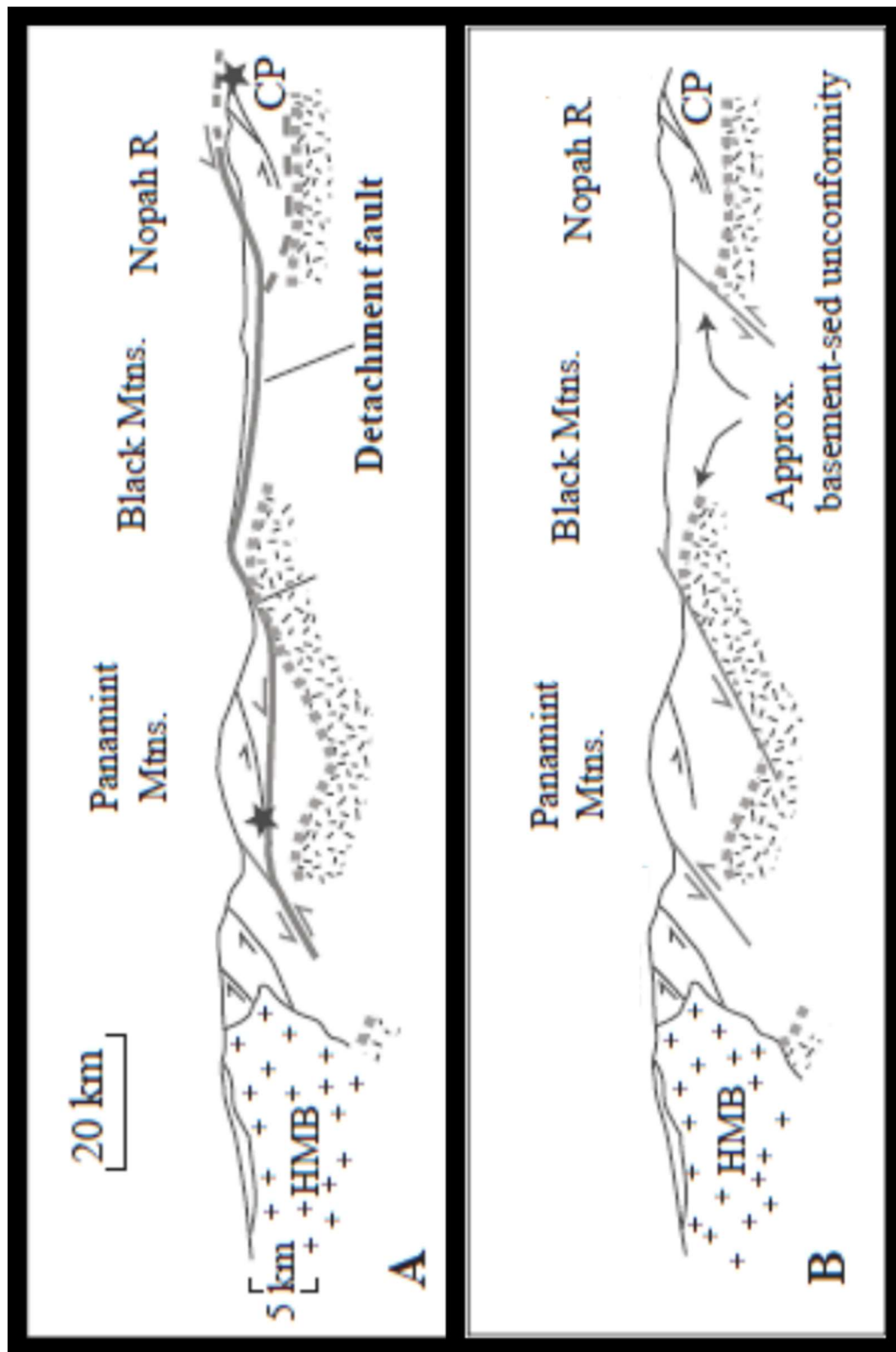


Figure 3.3. A. shows the rolling-hinge model as it pertains to the Death Valley region. B. shows an example of a discrete system of extensional faults for the region. Modified from Miller and Pavlis (2005).

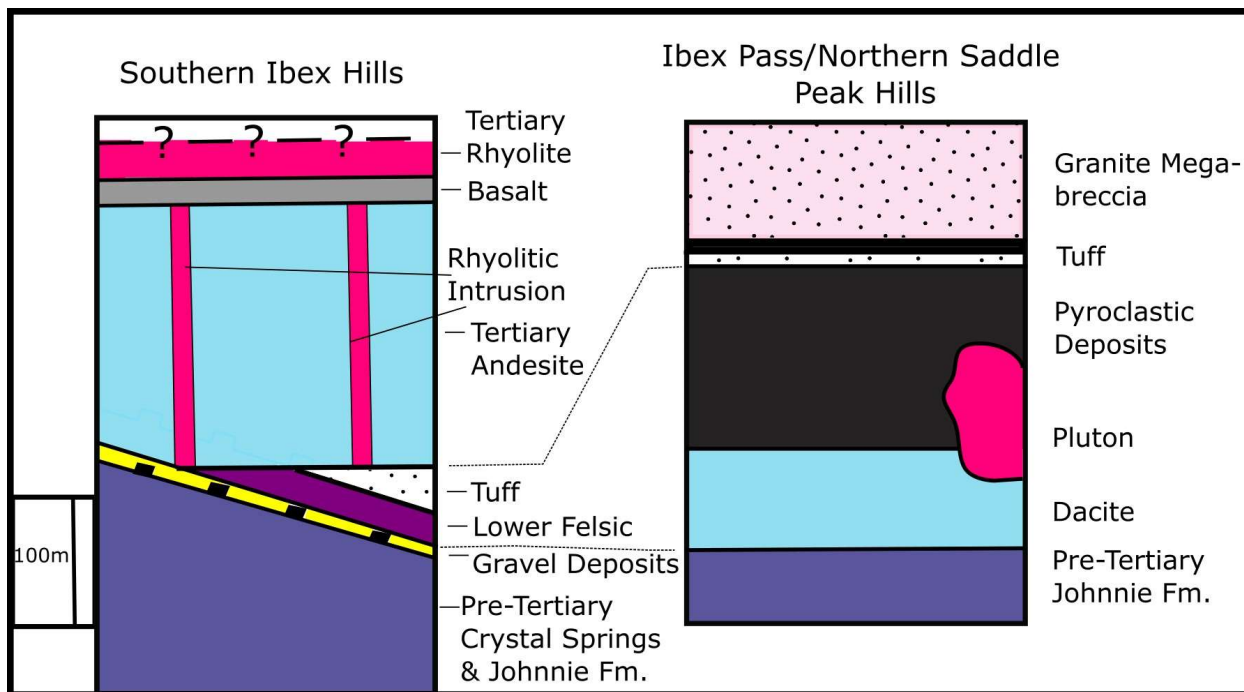


Figure 3.4. Comparative stratigraphic sections of the volcanic packages in the southern Ibex Hills and those of Canalda (2009), north of the Saddle Peak Hills.

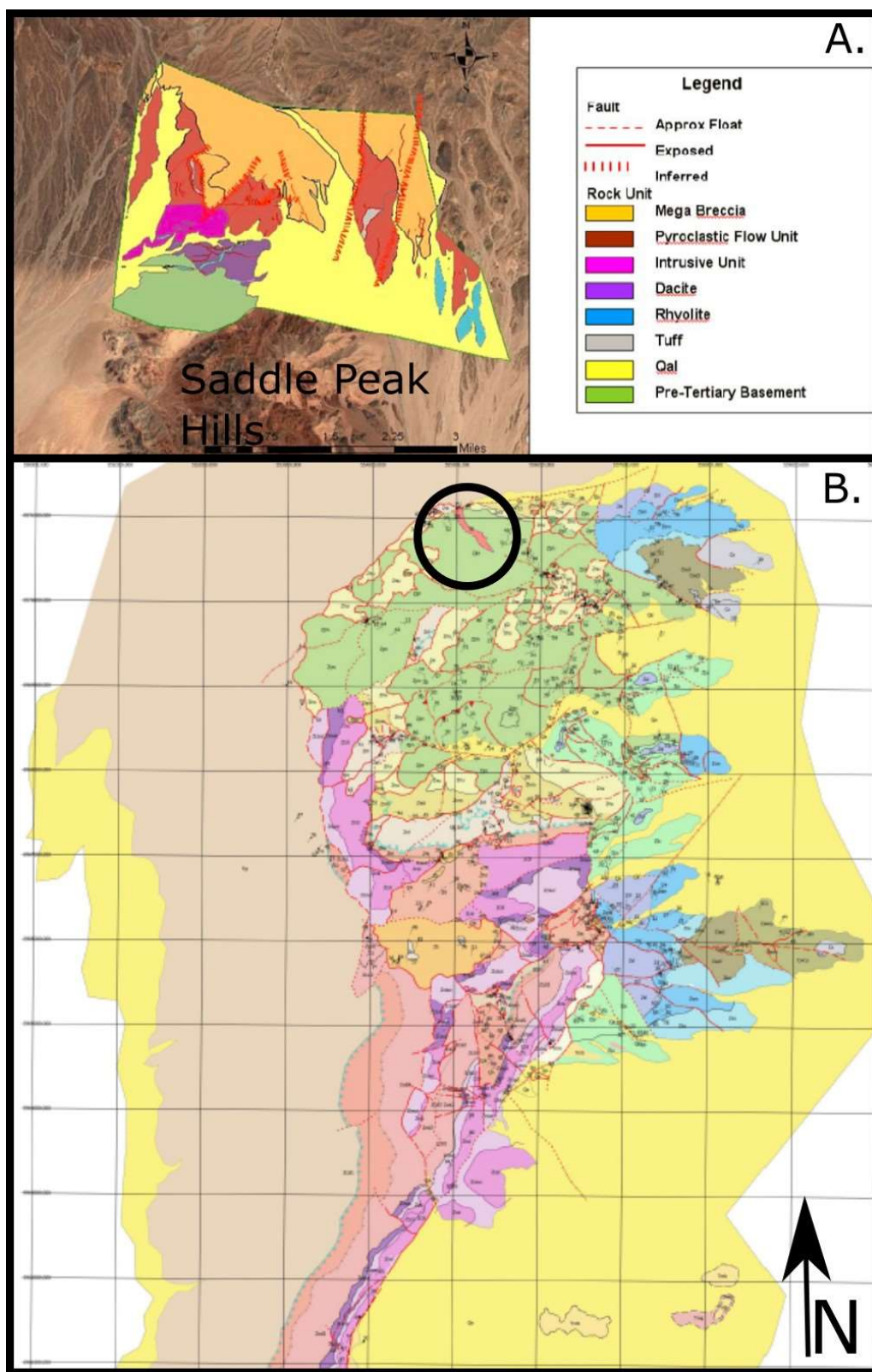


Figure 3.5. A. The mapping of Canalda (2009) in Ibex Pass and the northernmost Saddle Peak Hills. B. Same mapping area as Figure 2 in the Ibex Hills with the newly mapped volcanic unit circled.

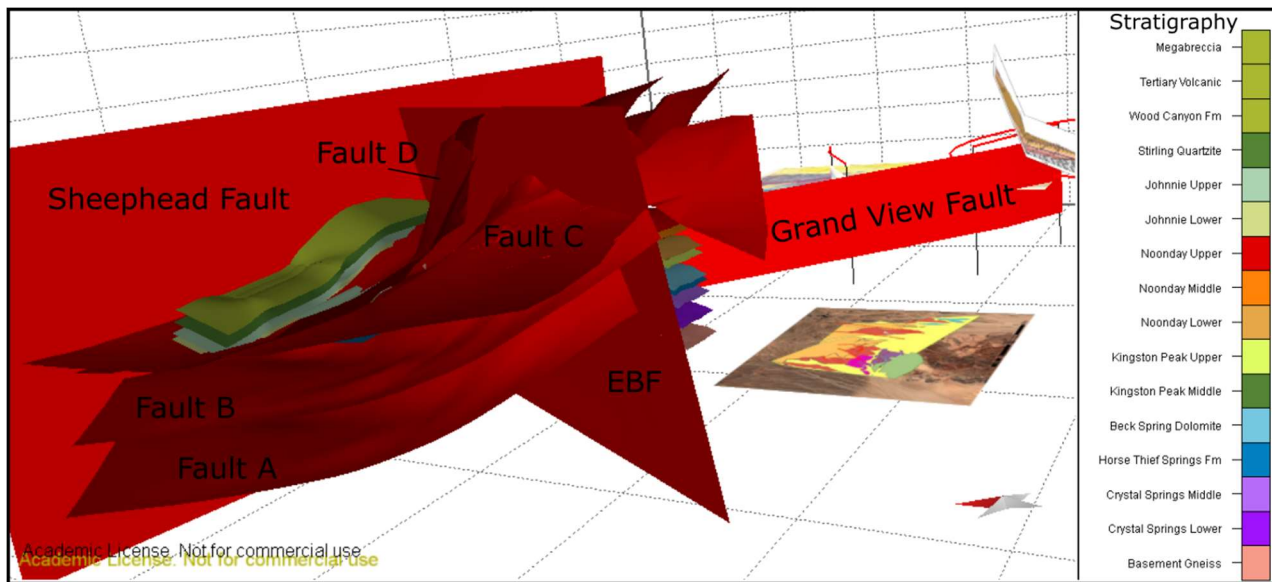


Figure 3.6. A. See associated .pdf. 3D structural model of the Ibex Hills after restoration of only the moderate to high-angle normal faults. B. Below is a screenshot of the model with the major faults labeled along with the colors used for the stratigraphy. These colors are consistent through the other model steps presented in this work.

Figure 3.8. See associate 3D .pdf. A. Model after restoration of the EBF and Fault D. B. After the restoration of Fault C. C. After restoration along the Grand View Fault only. D. After restoration along the Sheephead Fault and the Grand View Fault. E. Following SW directed restoration after the model of 8D.

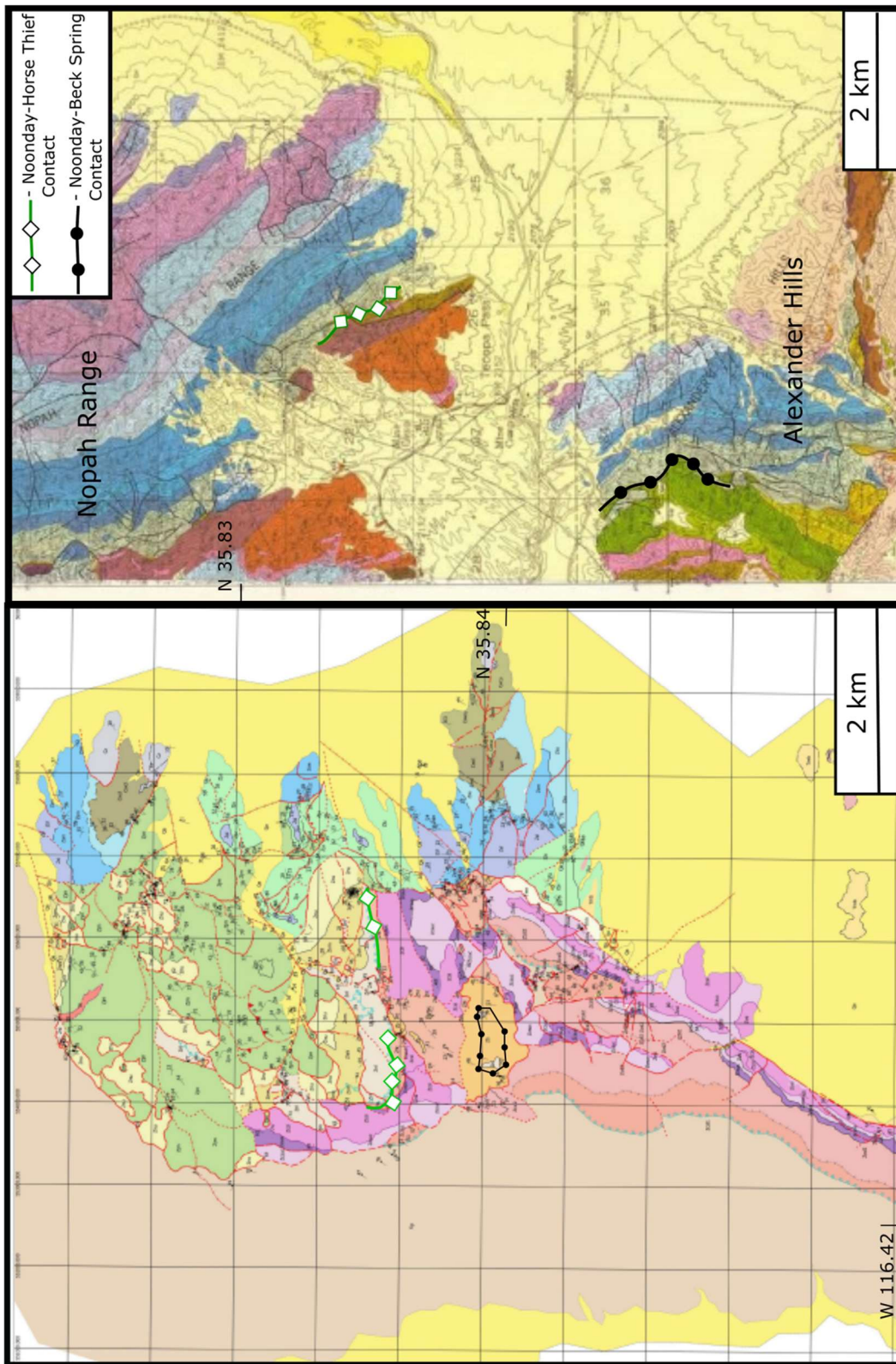


Figure 3.9. Maps showing the location of the basal Noonday unconformity in the Ibex Hills (left) and the Nopah Range/Alexander Hills (right).

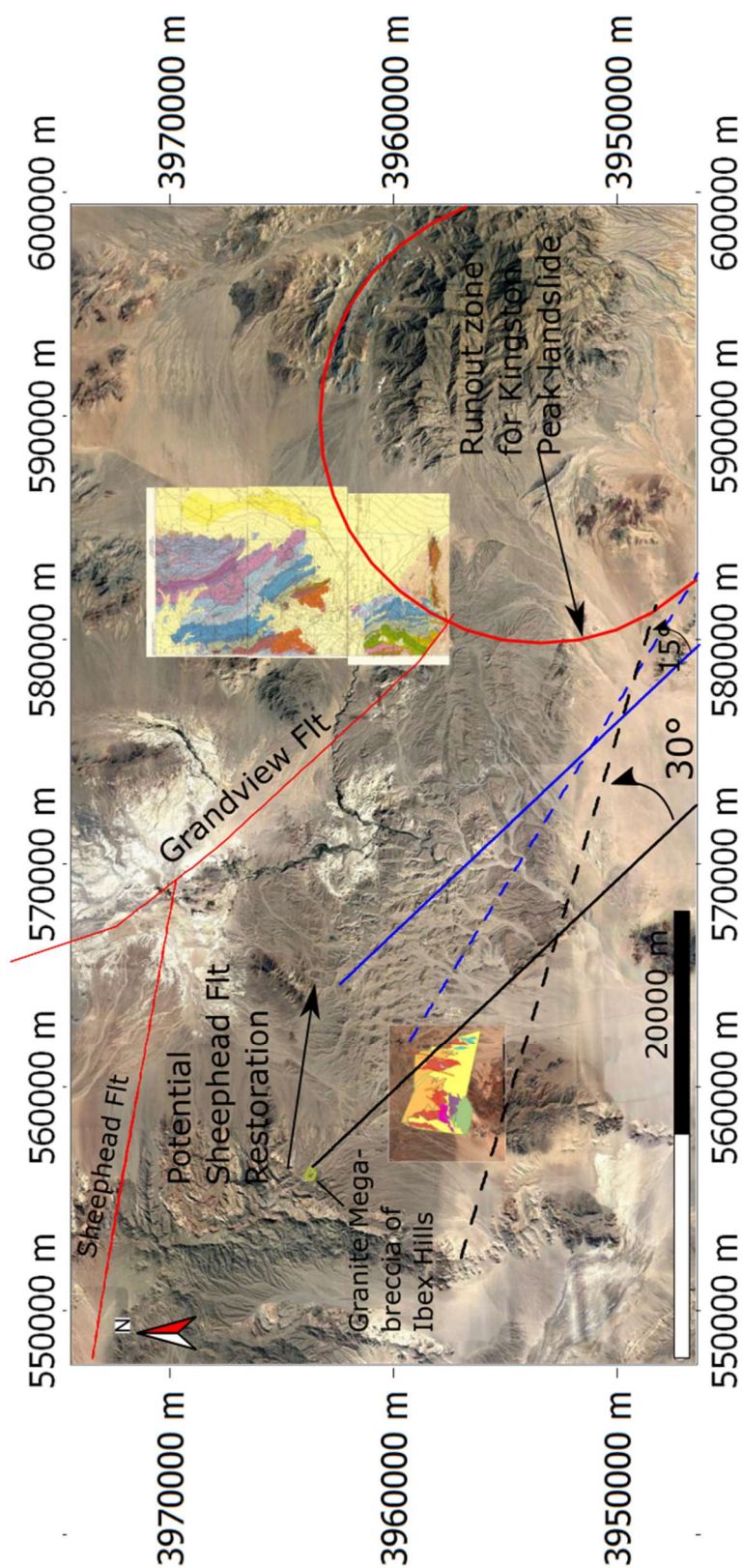


Figure 3.10. Map showing the potential paths of restoration for the Ibex Hills granitic mega-breccia. The solid black line is the path of restoration along only the Grand View Fault, which requires 30° of rotation to restore properly (black dashed line). Alternatively, the solid blue line is the path which includes movement along the Sheephead Fault. This option requires only 15° of rotation.

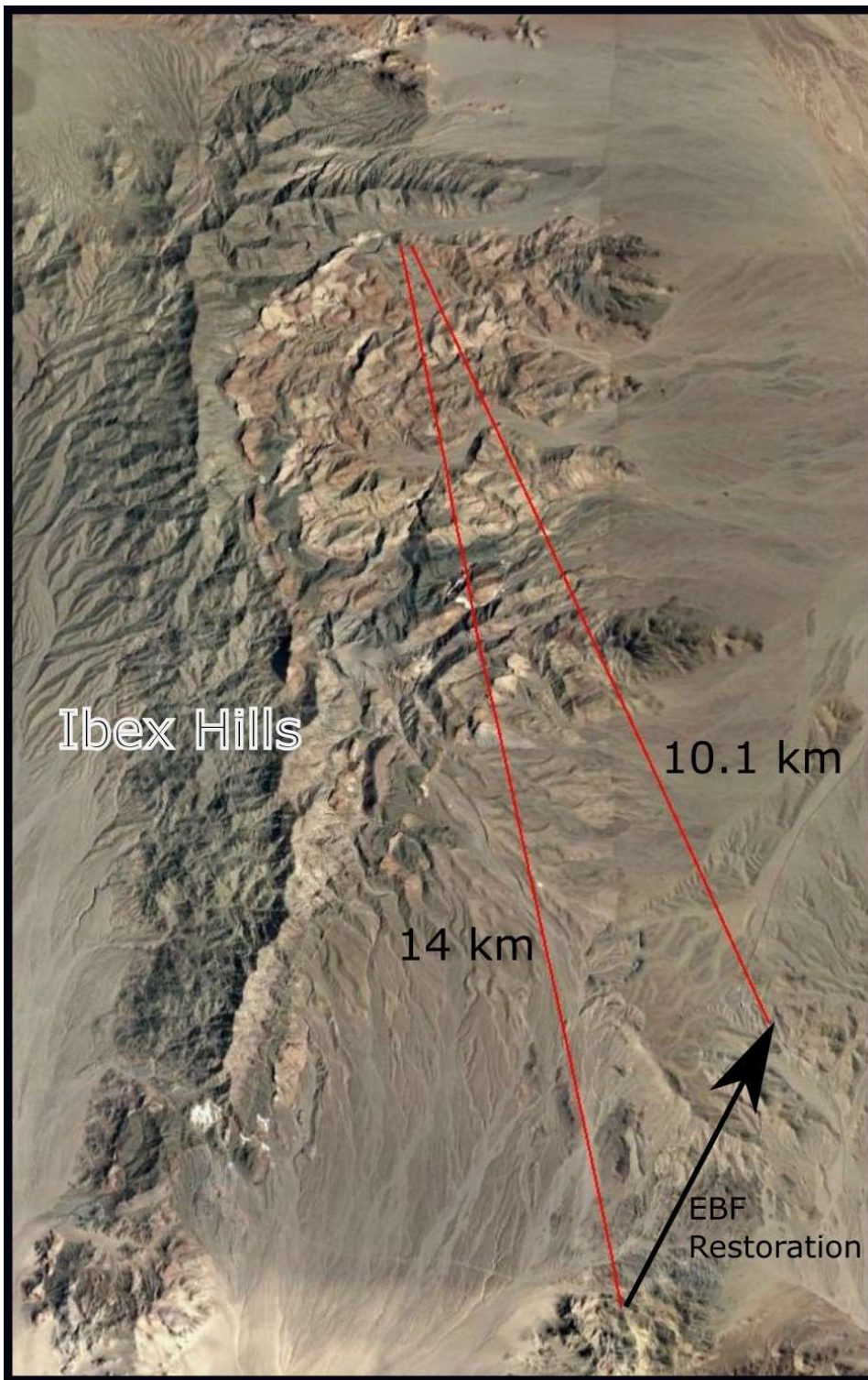


Figure 3.11. Satellite image of the Ibex Hills and northern Saddle Peak Hills area (Google Earth) overlain with the horizontal distances between the intrusives of Canalda (2009) in the south and the intrusive mapped in the northern Ibex Hills. The arrow indicate the relative position of the Ibex Pass intrusive after movement along the EBF is restored.

Figure 3.12. See associate 3D pdf. 3D model showing the restored faults, C and D in their projected positions in the Saddle Peak Hills. A cross-section of the Saddle Peak Hills shows the presence of low-angle faults which cut the Johnnie Fm., perhaps related to those in the Ibex Hills.

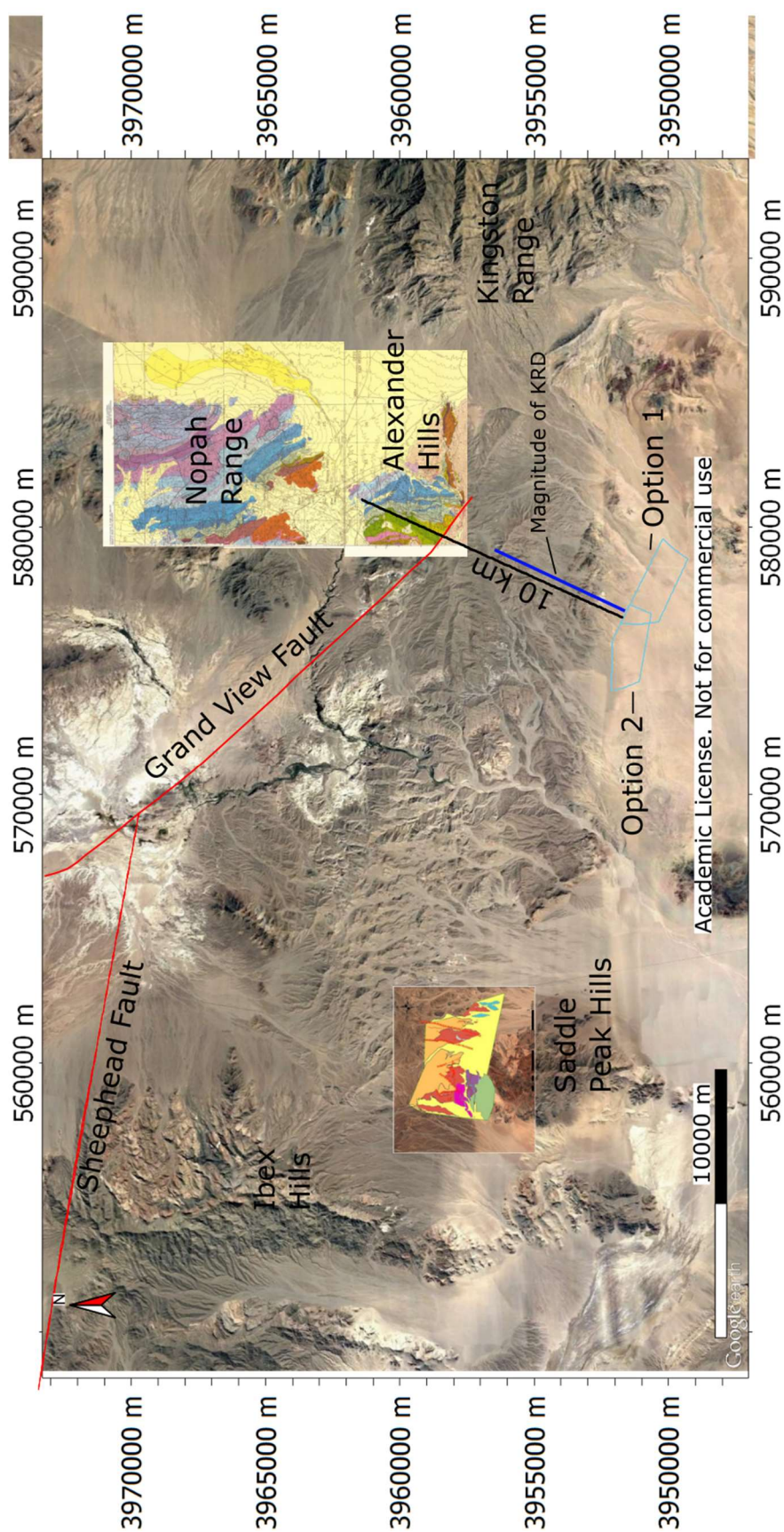


Figure 3.13. Map showing the distances between the stratigraphic pinch out of the Beck Spring below the Noonday Fm in the Ibx Hills and the same contact in the northern Alexander Hills. The blue line indicates the magnitude of motion on the Kingston Range Detachment. Light blue boxes represent the extent of the Beck Spring Dolomite in the Ibx Hills after restoration of the two model options.

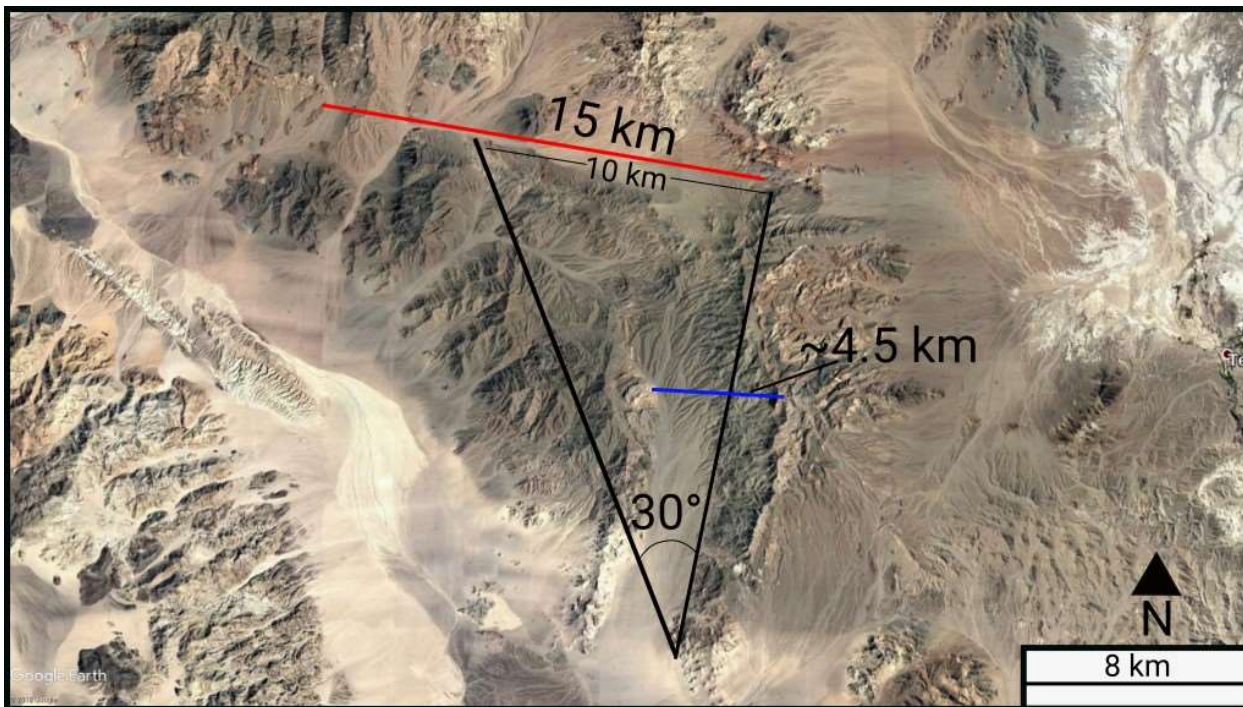


Figure 3.14. Map showing the distance between the Ibex Hills and the Amargos Chaos (red line). The black lines represent the distance along the Sheephead Fault that the Ibex Hills might have traveled given a 30° clockwise rotation with an axis at the southern extent of the range. The blue line shows the current horizontal distance between the Beck Spring Dolomite of the Confidence Wash area and the same unit in the central Ibex Hills.

References

- Bidgoli, T.S., Amir, E., Walker, J.D., Stockli, D.F., Andrew, J.E., and Caskey, S.J., 2015, Low-temperature thermochronology of the Black and Panamint mountains, Death Valley, California: Implications for geodynamic controls on Cenozoic intraplate strain: *Lithosphere*, p. L406.1, doi: 10.1130/L406.1.
- Buck, W.R., Martinez, F., Steckler, M.S., and Cochran, J.R., 1988, Thermal consequences of lithospheric extension; pure and simple: *Tectonics*, v. 7, p. 213–234, doi: <http://0-dx.doi.org.lib.utep.edu/10.1029/TC007i002p00213>.
- Burchfiel, B.C., and Stewart, J.H., 1966, “Pull-Apart” Origin of the Central Segment of Death Valley, California: *Geological Society of America Bulletin*, v. 77, p. 439–442, doi: 10.1130/0016-7606(1966)77[439:POOTCS]2.0.CO;2.
- Calzia, J.P., and Ramo, O.T., 2000, Late Cenozoic crustal extension and magmatism, southern Death Valley region, California (D. R. Lageson, Ed.): *GSA Field Guide*, v. 2, p. 135–164.
- Canalda, S.M., 2009, Magnitude of right-lateral offset on the southern Death Valley fault zone from Miocene volcanic assemblages [M.S.]: The University of Texas at El Paso, 155 p., <http://0-search.proquest.com.lib.utep.edu/pqdtglobal/docview/305068006/abstract/FFFE661790334E34PQ/2?accountid=7121> (accessed February 2015).
- Davis, G.A., Fowler, T.K., Bishop, K.M., Brudos, T.C., Friedmann, S.J., Burbank, D.W., Parke, M.A., and Burchfiel, B.C., 1993, Pluton pinning of an active Miocene detachment fault system, eastern Mojave Desert, California: *Geology*, v. 21, p. 627–630, doi: 10.1130/0091-7613(1993)021<0627:PPOAAM>2.3.CO;2.
- Fleming, Z.D., and Pavlis, T.L., 2018, Structural analysis of the ibex hills, Ca: evidence for multiple phases of Mesozoic shortening and transtensional related folding, faulting, and extension: *Abstracts with Programs - Geological Society of America*, v. 50, p. Abstract no. 18-3.
- Fowler, T.K., and Calzia, J.P., 1999, Kingston Range detachment fault, southeastern Death Valley region, California; relation to Tertiary deposits and reconstruction of initial dip (L. A. Wright, Ed.): *Special Paper - Geological Society of America*, v. 333, p. 245–257.

Fridrich, C.J., and Thompson, R.A., 2011, Cenozoic tectonic reorganizations of the Death Valley region, southeast California and southwest Nevada: U. S. Geological Survey Professional Paper, p. 36, 1 sheet.

Guest, B., Pavlis, T.L., Golding, H., and Serpa, L., 2003, Chasing the Garlock: A study of tectonic response to vertical axis rotation: *Geology*, v. 31, p. 553–556, doi: 10.1130/0091-7613(2003)031<0553:CTGASO>2.0.CO;2.

Hamilton, W.B., 1988, Detachment faulting in the Death Valley region, California and Nevada (M. D. Carr, Ed.): U. S. Geological Survey Bulletin, p. 51–85.

Hillhouse, J.W., 1987, Late Tertiary and Quaternary geology of the Tecopa Basin, southeastern California: U. S. Geological Survey Reston VA, 16, 1 sheet p., <http://0.search.proquest.com/georef/docview/51056591/F83044699F64643PQ/1> (accessed August 2018).

Holm, D.K., and Dokka, R.K., 1993, Interpretation and tectonic implications of cooling histories: An example from the Black Mountains, Death Valley extended terrane, California: *Earth and Planetary Science Letters*, v. 116, p. 63–80, doi: 10.1016/0012-821X(93)90045-B.

Holm, D.K., Pavlis, T.L., and Topping, D.J., 1994, Black Mountains crustal section, Death Valley region, California (S. F. McGill, Ed.): Geological Society of America, Cordilleran Section, Annual Meeting, Guidebook., v. 27, p. 31–54.

Holm, D.K., and Wernicke, B., 1990, Black Mountains crustal section, Death Valley extended terrain, California: *Geology*, v. 18, p. 520–523, doi: 10.1130/0091-7613(1990)018<0520:BMCSDV>2.3.CO;2.

Luckow, H.G., Pavlis, T.L., Serpa, L.F., Guest, B., Wagner, D.L., Snee, L., Hensley, T.M., and Korjenkov, A., 2005, Late Cenozoic sedimentation and volcanism during transtensional deformation in Wingate Wash and the Owlshead Mountains, Death Valley: *Earth-Science Reviews*, v. 73, p. 43, doi: 10.1016/j.earscirev.2005.07.013.

Mahon, R.C., Dehler, C.M., Link, P.K., Karlstrom, K.E., and Gehrels, G.E., 2014, Geochronologic and stratigraphic constraints on the Mesoproterozoic and Neoproterozoic Pahrump

Group, Death Valley, California: A record of the assembly, stability, and breakup of Rodinia: Geological Society of America Bulletin, p. B30956.1, doi: 10.1130/B30956.1.

Mahon, R.C., and Link, P.K., 2013, EdMap geologic map of the Saddle Peak Hills 7.5' quadrangle, Death Valley National Park, San Bernardino County, California: Abstracts with Programs - Geological Society of America, v. 45, p. 372.

Mancktelow, N.S., and Pavlis, T.L., 1994, Fold-fault relationships in low-angle detachment systems: Tectonics, v. 13, p. 668–685, doi: 10.1029/93TC03489.

McMackin, M.R., 1992, Tectonic evolution of the Kingston Range, Death Valley, California [Doctoral]: Pennsylvania State University at University Park, University Park, PA, United States (USA), 183 p., <http://0-search.proquest.com.lib.utep.edu/georef/docview/50366954/citation/42CA980148AE48F3PQ/10> (accessed March 2016).

Miller, M.B., and Pavlis, T.L., 2005, The Black Mountains turtlebacks: Rosetta stones of Death Valley tectonics: Earth-Science Reviews, v. 73, p. 115–138, doi: 10.1016/j.earscirev.2005.04.007.

Miller, M.G., and Prave, A.R., 2002, Rolling hinge or fixed basin?: A test of continental extensional models in Death Valley, California, United States: Geology, v. 30, p. 847–850, doi: 10.1130/0091-7613(2002)030<0847:RHOFA>2.0.CO;2.

Norton, I., 2011, Two-stage formation of Death Valley: Geosphere, v. 7, p. 171–182, doi: 10.1130/GES00588.1.

Pavlis, T.L., Rutkofske, J., Guerrero, F., and Serpa, L.F., 2014, Structural overprinting of Mesozoic thrust systems in eastern California and its importance to reconstruction of Neogene extension in the southern Basin and Range: Geosphere, v. 10, p. 732–756, doi: 10.1130/GES00993.1.

Pavlis, T.L., Guest, B., H., and Serpa, L., Wagner, D., Snee, L., Hensley, T., and Korjenkov, A., 2012, Geologic map of the Wingate Wash area, Owlshead Mountains, Death Valley: GSA map and Charts Series, doi: 10.1130/2012.DMCH011.

Prave, A.R., and McMackin, M.R., 1999, Depositional framework of mid- to late Miocene strata, Dumont Hills and southern margin Kingston Range; implications for the tectonostratigraphic evolution

of the southern Death Valley region (L. A. Wright, Ed.): Special Paper - Geological Society of America, v. 333, p. 259–275.

Renik, B., 2010, Distribution of Neogene extension and strike slip in the Death Valley region, California-Nevada, with implications for palinspastic reconstruction and models of normal faulting: Ph.D. Thesis, p. 12.

Renik, B., and Christie-Blick, N., 2013, A new hypothesis for the amount and distribution of dextral displacement along the Fish Lake Valley–northern Death Valley–Furnace Creek fault zone, California-Nevada: *Tectonics*, v. 32, p. 123–145, doi: 10.1029/2012TC003170.

Serpa, L., and Pavlis, T.L., 1996, Three-dimensional model of the late Cenozoic history of the Death Valley region, southeastern California: *Tectonics*, v. 15, p. 1113–1128, doi: 10.1029/96TC01633.

Serpa, L., Voogd, B.D., Wright, L., Willemin, J., Oliver, J., Hauser, E., and Troxel, B., 1988, Structure of the central Death Valley pull-apart basin and vicinity from COCORP profiles in the southern Great Basin: *Geological Society of America Bulletin*, v. 100, p. 1437–1450, doi: 10.1130/0016-7606(1988)100<1437:SOTCDV>2.3.CO;2.

Snow, J.K., and Wernicke, B.P., 2000, Cenozoic tectonism in the central Basin and Range; magnitude, rate, and distribution of upper crustal strain: *American Journal of Science*, v. 300, p. 659–719, doi: 10.2475/ajs.300.9.659.

Spencer, J.E., 1984, Role of tectonic denudation in warping and uplift of low-angle normal faults: *Geology (Boulder)*, v. 12, p. 95–98.

Stewart, J.H., 1983, Extensional tectonics in the Death Valley area, California: Transport of the Panamint Range structural block 80 km northwestward: *Geology*, v. 11, p. 153–157, doi: 10.1130/0091-7613(1983)11<153:ETITDV>2.0.CO;2.

Topping, D.J., 2018, Mio-pliocene stratigraphic and structural evidence refutes simple rolling-hinge model for post-7.8 ma extension in the southern Black Mountains and indicates large-scale extension distributed among many faults: *Abstracts with Programs - Geological Society of America*, v. 50, p. Abstract no. 2-4.

Topping, D.J., 1993, Paleogeographic reconstruction of the Death Valley extended region: Evidence from Miocene large rock-avalanche deposits in the Amargosa Chaos Basin, California: Geological Society of America Bulletin, v. 105, p. 1190–1213, doi: 10.1130/0016-7606(1993)105<1190:PROTDV>2.3.CO;2.

Wernicke, B.P., and Axen, G.J., 1988, On the role of isostasy in the evolution of normal fault systems: Geology (Boulder), v. 16, p. 848–851, doi: [http://0-dx.doi.org.lib.utep.edu/10.1130/0091-7613\(1988\)016](http://0-dx.doi.org.lib.utep.edu/10.1130/0091-7613(1988)016).

Wernicke, B., Axen, G.J., and Snow, J.K., 1988, Basin and Range extensional tectonics at the latitude of Las Vegas, Nevada: Geological Society of America Bulletin, v. 100, p. 1738–1757, doi: 10.1130/0016-7606(1988)100<1738:BARETA>2.3.CO;2.

Wright, L., 1974, Geology of the southeast quarter of the Tecopa quadrangle, San Bernardino and Inyo Counties, California:

Wright, L.A., Thompson, R.A., Troxel, B.W., Pavlis, T.L., DeWitt, E., Otton, J.K., Ellis, M.A., Miller, M.G., and Serpa, L.F., 1991, Cenozoic magmatic and tectonic evolution of the east-central Death Valley region, California (M. J. Walawender, Ed.): San Diego State Univ.; San Diego; CA, <http://0-search.proquest.com.lib.utep.edu/georef/docview/50430819/C8FB1E7B54A14F0DPQ/1> (accessed November 2015).

Wright, L., and Troxel, B., 1984, Geology of the northern half of the confidence hills 15-minute quadrangle, death valley region, eastern california; the area of the amargosa chaos: California Division of Mines and Geology.

Wright, L.A., and Troxel, B.W., 1973, Shallow-Fault Interpretation of Basin and Range Structure, Southwestern Great Basin: John Wiley & Sons, New York, <http://0-search.proquest.com.lib.utep.edu/georef/docview/52433136/2630E80EC9F84A79PQ/4> (accessed January 2017).

Wright, L.A., Troxel, B.W., Williams, E.G., Roberts, M.T., and Diehl, P.E., 1974, Precambrian sedimentary environments of the Death Valley region, eastern California: Death Valley Publ. Co.; Shoshone; CA, <http://0->

[search.proquest.com.lib.utep.edu/georef/docview/52351472/2DAD0567B15240FFPQ/2?accountid=712](http://search.proquest.com/lib.utep.edu/georef/docview/52351472/2DAD0567B15240FFPQ/2?accountid=712)
1 (accessed February 2015).

Vita

Zachariah Fleming received his Bachelor of Science degree in Geology from The College of William and Mary in 2014. Following that he joined UTEP's doctoral program in Geological Sciences in the fall of 2014.

During his tenure at UTEP Dr. Fleming was the recipient of a Geological Society of America (GSA) Student Research Grant as well as the Lauren Wright and Bennie Troxel Award for his work in the Death Valley, CA region.

Dr. Fleming presented his research at a number of regional and national conferences including GSA national meetings and GSA Cordilleran Sectional meetings. Along with the conference proceedings his work has also been published in the Journal of Structural Geology.

While pursuing his degree, Dr. Fleming was a Teaching Assistant for the Department of Geological Sciences. He is now employed as a Post-Doctoral Researcher at UniLaSalle.

Dr. Fleming's dissertation, Geometry, Timing, and Kinematics of Neogene Extensional and Transtensional Structures of Southern Death Valley: Implications for Regional Reconstructions and a Corrective Method for Rigid Body Rotations, was supervised by Dr. Terry Pavlis.

Permanent address: 19 rue Pierre Wagué
Beauvais, France 60000

This thesis/dissertation was typed by Zachariah Douglas Fleming.